Quantitative Methods for the Characterization of Separated and Intermittent Multiphase Flow Patterns

vorgelegt von
M. Sc.
Marc Olbrich

an der Fakultät V - Verkehrs- und Maschinensysteme
der Technischen Universität Berlin
zur Erlangung des akademischen Grades

Doktor der Ingenieurwissenschaften
-Dr.-Ing.-

genehmigte Dissertation

Promotionsausschuss:
Vorsitzender: Prof. Dr.-Ing. Christian Oliver Paschereit
Gutachter: Prof. Dr.-Ing. Kilian Oberleithner
Gutachter: Prof. Dr. Abdulla Ghani
Gutachter: Prof. Dr. Jiri Polansky
Gutachterin: Dr. rer. nat. Sonja Schmelter
Tag der wissenschaftlichen Aussprache: 17. Oktober 2022

Berlin 2022

For Leili, Minu & Dora.
♡

Acknowledgements

First and foremost I would like to express my sincere gratitude to my supervisors Dr. Sonja Schmelter, Prof. Dr.-Ing Kilian Oberleithner und Prof. Dr. Markus Bär for their assistance, insightful comments and suggestions during my PhD study, my publications and my doctoral thesis. I would also like to thank Dr. Moritz Sieber, Dr. Nando Farchmin, Dr. Vasco Worlitzer and all the members of the working group 8.41 from the Physikalisch-Technische Bundesanstalt for their kind support and inspiring discussions. I would also like to thank my parents Simone and Günter, who have supported me throughout the years. Finally, I am deeply grateful to my wonderful wife Leili and our wonderful children Minu and Dora for their love, support, encouragement and belief in me.

This work was supported through the Joint Research Project Multiphase flow reference metrology (16ENG07). This project has received funding from the EMPIR programme co-financed by the Participating States and from the European Union's Horizon 2020 research and innovation programme.

Zusammenfassung

Eine Mehrphasenströmung bezeichnet eine simultane Strömung von verschiedenen Phasen, wie zum Beispiel: Flüssigkeiten, Gasen und Festkörpern. Sie ist Bestandteil verschiedenster Prozesse in der Industrie und Umwelt. Mehrphasenströmungen stellen aufgrund ihrer Komplexität hohe Anforderungen an den Entwurf und Betrieb von industriellen Anlagen und Rohrsystemen, weshalb sie einen Schwerpunkt in Wissenschaft und Forschung bilden. Dies gilt in besonderem Maße für zweiphasige Rohrströmungen von Gasen und Flüssigkeiten, bei denen sich verschiedene Strömungsmuster (*flow patterns*) ausgeprägen können. Diese Strömungsmuster stellen Kategorien dar, welche die zeitliche und räumliche Verteilung der verschiedenen Phasen innerhalb der Strömung beschreiben. Sie entstehen in der Regel in Abhängigkeit von den Fluideigenschaften, der Rohrgeometrie und den Strömungsbedingungen. Bei zweiphasigen Strömungen in horizontalen Rohren wird typischerweise zwischen den folgenden sieben Strömungsmustern unterschieden: *Schichtströmung (stratified flow)*, *Wellenströmung (wavy flow)*, *Pfropenströmung (plug flow)*, *Schwallströmung (slug flow)*, *Tröpfen-Ringströmung (annular flow)*, *Sprühströmung (mist flow)* und *Blasenströmung (bubbly flow)*. Aufgrund ihrer intermittierenden Abfolge von großen Gasblasen und rohrquerschnittsfüllenden Flüssigkeitsansammlungen führen vor allem Schwall- und Pfropfenströmungen zu diversen Nachteilen, wie zum Beispiel: hohen Fehlern bei Durchflussmessungen, großen Druckverlusten, unerwünschten Schwankungen bei Druck und Volumenstrom sowie induzierten Vibrationen und einer damit verbundenen erhöhten Materialermüdung der durchströmten Rohre. Dies gilt insbesondere für den Stofftransport in der Öl- und Gasindustrie mit ihren weitreichenden Pipeline-Systemen. Aus diesen Gründen werden die Strömungsmuster schon bei der Planung solcher Anlagen mit einbezogen. Dafür werden unter anderem verschiedene Vorhersage-Modelle, numerische Strömungssimulationen oder empirische Korrelationen verwendet. Aufgrund der Komplexität der Strömungsmuster und der vielen verschiedenen Einflüsse bei ihrer Entstehung sind Verfahren, welche die Strömungsmuster und ihre zeitlichen und räumlichen Charakterisierungen für gegebene Fluideigenschaften, Strömungsbedingungen und Rohrdurchmesser zuverlässig und präzise vorhersagen, Gegenstand aktueller Forschung. Für die Entwicklung und Validierung solcher Modelle, Simulationen und Korrelation sind akkurate Quantifizierungen der betrachteten Strömungen erforderlich. Dies gilt nicht nur für die intermittierenden Strömungsmuster, wie Schwallströmung, sondern auch für die separierten Strömungsmuster, wie Schicht- und Wellenströmung, da diese oft den Ausgangszustand in der Entwicklung komplexerer Strömungsmuster darstellen. In diesem Zusammenhang werden quantitative Verfahren und neuartige Ansätze zur zeitlichen und räumlichen Charakterisierung von intermittierenden und separierten Zweiphasenströmungen in dieser Arbeit vorgestellt und diskutiert. Für diese Untersuchungen wurden zeitlich und räumlich aufgelöste Video- und Phasenvolumenanteilsdaten verwendet. Der Fokus lag dabei

auf den Schwallströmungen, da dieses komplexe Strömungsmuster eine große Ähnlichkeit zur vergleichsweise geordneteren Pfropfenströmung aufweist und auch Elemente der Schicht- und Wellenströmung beinhaltet.

Zu Beginn wird ein neuartiger Ansatz zur Quantifizierung von horizontalen Schwallströmungen mit dem Verfahren *Snapshot Proper Orthogonal Decomposition* (Snapshot-POD) vorgestellt. Dies beinhaltet Untersuchungen zur Repräsentation der Schwallstrukturen in den POD-Moden, die Ableitung räumlicher und zeitlicher Charakterisierungen von Schwallströmungen aus den POD-Moden, sowie die Anforderungen an die Ausgangsdaten für diese Anwendung. Für die verwendeten Datensätze wurde gezeigt, dass die Schwallstrukturen im dominanten Modenpaar einer Snapshot-POD-Analyse repräsentiert sind. Dabei bildet die räumliche Mode eine mittlere Schwallstruktur und der zugehörige zeitliche Koeffizient die zeitliche Veränderung der Phasengrenze ab. Im Weiteren wurde für diese Analysen gezeigt, dass sich die konventionellen Zeit- und Längenskalen zur Charakterisierung von horizontalen Schwallströmungen von den räumlichen und zeitlichen Informationen des dominanten Modenpaares ableiten lassen. Somit ermöglicht die Snapshot POD eine detaillierte zeitliche und räumlich Charakterisierung der Schwallströmungen. Darüber hinaus konnte ein Zusammenhang zwischen der Genauigkeit der abgeleiteten Charakterisierung und der Länge des betrachteten Rohrsegments festgestellt werden.

Für diese Untersuchungen wurden Approximationen der Zeitserie der Flüssigkeitshöhe an festen Positionen im Rohr (*Liquid level* - Zeitserie), sowie Zeitskalen der Schwallstrukturen aus Videoaufzeichnungen von Schwallströmungen abgeleitet. Diese videobasierten zeitlichen Quantifizierungen horizontaler Schwallströmungen werden im zweiten Teil dieser Arbeit mithilfe von konventionellen Tomographie-Messungen validiert. Dabei wurde eine systematische Überschätzung bei der Approximation der *Liquid level* - Zeitserie aus den Videodaten im Vergleich zur Tomographie-Messung festgestellt. Die aus der videobasierten *Liquid level*-Approximation abgeleiteten Zeitskalen ermöglichen hingegen eine zuverlässige Charakterisierung der Schwallstrukturen.

In diesem Zusammenhang kann sich ein Verfahren, welches schnell und zuverlässig die *Liquid level* - Zeitserie aus Videodaten approximiert, zur Analyse von Schwallströmungen, aber auch anderen separierten und intermittierenden Zweiphasenströmungen, in wissenschaftlichen und industriellen Anwendungen eignen. Aus diesem Grund wird im letzten Teil dieser Arbeit ein neues *Deep Learning* - basiertes Bildverarbeitungsverfahren zur Approximation der *Liquid level* - Zeitserie aus Videoaufzeichnungen von separierten und intermittierenden Zweiphasenströmungen vorgestellt und diskutiert. Dabei konnte gezeigt werden, dass das Verfahren die *Liquid level* - Zeitserie akkurat und konsistent aus den Videodaten extrahiert. Dabei liefert es auch bei heterogenen, untrainierten und verrauschten Videodatensätzen zuverlässige Ergebnisse. Nach dem erfolgreichen Training des Deep-Learning-Modells benötigt eine Segmentierung der verwendeten Videodaten nur sehr wenig Rechenzeit, sodass das vorgestellte Verfahren eine schnelle und exakte Approximation der *Liquid level* - Zeitserie ermöglicht.

Abstract

Multiphase flow is defined as the simultaneous flow of different phases, such as liquids, gases or solids, and occurs in a variety of industrial and environmental processes. This type of flow poses special challenges for the operators and engineers due to the complex behavior of the phases, which is still subject to intensive research efforts. This applies in particular to gas-liquid pipe flows with its different flow patterns, i.e., categories of spatio-temporal phase distributions. The formation of these flow patterns depend on the fluid properties, the geometry of the pipes and the operating conditions. Several flow patterns with different properties have been identified in horizontal pipes, namely stratified flow, wavy flow, plug flow, slug flow, annular flow, bubbly flow, and mist flow. Due to their intermittent sequence of liquid blocks and large gas bubbles, the slug and plug flow pattern cause various disadvantages for the operating facilities, including higher measurement errors, larger pressure drops, undesired fluctuations in pressure and flow rates, as well as induced vibrations and the associated fatigue of the piping. These flows are encountered especially in the deep sea oil and gas production with its long transportation pipelines. Because of this, it is important to take these intermittent flow patterns into account for the design of multiphase transportation pipeline systems. Therefore, predictive models, numerical simulations, and empirical correlations have widely been used as a starting point for engineering designs. However, due to the complexity of these flow patterns, it is still subject to intensive research to find models, which reliably and accurately predict the flow patterns and their temporal and spatial characteristics for given flow rates, fluid properties, pipe diameters, and inclinations. For the development, calibration and validation of such predictive models, correlations and simulations, methods that provide precise descriptions of these flows are of special interest. This includes the complex intermittent flow patterns, such as slug flow, but also the separated flow patterns, such as stratified or wavy flow, since they often constitute an initial state in the development of the other, more complex flow patterns.

In this thesis, quantitative methods and novel approaches are presented and discussed, which enable a precise temporal and spatial characterization of separated and intermittent flow patterns from spatio-temporal flow data, such as raw video data or snapshot sequences of phase fraction fields. The focus for these investigations is on the slug flow pattern, since it is similar but more complex compared to the plug flow pattern and also contains stratified and wavy elements.

At first, a novel approach for the quantification of horizontal slug flow with *snapshot Proper Orthogonal Decomposition* (snapshot POD) is investigated in this thesis. This includes the aspect of the representation of the slugs in the POD -modes, the derivation of the spatial and temporal characteristics of slug flow from the POD -modes and the data requirements for this application. It was found that the slugs are represented in the dominant mode pair

of snapshot POD analysis for the considered data sets. This includes a description of the gas-liquid interface dynamics in the temporal coefficients as well as the representation of the averaged slug in the spatial modes. It is shown that the conventional length and time scale for a characterization of the considered slug flows can be derived from the temporal and spatial information of the dominant mode pair. Hence, the snapshot POD allows a detailed temporal and spatial characterization of the slugs. Moreover, it was found that, the length of the observed pipe segment (region of interest) affects the accuracy of the derived temporal and spatial characterization.

In the course of these investigations, an approximation of the liquid level time series as well as time scales of slug flow have been derived from video recordings. In a second step, this video-based temporal quantification of horizontal slug flow is assessed in a further examination, where parameters from an established tomography measurement technique are used as a reference. It was found that the approximation of liquid level time series from the video data shows a systematic overestimation compared to the tomography measurements. In contrast to this, the derived temporal characteristics of the liquid slugs from this approximation provide a reasonable and consistent temporal characterization of slug flow.

In this context, a fast and reliable method for the approximation of the liquid level time series from video data can serve as a useful tool in industrial and academic operations, where a temporal quantification of separated and intermittent flow patterns, such as wavy or slug flow, is needed. In a third step, the accurate and efficient extraction of the liquid level time series from video observations of separated and intermittent flow patterns with a novel deep learning based image processing technique is investigated. It is shown that the presented method accurately extracts the liquid level time series from the considered video data. It can handle different types of data, even unseen data sets. Furthermore, it can overcome various noise effects, which are generally included in such image or video data. Once, the net is successfully trained, it predicts highly accurate segmentation maps in very short time. Hence, the liquid level time series can be extracted accurately and efficiently from the raw video data.

Table of Contents

List of Figures

1 Introduction

1.1 Multiphase flow

Multiphase flow is a simultaneous flow of several different phases, such as liquids, gases or solids [1]. In this context, a *phase* refers to the definition of the thermodynamic state of matter, i.e., a thermodynamic system or a region within the system, throughout which all of the (specific) properties, such as density, are uniform [1, 2, 3, 4]. Thus, liquids of different densities, such as oil and water, are often considered as separate phases [5].

Multiphase flows occur in a variety of industrial and environmental processes [6]. Examples of this are transportation pipelines in oil and gas production [7, 8], cooling of nuclear reactors [9], sediment transport in waterways [10], boiling and combustion [11, 12] as well as multiphase reactors in chemical industry and biotechnology [13].

A general categorization of multiphase flow is according to the different states of phases or components of the flow, e.g., *solid*, *liquid* and *gas* [14]. A common example of this is two-phase gas-liquid flow in a pipe. Further distinctions of multiphase flows are made according to the direction of the flow; *horizontal*, *inclined* and *vertical*. This becomes important for larger differences in the densities of the phases, due to the influence of gravity. In addition to that, also the flow directions of the phases with respect to each other are considered. The flow is called *counter-current* when the phases flow in opposite directions and it is called *co-current or parallel* when they flow in the same direction [1].

There is a need for a phenomenological understanding of the complex behavior of multiphase flows for engineering designs since they appear in various industrial processes [6]. This has already been the subject of intensive research efforts [15]. However, the central issue in developing scientific approaches to gas-liquid pipe flows is the understanding of the spatio-temporal distribution of the different phases, also called *flow patterns* or *flow regimes* [6]. Based on the fluid properties, the geometry of the pipes and the operating conditions, different flow patterns can form [16]. These flow patterns are used to classify gas-liquid flows.

The present work is mainly concerned with multiphase flows of one category, namely co-current gas-liquid two phase flows in horizontal pipes, which especially occur in transportation

pipelines of the oil and gas industry. The flow patterns that can form for this category of multiphase flows are introduced in Section 1.2.

1.2 Gas-liquid flow patterns

In this section, the different flow patterns for co-current gas-liquid flows in horizontal pipes are introduced. Typically, they are classified into seven different flow patterns, namely *bubbly flow*, *plug flow*, *stratified flow*, *wavy flow*, *slug flow*, *annular flow*, and *mist flow*, which were identified mostly by observations of air-water and air-oil flows, see [17, 18, 19, 6, 16]. They are illustrated in Figure 1.1 and briefly described in the following.

- **Bubbly flow** consists of a continuous liquid phase with dispersed gas bubbles, which are moving in the upper part of the pipe at approximately the same velocity as the liquid [17].
- **Plug flow** consists of a continuous liquid phase with elongated gas bubbles, which move in the upper part of the pipe and alternate with plugs of liquid [17]. Due to the shape of the gas bubbles, this flow pattern is also known as *elongated bubble flow* [20].
- **Stratified flow** consists of continuous phases of liquid and gas, whereas the liquid flows along the bottom of the pipe and the gas flows above, over a smooth gas-liquid interface [17]. This flow pattern is also named, *stratified smooth flow* [21].
- **Wavy flow** is similar to a stratified flow, except that the interface is disturbed by waves, which are traveling in flow direction [17]. This flow pattern is also named, *stratified wavy flow* [21].
- **Slug flow** consists of a continuous liquid phase with coherent blocks of aerated liquid, which are separated by volumes of gas. These aerated blocks of liquid are called slugs and move along the pipe on top of a slowly flowing liquid layer at approximately the same velocity as the gas [6, 22, 23].
- **Annular flow** consists of a liquid film, that forms around the inside wall of the pipe with gas flowing at the central core, where some of the liquid is entrained as droplets [6, 17].
- **Mist flow** consists of liquid that is entrained as spray by the gas [17].

In Figure 1.1, the sequence of flow patterns are given for a fixed liquid flow rate and an increasing gas flow rate, according to [17, 18, 19]. For this, a horizontal pipe flow with a fixed liquid flow rate is considered, such that the observed pipe segment is completely filled with liquid. Then the gas flow is added in increasing amounts to form the different flow patterns [17]. At low gas flow rates, the gas is dispersed in bubbles and the bubble pattern forms. With increasing gas flow rates, the bubbles become larger and coalesce to form long bubbles resulting in the plug flow regime. For further increase in gas flow rate, the elongated gas bubbles join to form a continuous gas layer in the upper part of the pipe, resulting in the stratified flow regime. Due to the lower viscosity and lower density of the gas, it will flow faster than the

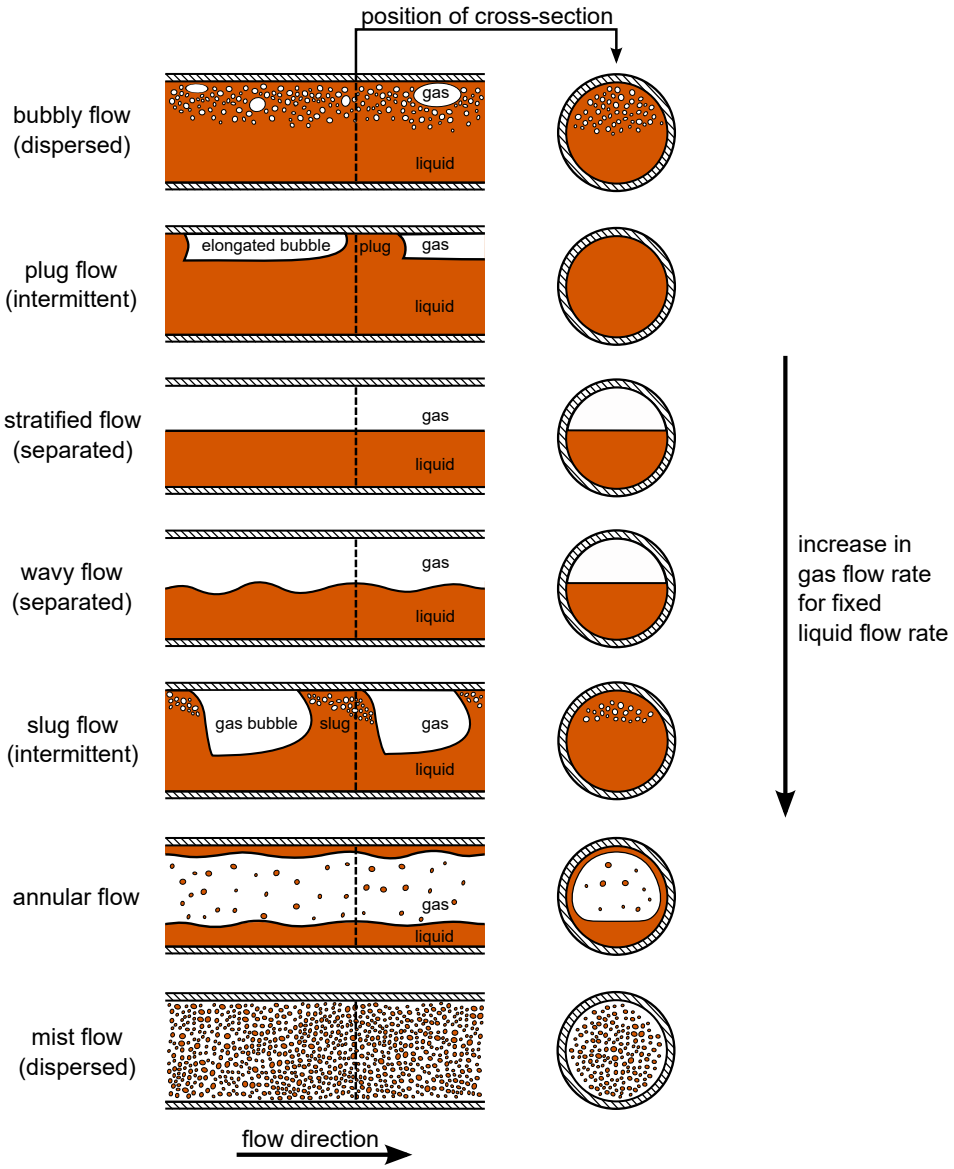

Figure 1.1: Illustration of horizontal gas liquid flow pattern in a longitudinal section of a pipe segment (left) and in a cross-section of the pipe (right).

liquid. As the gas flow rate is increased further, the interfacial shear stress becomes sufficient to generate waves on the surface of the liquid, producing the wavy flow regime. As the gas flow rate continues to rise, the waves, which travel in the direction of the flow, grow until their crests approach the top of the pipe, and block the gas flow to form a slug, which is then accelerated by the faster gas flow. This is known as slug flow pattern. At higher gas flow rates, the gas flow breaks through the waves and slugs, and the liquid is distributed over the inner wall of the pipe to form the annular regime. At very high gas flow rates, the liquid is being dispersed as droplets by the gas flow, resulting in the mist flow pattern. This description of the flow pattern sequence was taken from [19]. Further details on the different flow patterns and their transition can be found in [1, 6].

Since stratified and wavy flow consists of two continuous phases, separated by a (continuous) gas-liquid interface, these two flow patterns are grouped into *separated flows*. Due to their dispersed liquid or gaseous phases, bubbly and mist flow are grouped into *dispersed flows* [14]. For plug and slug flow, the liquid structures (plugs and slugs) appear intermittently. Because

of this, they are grouped into *intermittent flows* [6]. Due to their similar appearance, slug and plug flow are often not differentiated, see for example [21]. However, a differentiation between plug and slug flow was given in [24] and [6] by considering whether the liquid blockage contains gas bubbles or how fast the liquid blockage propagates relative to the liquid layer below, see [25, 26, 6].

In this work, only separated and intermittent flow patterns are considered, since the phase distribution with the gas-liquid interface needs to be visible from the side for the proposed methods and analyses. Due to its complexity and industrial relevance, the focus is on the slug flow pattern, which is described in further detail in Section 1.2.1.

1.2.1 Slug flow pattern

The slug flow pattern is one of the most common gas-liquid flow patterns in multiphase transportation pipelines, particularly in the oil and gas production [27]. As mentioned before in Section 1.2, it is characterized by a continuous liquid phase with coherent blocks of aerated liquid, which appear intermittently, and are separated by volumes of gas. These aerated liquid blocks moving on top of a slowly flowing liquid layer downstream the pipe at approximately the same velocity as the gas. They are called slugs [6, 22, 23]. Based on the slug initiation mechanism, the slug flow pattern in pipes can be classified into different categories, including *terrain-induced slugging*, *operationally induced slugging* as well as *hydrodynamic slugging*, see [16, 23].

Depending on the topography of the terrain, the geometry of the pipeline and local flow conditions, the liquid phase can accumulate in the low points of the pipeline, forming long blocks of liquid, which can be blown out from one pipeline section to the next by the gas pressure, see [28]. This phenomenon is called terrain-induced slugging. A severe form of this type of slugging occurs in pipeline systems with vertical riser segments, which are typically used in the subsea oil and gas production [29].

Operationally induced slugging is caused by transient operating conditions. These transient conditions include start-ups, operational upsets, such as changes in flow rates and pressure [28], and pigging procedures in pipelines [30]. Due to these transients, the liquid in the pipe can accumulate locally and form slugs [16].

Hydrodynamic slugging is caused by instabilities at the stratified gas-liquid interface. These instabilities evolve into waves, which can grow to fill the complete pipe cross-section with liquid, block the gas flow and form a slug [6].

The slug initiation mechanism of hydrodynamic slugging is still subject to research since the detailed behavior of the phases and the complex phenomena that occur in the development of slugs are not fully understood, see e.g., [23, 31]. However, in the following, a short description based on the dominant phenomena is given, which provides a basic understanding of this process.

Often the slug initiation mechanism of hydrodynamic slugging is described as a pattern transition along a horizontal pipe, starting with stratified flow close to the inlet for a given gas and liquid flow rate, for which slug flow can be observed downstream the pipe [23]. This is illustrated in Figure 1.2.

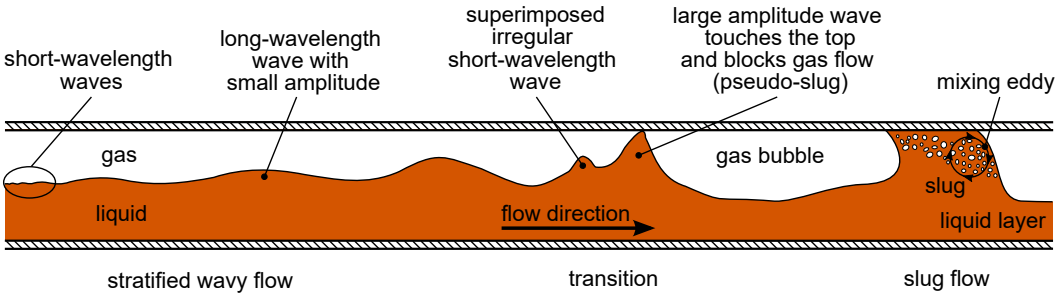

Figure 1.2: Illustration of slug initiation for hydrodynamic slugging in horizontal pipes, according to [6, 22, 32].

Initially, the two phases are separated by a smooth gas-liquid interface, where short-wavelength capillary waves can already be observed [33]. These short-wavelength waves grow to long-wavelength waves with small amplitudes further downstream the pipe [33], see Figure 1.2. Moreover, the liquid layer at the bottom of the pipe experiences larger shear forces from the pipe walls compared to the gas phase, due to the higher viscosity of the liquid. This causes the liquid layer to decelerate and the liquid level rises downstream [16, 21, 34, 33, 35]. Due to that, the cross-sectional area occupied by the gas decreases, and the gas flow accelerates [6, 23]. The pressure in the gas phase decreases, especially over the waves owing to the Bernoulli-effect resulting in a suction force acting on the interface and causes the wave to grow [21]. This effect is enhanced by the proximity of the upper wall [36] and additional irregular short-wavelength waves are superimposed on the long-wavelength waves. These can grow in amplitude and coalesce, as they propagate downstream and eventually touch the top of the pipe, fill the complete pipe cross-section with liquid, and block the gas flow [33, 6], see Figure 1.2. These liquid blockages are called *pseudo-slugs* or *slug precursors* [6, 16]. They can collapse or be accelerated by the faster gas flow and grow to form a slug [6, 33]. At the position, where such a (pseudo-)slug is formed and swept away, the pressure builds up behind the slug, the waves disappear and the liquid level drops [22]. The slug accelerates downstream the pipe to approximately the same velocity as the gas flow. When a slug moves along the pipe, it picks up the liquid from the slowly flowing liquid layer in front and sheds it in the liquid layer behind. For (pseudo-)slugs that grow in volume, the pick-up rate of liquid exceeds the shedding rate of liquid. They grow until a stable, *fully-developed state* is reached, where the pick-up rate of the slug is equal to its shedding rate [6]. Furthermore, gas is entrained into the slug as bubbles by a mixing eddy located at the front of the slug [35], see Figure 1.2. The entrained gas bubbles can rise to the top of the slug due to buoyancy, exit at the tail of the slug, or get shed along with the liquid in the liquid layer behind the slug [16].

Slug flow exists over a wide range of operational conditions for many different pipe diameters [35] and has several initiation mechanisms. Therefore, it is encountered particularly in the deep sea oil and gas production, where long transportation pipelines and risers from great depths are used, and the pressure in the oil and gas reservoirs, the ratio as well as the composition of the phases, such as gas, oil and brine water, and their flow rates vary over time [37].

The slug flow pattern can cause severe problems for industrial processes [38]. Field measurements of this type of flow are subject to larger measurement errors, see e.g., [39, 40, 41, 42]. The pressure drop due to the slug flow pattern can be an order of magnitude larger compared to other gas-liquid flow patterns, such as stratified or wavy flow [22]. The

sequence of liquid slugs causes undesired fluctuations in pressure and liquid or gas flow rates [43]. Furthermore, the slugs can grow to large structures, moving at high velocities. Thus, they can have large momenta and can induce vibrations and stresses when they impact on surfaces of the piping [6]. This can pose a serious threat to oil and gas production facilities. Because of this, it is important to take the slug flow pattern into account for the design of multiphase transportation pipeline systems. Therefore, predictive models, numerical simulations, and empirical correlations have widely been used as a starting point for engineering designs, see e.g., [6, 35, 44, 45, 46]. However, the slug flow pattern is inherently unsteady with large temporal variation of pressure, velocity and mass flow rate at any cross section, which leads also to unsteady processes of heat and mass transfer with substantial fluctuations in temperature and concentration [35]. This poses special and difficult problems for the modeling of the flow and it is still subject to intensive research to find models, which reliably and accurately predict the flow pattern and the slug characteristics for given flow rates, fluid properties, pipe diameters, and inclinations [35, 27, 47]. For the development, calibration and validation of such predictive models, correlations and simulations, methods that provide precise descriptions of slug flows are of special interest. Consequently, quantitative methods for such purpose are investigated in this thesis.

Slug flow is typically quantified by the length and time scales of the slugs as well as their translational velocities [48, 49]. This mainly includes the slug body length L_b and the slug unit length L_u, i.e. the distance between the slug front and slug rear or two consecutive slug fronts, respectively, their corresponding time scales, the slug unit times T_u and the slug body time T_b, i.e. the time a slug body or a slug unit needs to pass by at a fixed position, as well as the mean slug frequency, defined as

$$\bar{f}_s = \frac{1}{\bar{T}_u} \text{ with } \bar{T}_u = \frac{1}{N_s} \sum_{i=1}^{N_s} T_{u_i}, \tag{1.1}$$

where N_s denotes the number of slug units in the considered time interval, see [49, 23, 27, 50]. These length and time scales are illustrated in Figure 1.3.

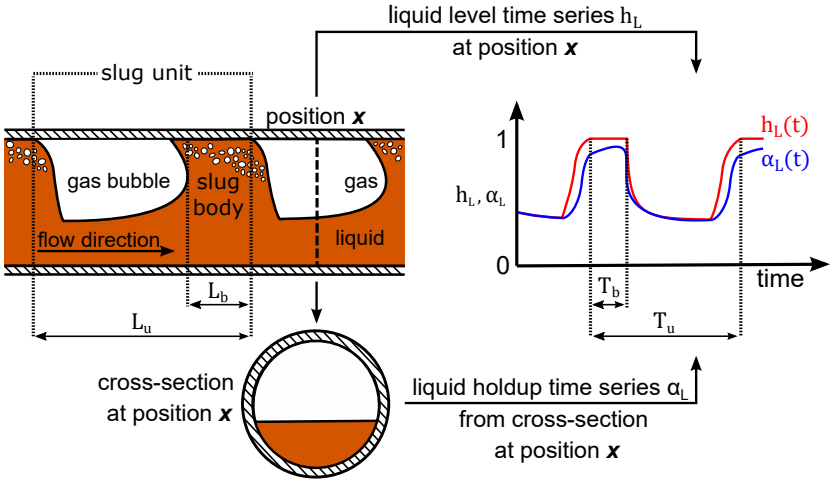

Figure 1.3: Illustration of length and time scales of slug flow with the liquid level time series from the vertical centerline of the pipe and the liquid holdup time series from the cross-section of the pipe at a streamwise position x.

The slug characteristics are often derived from time series that reveal the dynamics of the phase-distribution at a certain position in the pipe, such as liquid holdup and liquid level, see Figure 1.3.

The liquid holdup is a volumetric parameter and defined as the fraction of the volume of a considered pipe segment, which is occupied by the liquid phase at a time t [51]. It is denoted as $\alpha_L(t)$ and has a range of $[0, 1]$. Typically, for gas-liquid flows in horizontal pipes, the liquid holdup is measured in a pipe cross-section [6, 52], as illustrated in Figure 1.3. It can be measured either with intrusive techniques (instrumentation employed internal to the flow field), such as conductivity based wire-mesh sensors [53], or non-intrusive techniques (external to the flow field) [52], such as cross-sectional electrical capacitance tomography [40], cross-sectional X-ray tomography [54] or cross-sectional optical measurements [55].

The liquid level is a one-dimensional parameter and represents the local height of the liquid layer relative to the inner pipe diameter. It is defined as the vertical position of the gas-liquid interface relative to the inner pipe diameter in the vertical centerline of the pipe cross-section for a given streamwise position at a time t, as illustrated in Figure 1.3, see [36, 56, 57, 58]. It is denoted as $h_L(t)$ and has a range of $[0, 1]$. Typically, for gas-liquid flows in horizontal pipes, the liquid level is measured at the vertical centerline of the pipe, for instance with intrusive wire-sensors and needle-contact probes [36, 56, 57, 59] or non-intrusive narrow-beam gamma densiometers [60]. Other approaches are based on an approximations of the liquid level from cross-sectional liquid holdup measurements, see [61], and video data, as presented in an earlier work, see [62].

There are also other techniques for the measurement of slug characteristics in horizontal pipes, such as LED-triggering mechanisms for the local detection of slugs [63], video-analysis techniques for the measurement of length scales, geometrical properties and translational velocities of the slugs and bubbles [64, 65, 66], as well as simple visual observations of the slug frequency [67].

In this thesis, quantitative methods are presented and discussed, which enable not only an extraction of the slug characteristics, but also an approximation of the liquid level time series or its dynamic behavior from raw spatio-temporal flow data, such as videos or measured phase fractions. The basic concepts of these methods are introduced in the following section.

1.3 Methods

In this section, a brief introduction into the two main methodologies is given, which were used in this thesis. First, the *snapshot Proper Orthogonal Decomposition* is described. This quantitative method provides an energy-ranked mode basis of the coherent structures in the flow data and reveals their spatial and temporal features. Due to that capability, this method is employed to enable an extraction of the slug characteristics as well as an approximation of the liquid level dynamics from raw spatio-temporal slug flow data. Second, the concept of the *U-net*, a specific convolutional neural network architecture, is briefly introduced. This network constitutes the major component of an image-processing technique presented in this thesis that provides an approximation of the liquid level time series from raw spatio-temporal two- and three-phase flow data.

Detailed descriptions of the two methodologies can be found in the individual publications in Chapter 2.

1.3.1 Snapshot Proper Orthogonal Decomposition

The snapshot **P**roper **O**rthogonal **D**ecomposition (snapshot POD) is a modal decomposition, which extracts an energy-ranked mode basis of the coherent structures from the flow data [68, 69]. This orthonormal basis captures the dominant components from high dimensional data sets with only few modes [70]. The snapshot POD is based on the more general Proper Orthogonal Decomposition (POD) technique introduced by Lumley [71] in the context of turbulence and was proposed by Sirovich [72] as an efficient approach to determine the POD modes from high dimensional fluid flow data. For a snapshot POD of a flow field of interest g, spatially and temporally resolved data is required. In this context, let $(g(x,t_k))_{k=1,\dots,N}$ be a snapshot sequence of a scalar or vector field on a discrete domain with M spatial points and $N < M$. Then, the data is decomposed as follows

$$g(x,t_k) = \bar{g}(x,t_k) + g'(x,t_k) = \bar{g}(x,t_k) + \sum_{i=1}^{N} a_i(t_k)\phi_i(x), \tag{1.2}$$

for all times t_k and spatial points x, where $\bar{g}$ denotes the time-averaged data field, g' the corresponding fluctuations, a_i the i-th temporal coefficient and ϕ_i the i-th spatial mode. Consequently, the (temporal) fluctuations g' in the original field g are expressed as the linear combination of the spatial modes ϕ_i and their corresponding temporal coefficients a_i [69]. Furthermore, a_i and ϕ_i can be obtained from an eigenvalue decomposition of the (temporal) covariance matrix $R \in \mathbb{R}^{N\times N}$ resulting from g:

$$Rv_i = \lambda_i v_i \text{ for } i = 1,\dots,N \text{ with } \lambda_1 \geq \cdots \geq \lambda_N \geq 0. \tag{1.3}$$

Here, the temporal coefficient a_i is given by the scaled eigenvector v_i with respect to the eigenvalue λ_i as

$$a_i \coloneqq \sqrt{N\lambda_i}\, v_i \text{ for } i = 1,\dots,N, \tag{1.4}$$

and the spatial mode

$$\phi_i(x) \coloneqq \frac{1}{N\lambda_i} \sum_{k=1}^{N} a_i(t_k) g'(x,t_k) \text{ for } i = 1,\dots,N. \tag{1.5}$$

A detailed description of the calculations of R from g can be found in [69], as well as in the method section of the first two publications given in Chapter 2.

Note that the sum of all eigenvalues represents the mean energy of the considered system, according to [72]. For a variable of interest g with appropriate physical units, the mean energy of the considered system can be identified with a physical energy, such as turbulent kinetic energy for a velocity field [69, 72]. However, for variables with arbitrary units instead of physical units, the mean energy of the system refers to the total variance in the data set [73]. Thus an eigenvalue λ_i represents a measure for the proportion of the intensity of the mean

fluctuations from the data set that is captured by the corresponding eigenvector, or rather the corresponding temporal coefficient.

After the POD modes are calculated for a given flow field of interest, an additional mode coupling algorithm is applied for the analyses in this thesis. This algorithm was introduced by Sieber et al. in [68] and is based on the fact that the dynamics of periodic coherent structures can be described by a pair of modes and the observation that such modes also show a similar amount of energy and appear pairwise in the POD spectrum, i.e. eigenvalues appear pairwise in the spectrum of R (see Equation 1.3), as mentioned in [74]. The algorithm identifies related modes by the spectral similarity of their temporal coefficients, which accounts for modes that are shifted by a quarter period. Then the identified modes are combined into pairs of coupled modes, which are assumed to describe the same underlying coherent structure. This is achieved by an additional eigenvalue decomposition of the temporal coefficients and the calculation of the harmonic correlation as similarity measure of the different modes. Details can be found in [68], as well as in the method section of the first two publications given in Chapter 2.

Even though other variations of the POD technique exist, e.g., spatial POD, the snapshot-based approach is presently the most widely used POD method in fluid mechanics, due to the significant reduction in the required computation and memory resources [69]. The applications of the POD techniques include fundamental analysis of fluids flows [75], reduced-order modeling [76], data compression and reconstruction [77, 78], flow control [79, 80], and aerodynamic design optimization [81], particularly for single phase flows, see also [69]. For multiphase flows, however, there are only a few references on POD. The method was primarily used to find a low order description of large and complex multiphase flow data sets [82, 83, 84] and to investigate turbulent structures in two-phase flows [85, 86, 87, 88]. In [89] a temporal characterization of horizontal slug flow is presented, based on a POD-analysis of cross-sectional tomography measurements.

In this thesis, not only a temporal, but also a spatial characterization of horizontal slug flow as well as an approximation of the dynamic behavior of the liquid level time series, derived from a POD-analysis of raw spatially and temporally resolved data sets, is presented. These data sets consist of phase-fraction fields in a longitudinal section along the vertical centerline of the pipe as well as high speed video recordings from the side.

For a specific temporal characterization of separated and intermittent multiphase flows, a deep learning based image-processing technique is also presented in this thesis, which enables a fast and robust approximation of the liquid level time series from raw video data. In this context, the basic concepts of deep learning and the used network architecture, called *U-net*, is briefly introduced in the next section.

1.3.2 U-net

Deep learning is a subfield of machine learning and allows computational models, which are composed of multiple processing layers, to learn representations of data with multiple levels of abstraction [90, 91]. **C**onvolutional **N**eural **N**etworks (CNN) constitute a class of deep learning models which are based on convolution operations in the layers [92, 93]. CNN's are widely used for image classification and segmentation problems [94, 95]. The most common learning technique for CNN's is supervised learning [91], where the model receives a set of

labeled input-output pairs as training data and learns a function that maps from input to output to predict also unseen data points [96, 97].

The U-net is a convolutional neural network architecture for a fast and precise segmentation of images and was introduced by Ronneberger et al. [98]. It has been successfully applied in many image-to-image learning problems, e.g., computer tomography, see [99, 100, 101]. The U-net is typically trained in a supervised manner and able to achieve accurate results with only few labelled training data. Details can be found in [98], as well as in the method section of Publication IV, given in Chapter 2.

An essential point to achieve the desired characterizations and approximations with the used data-driven approaches and quantitative methods are the data itself, and more precisely, the spatial and temporal features of the flow, which are captured in it. In that regard, the used data sets are described briefly in the next section.

1.4 Data

In this thesis, different types of spatially and temporally resolved data sets of separated and intermittent multiphase flows have been analysed. This includes data from high-speed video recordings of horizontal two- and three-phase flows at different position along the pipe and phase fraction measurements from cross-sectional electrical capacitance tomography (ECT) systems. The video data show an approximately 0.5 m long transparent pipe segment from the side, where the multiphase flow and its instationary phase-distribution can be observered. Thus, the three-dimensional flow in this 0.5 m long pipe segment is represented in the frames of the video as a two-dimensional projection with spatial degrees of freedom in vertical and longitudinal directions (see Figure 1.4). In contrast to this, the cross-sectional tomography measurements show the instationary phase-distribution inside a complete pipe cross-section, but only at a certain streamwise position, with spatial degrees of freedom in vertical and transversal directions (see Figure 1.4).

These data sets were acquired in experiments performed by TÜV SÜD NEL and DNV as part of the projects *Multiphase flow metrology in oil and gas production* (MultiFlowMet I) [102] and *Multiphase flow reference metrology* (MultiFlowMet II) [7].

Moreover, spatially and temporally resolved phase volume fraction fields from a numerical simulation of a horizontal air-water slug flow were also considered. These phase volume fraction fields were extracted from longitudinal sections of different lengths along the vertical centerline of the pipe, with spatial degrees of freedom in vertical and longitudinal directions (see Figure 1.4).

In Figure 1.4, the described types of data are illustrated. Please note that they are given one after another along the horizontal pipe just for illustration.

To achieve the desired characterizations and approximations with the previously described data-driven approaches and quantitative methods, snapshot sequences of the video frames from experiments as well as snapshot sequences of phase volume fraction fields from numerical simulations have been analysed. The cross-sectional tomography measurements provided reference parameters for validations.

Detailed descriptions of the data can be found in the individual publications in Chapter 2.

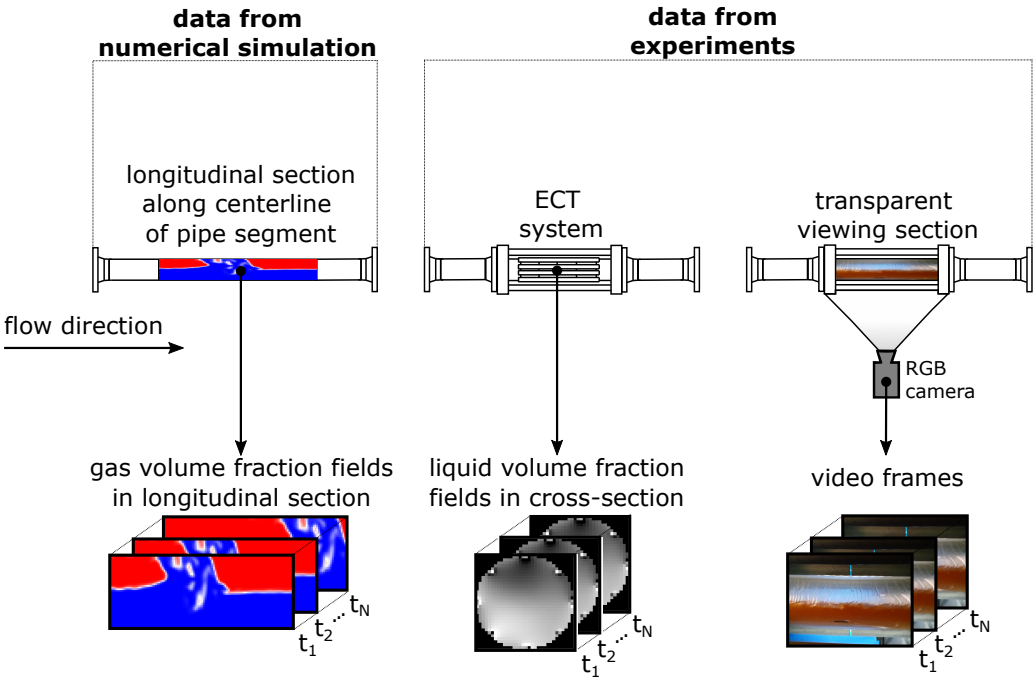

Figure 1.4: Illustration of the different types of spatially and temporally resolved data (snapshot sequences) that have been used in this thesis.

In the previous sections, the basic aspects for the understanding of the research presented in this thesis have been introduced. These topics include the phenomenology of gas-liquid flows and parameters for their quantification, the methodology of snapshot POD and the U-net as well as the different types of data. Accordingly, the research objectives are formulated in the following section.

1.5 Research objectives

Multiphase flows occur in a variety of industrial and environmental processes [6] and pose challenges for the operators and engineers due to the complex behavior of the phases and the lack of its complete phenomenological understanding. This applies in particular to gas-liquid slug flows, which are encountered especially in the deep sea oil and gas production. In this area, the slug flow pattern causes various disadvantages, e.g., increased measurement errors [42], increased pressure drops [22], undesired fluctuations in pressure and flow rates [43] as well as induce vibrations and the associated fatigue of the piping [6, 103]. Because of this, it is important to take the slug flow pattern into account for the design of multiphase transportation pipeline systems. Therefore, predictive models, numerical simulations, and empirical correlations have widely been used as a starting point for engineering designs [6, 35, 44, 45, 46]. However, due to the complexity of the slug flow pattern, it is still subject to intensive research to find models, which reliably and accurately predict the flow pattern and the slug characteristics for given flow rates, fluid properties, pipe diameters, and inclinations [35, 27, 47]. For the development, calibration and validation of such predictive models, correlations and simulations, methods that provide precise descriptions of slug flow are of special interest. Typically, the procedures that are used for this purpose, are focusing either on a temporal description of the slug flow or a spatial description of the slugs. This includes time series

analysis of phase volume fraction [40] and liquid level measurements [36] or image analysis for the measurement of geometrical properties of the slugs [64]. Some of the established approaches also rely on additional subjective decisions for the analysis, such as manually counting slugs [67]. Usually, the slug length is approximated from temporal descriptions of slug flow, but this requires additional information, such as the translational slug velocities, which needs to be measured in advance [50]. Furthermore, these methods require specific data, which differ in its type for the temporal or spatial quantification of slug flow.

In this context, the snapshot Proper Orthogonal Decomposition is considered, which has been proven as a robust and objective method for the temporal and spatial quantification of coherent structures in single phase flows from spatio-temporal data sets. Thus, it has the potential to provide a robust and objective description for the temporal and spatial features of horizontal slug flow from a single spatially and temporally resolved data set, such as a snapshot sequence of phase volume fraction fields or video recordings (see Section 1.4).

In that regard, a novel approach for the quantification of horizontal slug flow with snapshot POD is investigated in this thesis. This includes the aspect of the representation of the slugs in the POD modes, the derivation of the spatial and temporal characteristics of slug flow from the POD-modes and the data requirements for this application.

In the course of these investigations, an approximation of the liquid level time series as well as time scales of slug flow have been derived from video recordings. Typically, such video-based approaches have been used for counting slugs [67] as well as determining geometrical properties of the slugs and bubbles [64]. An approximation of the liquid level time series and a derivation of the time scales of the slugs from video observations was not reported in the literature, except in the authors earlier work [62]. For this reason, the plausibility of the temporal quantification of slug flow achieved with this new procedure needs to be investigated. In that regard, the temporal quantification of slug flow from video observations are assessed in a further examination, where parameters from an established tomography measurement technique are used as a reference.

If only a pure temporal characterization of slug flow is needed, or the spatial scales of the slugs do not allow a direct characterization from video observations, a fast and reliable non-intrusive method for the approximation of the liquid level time series from video data can serve as a useful tool in related industrial and academic operations. The achieved temporal quantification helps to assess not only slug flow, but also other separated and intermittent flow patterns and do not require intrusive as well as costly non-intrusive measurement techniques, such as wire-mesh sensors or tomography measurements, respectively. In that regard, a novel deep learning based image processing technique is presented and the accurate and efficient extraction of the liquid level time series from video observations of separated and intermittent flow pattern is investigated.

The introduced research objectives, which are adressed in this thesis, are summarized in the following:

1. The quantification of horizontal slug flow with snapshot POD

    a Representation of the slugs in the POD modes.

   b Derivation of time and length scales from the POD modes for the characterization of slug flow.

   c Data requirements for the characterization of slug flow with POD

2. The evaluation of the temporal quantification of slug flow from video observations by using tomography measurements as a reference.

3. Accurate and efficient extraction of the liquid level time series from video observations of multiphase flows with a deep learning model.

These research objectives are addressed in four journal publications, which comprises this thesis. These publications and their contribution to the individual research objectives are presented in Chapter 2. The scientific results presented in the publications are discussed in Chapter 3 in the context of the research objectives.

2

Publications

This chapter contains the publisher-versions of the four journal publications in chronological order. In these publications, the scientific results of the investigations are presented, which address the research objectives of this thesis (see Section 1.5). This includes the quantification of horizontal slug flow with snapshot POD (see Publication I and II), the evaluation of the temporal quantification of slug flow from video observations by using tomography measurements as a reference (Publication III), and the accurate and efficient extraction of the liquid level time series from video observations of multiphase flows with a deep learning model (see Publication IV). A short summary for each of the four journal publications and their contribution to the different research objectives are given in advance, prior to each article. This thesis is comprised of the following for publications:

Publication I

M. Olbrich, E. Schmeyer, M. Bär, M. Sieber, K. Oberleithner, S. Schmelter, "Identification of coherent structures in horizontal slug flow". In: *Flow Measurement and Instrumentation* 76 (2020), p. 101814, ISSN 0955-5986, https://doi.org/10.1016/j.flowmeasinst.2020.101814.

Publication II

M. Olbrich, M. Bär, K. Oberleithner, S. Schmelter, "Statistical characterization of horizontal slug flow using snapshot proper orthogonal decomposition". In: *International Journal of Multiphase Flow* 134 (2021), p. 103453, ISSN 0301-9322, https://doi.org/10.1016/j.ijmultiphaseflow.2020.103453.

Publication III

M. Olbrich, A. Hunt, T. Leonard, D. S. van Putten, M. Bär, K. Oberleithner, S. Schmelter, "Comparing temporal characteristics of slug flow from tomography measurements and video observations". In: *Measurement: Sensors* 18 (2021), p. 100222, ISSN 2665-9174, https://doi.org/10.1016/j.measen.2021.100222.

Publication IV

M. Olbrich, L. Riazy, T. Kretz, T. Leonard, D. S. van Putten, M. Bär, K. Oberleithner, S. Schmelter, "Deep learning based liquid level extraction from video observations of gas–liquid flows". In: *International Journal of Multiphase Flow* 157 (2022), p. 104247, ISSN 0301-9322, https://doi.org/10.1016/j.ijmultiphaseflow.2022.104247.

2.1 Publication I

Identification of coherent structures in horizontal slug flow

The snapshot Proper Orthogonal Decomposition has been proven as a robust and objective method for the temporal and spatial quantification of coherent structures in single phase flows from spatio-temporal data sets. Thus, it has the potential to provide a robust and objective description for the temporal and spatial features of horizontal slug flow. In that regard, a novel approach for the quantification of horizontal slug flow with snapshot POD is investigated in this publication, with the particular focus on the representation of the slugs in the POD modes and their characterization (research objective Nr. 1a and b). For this, two different instances of horizontal slug flow are investigated with snapshot proper orthogonal decomposition and an additional mode coupling algorithm. At first, an operationally induced air-water slug flow from a numerical simulation is considered, where the slugs occur in a periodic manner with a fixed frequency of 1 Hz at the point of observation. For this instance, temporally and spatially resolved phase volume fraction fields from a longitudinal section along the vertical centerline of a pipe segment are used. Furthermore, a nitrogen-brine water slug flow with hydrodynamic slugging from an experiment is considered, where the slugs occur intermittently at the point of observation. For this, temporally and spatially resolved gray intensity fields from video recordings of the flow from the side are used.

For both slug flows, it is shown that the dynamics of one of the temporal coefficients from the most dominant pair of POD modes coincides with the dynamics of the liquid level time series, extracted from the raw data. Thus, it reveals the dynamics of the phase distribution and can therefore be used for a temporal characterization of the slugs.

For the slug flow data from the numerical simulations, the structure displayed in one of the spatial modes of the dominant mode pair shows a strong similarity to the ensemble-averaged slug, derived from the raw data. Thus, it can be used for the spatial characterization of the slugs. In this context, a mean length scale is derived from the spatial mode that approximates the mean slug body length. For the video data from the slug flow experiment, the averaged slug is too long to be displayed entirely in the observed region of interest. Thus, a spatial characterization could not be derived from the spatial mode. Nevertheless, with additional knowledge of the averaged translational velocity of the slugs, it is demonstrated for both instances that a mean length scale for the slugs can be calculated with the approximation of the slug body time from the temporal coefficients.

Altogether, it is shown for the considered slug flow data that the slugs are represented in the dominant mode pair. Furthermore, rough estimates of the temporal and spatial scales were derived from the POD modes.

Flow Measurement and Instrumentation 76 (2020) 101814

Contents lists available at ScienceDirect

Flow Measurement and Instrumentation

journal homepage: http://www.elsevier.com/locate/flowmeasinst

Identification of coherent structures in horizontal slug flow

M. Olbrich [a,b,*], E. Schmeyer [a], M. Bär [a], M. Sieber [b], K. Oberleithner [b], S. Schmelter [a]

[a] Physikalisch-Technische Bundesanstalt (PTB), Abbestr. 2–12, 10587, Berlin, Germany
[b] Institute of Fluid Dynamics and Technical Acoustics, Technische Universität Berlin, Müller-Breslau-Straße 8, 10623, Berlin, Germany

ARTICLE INFO

Keywords:
Slug flow
Coherent structures
Snapshot POD

ABSTRACT

Multiphase flow measurement devices are significantly affected by the flow pattern, such as, e.g., slug flow, leading to large uncertainties. In this context, the slug flow pattern in horizontal pipes is investigated with the aim of finding a statistical characterization of the structures in space and time. For this, two different instances of slug flow are analyzed with a snapshot proper orthogonal decomposition and an additional mode coupling algorithm, which provides an energy-ranked mode basis of the underlying coherent structures. For the considered flows, the most energetic mode pair has been identified with the corresponding slugging structures. Thereby, the temporal and spatial information of these mode pairs enables a statistical characterization of the slugs. In this context, a length scale, a dominant frequency, and an energy representation of the slugging structures are obtained from this method.

1. Introduction

One central aim in multiphase flow metrology is to explain and quantify the large uncertainty in multiphase flow metering that reaches up to 20% in the oil and gas industries [11]. For this, the slug flow pattern in horizontal pipes is of special interest since multiphase flow measurement devices can significantly be affected by liquid slugs and the induced pressure fluctuations and vibrations. A concise description of the slug flow pattern can contribute to the aim of explaining these uncertainties. Therefore, a technique for a quantification of this flow pattern is investigated.

In this contribution, we focus on the analysis of horizontal slug flow by means of snapshot proper orthogonal decomposition (snapshot POD), see, e.g., Ref. [1,3,4], with an additional mode coupling algorithm, as proposed in Ref. [4]. The snapshot POD extracts an energy-ranked mode basis of the coherent structures from the flow data with the aim of representing the relevant flow phenomena (e.g., slugs) by a few elements of the mode basis. This method is applied to spatially and temporally resolved data.

At first, we analyze data obtained from the CFD simulation of an air-water slug flow test case, for which the slugs occur at a fixed frequency of 1Hz [6]. Furthermore, the snapshot POD analysis is applied to data from experimental video observations of a nitrogen - brine water slug flow.

Since the flow pattern is characterized by the distribution of the different phases in the pipe, time-resolved phase volume fraction fields from CFD, as well as gray intensity fields from video observations are used for this analysis.

In both slug flows, the most energetic mode pair from snapshot POD provides a statistical characterization of the slugging structures through their temporal and spatial information.

2. Data analysis methodology

2.1. Snapshot proper orthogonal decomposition

The snapshot proper orthogonal decomposition (snapshot POD) is a modal decomposition and often used for the identification and characterization of coherent structures in turbulent flows, see, e.g., Ref. [1–5].

For the analysis of coherent structures in the slug flow regime, the snapshot POD is applied to spatially and temporally resolved data of this flow pattern. For this, let $g(x,y,t)$ be a snapshot sequence of a two-dimensional scalar field. Then, the data is decomposed as follows

$$g(x,y,t) = \overline{g}(x,y) + g'(x,y,t) = \overline{g}(x,y) + \sum_i a_i(t)\varphi_i(x,y), \quad (1)$$

where $\overline{g}$ denotes the time-averaged data field, g' the corresponding fluctuations, a_i the temporal coefficients and φ_i the spatial modes. Furthermore, a_i and φ_i can be obtained from an eigenvalue

* Corresponding author. Physikalisch-Technische Bundesanstalt (PTB), Abbestr. 2–12, 10587, Berlin, Germany.
E-mail address: marc.olbrich@ptb.de (M. Olbrich).

https://doi.org/10.1016/j.flowmeasinst.2020.101814
Received 2 December 2019; Received in revised form 19 June 2020; Accepted 17 August 2020
Available online 16 October 2020

decomposition of the correlation matrix of the fluctuations g' as follows. Let $G \in \mathbb{R}^{M\times N}$be the matrix of the rearranged fluctuations of the snapshot sequence g' with M rows and N columns, where M denotes the number of spatial points and Ndenotes the number of snapshots. Here, all spatial points of the i-th snapshot are arranged in the i-th column of G. Then a_i and φ_i are obtained from the eigenvalue decomposition of $R := \frac{1}{N}G^TG$:

$$Rv_i = \lambda_i v_i, i = 1, \ldots, N, \ with\ \lambda_1 \geq \ldots \geq \lambda_N \geq 0. \tag{2}$$

Here, the temporal coefficient a_i is given by the scaled eigenvector v_i with respect to the eigenvalue λ_i as,

$$a_i(t) := \sqrt{N\lambda_i}v_i \tag{3}$$

and the spatial mode φ_i is given as

$$\varphi_i(x,y) := \frac{1}{N\lambda_i}\sum_{k=1}^{N} a_i(t_k)g'(x,y,t_k) \tag{4}$$

for $i = 1, \ldots, N$. In the context of fluid dynamics, a temporal coefficient $a_i(t)$ (Equation (3)) can be interpreted as the dynamical behaviour of an underlying coherent structure of the flow field. The corresponding eigenvalue provides a measure of the energy of this coherent structure. The spatial mode $\varphi_i(x,y)$ (Equation (4)) can then be understood as a weighted time-average of the considered flow field fluctuations, weighted with the corresponding dynamics and energy. This provides spatial information of the underlying coherent structure. Further details can be found in Ref. [1,3,4].

2.2. Mode-coupling algorithm

Since the dynamics of periodic structures can be described by a pair of modes, the mode-coupling algorithm proposed in Ref. [4] is used in addition. Related modes are identified by the spectral similarity of their temporal coefficients, which accounts for modes that are shifted by a quarter period. The mode coupling is computed by an additional eigenvalue decomposition

$$Ac_i = \mu_i c_i \tag{5}$$

$$\text{with } A := \begin{bmatrix} a_1^2 & \cdots & a_N^2 \\ \vdots & \ddots & \vdots \\ a_1^N & \cdots & a_N^N \end{bmatrix}^T \cdot \left(\begin{bmatrix} a_1^1 & \cdots & a_N^1 \\ \vdots & \ddots & \vdots \\ a_1^{N-1} & \cdots & a_N^{N-1} \end{bmatrix}^T \right)^+,$$

Where a_i^k denotes the k-th entry of the i-th temporal coefficient a_i and $(\cdot)^+$ denotes the Moore-Penrose pseudo inverse of the corresponding matrix. Note that this is a dynamic mode decomposition (DMD) on the temporal coefficients. The similarity measure of the temporal coefficients a_i and a_j is given by

$$H_{i,j} := \mathrm{Im}\left(\sum_{k=1}^{N} c_k^i \overline{c_k^j} \mathrm{sgn}(\mathrm{Im}(\mu_k)) \right), \tag{6}$$

where $\overline{c_k^j}$ denotes the complex conjugate of c_k^j, Im the imaginary part and sgn the sign function. The matrix H is also called *harmonic correlation matrix*.

The indices of the coupled modes are then given by the indices of the maximal entries of H, since it indicates the temporal coefficients with the highest spectral similarity. The dominant frequency f of an identified mode pair (a_i, a_j) (equivalently denoted by (φ_i, φ_j)) is then derived from the corresponding eigenvalue μ_k (Equation (5)) by

$$f = \frac{\mathrm{Im}(\ln(\mu_k))}{2\pi}. \tag{7}$$

To determine the combined energy content of the mode pair (a_i, a_j) the corresponding eigenvalues of the modal decomposition (see Equation (2)) are summarized as

$$E = \frac{\lambda_i + \lambda_j}{\sum_{l=1}^{N}\lambda_l}. \tag{8}$$

Note that E represents the energy distribution in terms of a discrete time signal. It can only be identified with a physical energy if g has appropriate physical units. For details see Ref. [4].

3. Data of horizontal slug flow

For the analysis of horizontal slug flow with snapshot POD, two different types of slug flow data are considered.

At first, phase volume fraction fields, obtained from the CFD simulation of a periodic air-water slug flow, are used. Because of its periodicity, this flow is suitable for testing the applicability of snapshot POD.

Second, the method is applied to video observations of an experimental nitrogen-brine water slug flow.

3.1. CFD simulation of periodic air-water slug flow

The simulation of an air-water slug flow through a horizontal pipe with an inner diameter of $D = 0.054$m and a length of $L = 8$m, was adopted from Ref. [6]. The fluid properties and superficial velocities of this flow are given in Table 1.

For the computation, the pipe was discretized as an O-grid consisting of about 1.1 million nodes (45 nodes in radial, 104 nodes in angular, and 685 nodes in longitudinal direction).

To generate a periodic formation of slugs in the pipe, a time-dependent sinusoidal displacement of the vertical position of the air-water interface is applied to this flow as introduced in Ref. [6]. For this, the inlet is initialized with equally distributed phases in the inlet cross section, such that the lower half of the cross section is filled with water and the upper half is filled with air (see Fig. 1). The initial condition is obtained from the vertical position of the interface $\tilde{y}_{int}$ by

$$\tilde{y}_{int}(x, t=0) = \frac{D}{4}\sin\left(2\pi\frac{4x}{L}\right) + \frac{D}{2}, \tag{9}$$

where t denotes the time and x the spatial component in flow direction (see Fig. 1). The time-dependent vertical position of the interface at the inlet is then given by

$$\tilde{y}_{int}(x=0, t) = \frac{D}{4}\sin\left(2\pi\frac{v4t}{L}\right) + \frac{D}{2}, \tag{10}$$

where $v = 2\frac{\mathrm{m}}{\mathrm{s}}$ denotes the inlet gas or liquid velocity. This perturbation leads to a periodical slug formation in the pipe of 1 Hz (see Fig. 2).

Furthermore, a no-slip boundary condition at the walls of the pipe and a pressure outlet boundary condition was set.

The CFD simulation was performed in ANSYS FLUENT [7]. For this, an unsteady Reynolds-averaged Navier-Stokes (URANS) approach with the k-ω-SST turbulence model was chosen [8].

To model the gas-liquid interface the volume of fluid (VOF) method was applied within a mixture model [9]. In addition, turbulence damping was included to model such flows with high velocity gradients at the interface correctly [10]. The space and time discretization schemes are chosen as in Ref. [12].

Table 1
Fluid properties and superficial vel. for CFD.

	water	air
density in $\frac{\mathrm{kg}}{\mathrm{m}^3}$	998.2	1.225
dyn. viscosity in Pa·s	1.003×10^{-3}	1.789×10^{-5}
superficial vel. in $\frac{\mathrm{m}}{\mathrm{s}}$	1.0	1.0

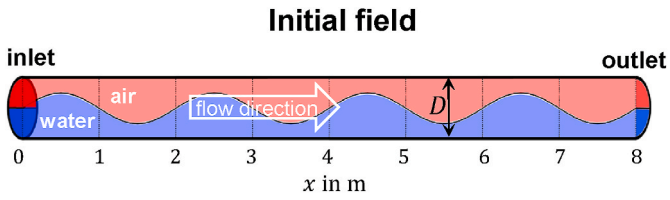

Fig. 1. Illustration of the initial field (not to scale).

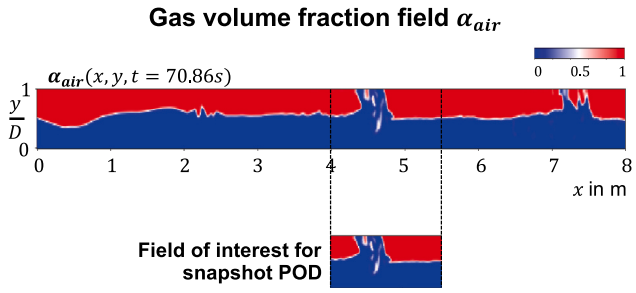

Fig. 2. Snapshot of gas volume fraction field from a longitudinal pipe section at $t = 70.86s$ with exposed field of interest (not to scale).

In Fig. 2, a snapshot of the gas volume fraction field $\alpha_{air}(x, y, t)$ from a longitudinal section of the pipe at $t = 70.86$s is depicted. Here, the time-dependent interface displacement at the inlet is visible along the first few metres of the pipe. Further downstream the water slugs are formed.

To analyze the fully developed slug flow from the simulations with snapshot POD, the gas volume fraction field data is collected from a longitudinal section of a 1.5m long pipe segment at 4– 5.5m (see Fig. 2). To ensure that numerical effects from the initialization do not affect the flow field anymore and the simulated flow is well developed, the snapshot sequence is collected in a time interval of 10s from 70s to 80s with a sample rate of 100Hz (see Fig. 3).

3.2. Experimental slug flow

The considered experiment of a horizontal gas-liquid slug flow was performed by TUV SUD NEL. The experimental setup consists of a straight horizontal pipe with an inner diameter of $D = 0.0972$m and a length of 100D, followed by a Perspex viewing section with a length of 0.5m, where the slug flow was recorded from aside by a high-speed camera with a frame rate of 240fps. This section is followed by a right-angled bend connected to a vertical measurement configuration [11], but this is of minor interest, since the slugging structures in the horizontal pipe are investigated. The fluid properties and superficial velocities are listed in Table 2.

To obtain a scalar field representation of the multidimensional RGB-frames from the video, the grayscale is extracted. A snapshot sequence of these grayscale frames for a time interval of 50s is then used for the analysis with snapshot POD (see Fig. 3).

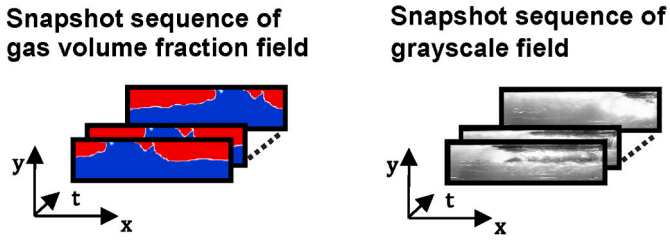

Fig. 3. Illustration of snapshot sequences from CFD data (left) and grayscale frames of experimental videos (right).

Table 2
Fluid properties and superficial vel. for experiment.

	Brine water	nitrogen
density in $\frac{kg}{m^3}$	1011	10.8
dyn. viscosity in $Pa{\cdot}s$	$8.82{\times}10^{-4}$	$1.75{\times}10^{-5}$
superficial vel. in $\frac{m}{s}$	0.545	1.635

4. Results

In this chapter, the results of the snapshot POD analysis of the flow field data from CFD and experimental video observations are presented. Since this work focuses on a statistical characterization of the slugging structures, only the relevant results are selected. For both data sets, the coherent structures, represented by the most energetic mode pair can be identified with the slugging structures of the corresponding slug flow. Hence, this mode pair provides spatial and temporal parameters for a characterization of the slugging structures. For a validation of this identification, the statistical length and time scales of the flow are compared with the length and time scales that were derived from the snapshot POD results.

4.1. Results for CFD data

In Fig. 4, the most energetic mode pair of the air-water slug flow from CFD, as well as the corresponding temporal coefficients and the time-averaged gas volume fraction field are depicted as the results of the analysis with snapshot POD. In addition, the vertical position of the gas-liquid interface (liquid level) over time and the averaged slugging structure are also given for a visual comparison. The liquid level was extracted from the snapshot sequence at $x = 13.9D$ with the method of tracking the gas-liquid interface described in Ref. [13]. The averaged slugging structure was obtained from the mean of all snapshots with a slug (at centered position). Due to the eigenvalue decomposition of the gas volume fraction field in the POD algorithm, the absolute values of the single spatial modes are not in the same range as the gas volume fraction. For consistency in Fig. 4, the spatial modes were normalized to the range of the gas volume fraction as follows

$$\widehat{\varphi}_i = \frac{\varphi_i - \min(\varphi_i)}{\max(\varphi_i) - \min(\varphi_i)} \tag{11}$$

This mode pair is identified with the averaged slugging structure of the corresponding air-water slug flow, since the temporal coefficients coincides with the liquid level, especially in width and periodicity of the spikes. Note that a_1 is shifted to a_2 as stated in Chapter 2. Furthermore, the frequency of the coupled mode pair (φ_1, φ_2) of 1Hz (see Equation (8)) is equal to the frequency of slug occurrence of the periodic slug flow. The structure displayed in the spatial mode $\varphi_2(x, y)$ is interpreted as the averaged slugging structure. This can be verified by the averaged slug, which is also depicted in Fig. 4. From that, the slug body length L_s can be derived [14–16]. Here, the averaged slug body length derived from the spatial mode $\varphi_2(x, y)$ is given by $L_s^{POD} = 6.5D$, whereas the averaged slug body length derived from the averaged slug of the flow data is given by $L_s = 6D$. This length scale and the slug frequency f provide parameters for a statistical characterization of the slug flow.

Furthermore, an additional length scale L^* can be obtained from a_2 as proposed in Ref. [2], where the similarity between one of the dominant temporal coefficients and the liquid holdup was mentioned. For this, the transitional velocity of a slug v_s is multiplied by the time interval of a slug Δt_s passing by at one point, i.e.:

$$L^* = v_s \cdot \Delta t_s. \tag{12}$$

Based on the unit cell model [14] and the considered specific rectangular shape of a slug, this length scale is often used for the calculation

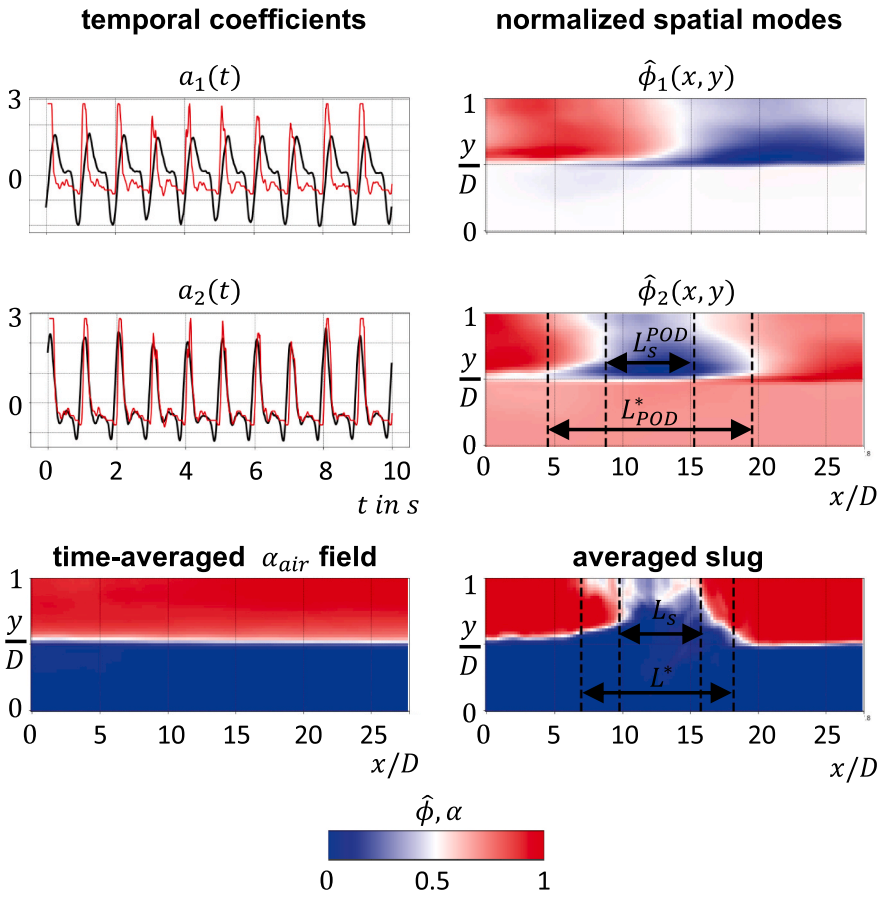

Fig. 4. Most energetic mode pair (φ_1, φ_2) with corresponding temporal coefficients $\boldsymbol{a}_1, \boldsymbol{a}_2$(—) from snapshot POD in comparison with liquid level over time (—), the averaged slug and the time-averaged gas volume fraction field $\overline{\boldsymbol{\alpha}}_{\boldsymbol{air}}$, obtained from CFD data. In addition, the derived length scales $\boldsymbol{L_s}, \boldsymbol{L^*}, \boldsymbol{L_s^{POD}}, \boldsymbol{L_{POD}^*}$ are given. Note that $\boldsymbol{a}_1, \boldsymbol{a}_2$ and the liquid level are depicted in standard score, respectively. Drawings not to scale.

of the slug body length, see Ref. [15]. But for slugs, which deviate much in their shape from the unit cell model, this identification is not obvious. Since on strongly tilted slugging structures as in Fig. 4, it is not clear how to determine a unique time of a slug front and a slug tail. Nevertheless, the length scale L^* can be obtained from the liquid level over time as well as the temporal coefficient a_2 (denoted by L^*_{POD}) under knowledge of v_s, since it depends only on temporal information and a velocity. Considering the liquid level time series, a spike with a large amplitude close to $y/D = 1$ indicates a slug, where the beginning and the end of the spike are given by the corresponding local minima. Then, the obtained length scale L^* provides an information of the length of the complete structure, and not just the inner part of the slug body. To determine L^*, average parameters are considered, since a statistical characterization is sought. For this, the averaged translational velocity of the slugs is obtained by a cross-correlation of a column of the field of interest at $x_1 = 0D$ and $x_2 = 27.8D$ over time. Since the distance is known, the average velocity of the slugs is then derived by the shift of the data obtained by the (unique) maximum of the cross-correlation function. This procedure is adopted from the PIV-measurement technique, see, e.g., Ref. [17]. This leads to an average translational velocity $\overline{v}_s = 2.63\frac{m}{s}$ of the slugging structures.

Considering the liquid level over time in standard score, the time interval of a slug Δt_s is approximated by the width of the associated spike from zero to zero. Taking the mean of all these intervals, the average time interval $\overline{\Delta t}_s = 0.23s$ can be derived from the liquid level time series. This results in a length scale for the averaged slugging structure of about $L^* = 11.2D$, which matches the length of the average slug shown in Fig. 4. Since the temporal coefficient a_2 represents the dynamics of the liquid level, an approximation of these parameters can also be derived from a_2, resulting in $\overline{\Delta t}_s^{POD} = 0.31s$ and $L^*_{POD} = 15.1D$, which also matches the length of the blurred slugging structure shown in φ_2 (see Fig. 4). The parameters for a statistical characterization of the slugs obtained from analysis with snapshot POD are summarized in Table 3.

4.2. Results for experimental data

In Fig. 5, the most energetic mode pair of the experimental nitrogen - brine water slug flow, as well as the corresponding temporal coefficients are depicted as result of the analysis with snapshot POD. Analogously to Fig. 4, the liquid level over time, obtained from the experimental video observations with the same method as mentioned in Section 4.1, see Ref. [13], is plotted for comparison.

Since a snapshot sequence of grayscale fields are analyzed, the modal decomposition accounts for the changes in the gray intensities. For the considered flow, the brine water shows higher gray intensities than the transparent nitrogen in front of the dark background. But the highest gray intensities appear at the gas-liquid interface, due to reflection at the

Table 3
Parameters for statistical characterization of air-water slug flow from CFD data derived from snapshot POD results.

Coupled energy content $\boldsymbol{E}$ of mode pair (φ_1, φ_2) (see Equation (8))	46.6%
Frequency f of mode pair (φ_1, φ_2) (see Equation (7)) (Identified with slugging frequency)	1Hz
Averaged slug body length $\boldsymbol{L_s^{POD}}$	$6.5D$
Averaged structure length $\boldsymbol{L_{POD}^*}$	$15.1D$

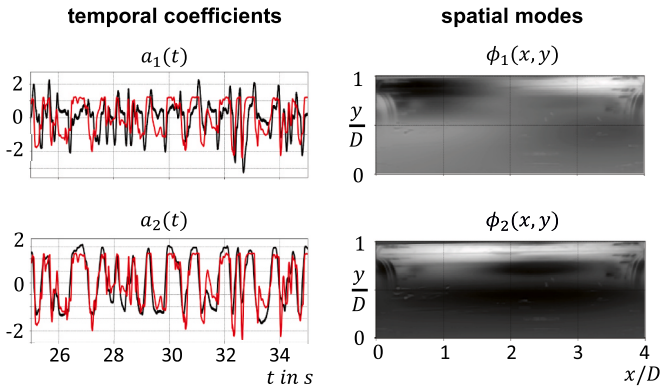

Fig. 5. Most energetic mode pair (φ_1, φ_2) with corresponding temporal coefficients $\boldsymbol{a}_1, \boldsymbol{a}_2$(—) from snapshot POD in comparison with liquid level over time (—). Note that $\boldsymbol{a}_1, \boldsymbol{a}_2$and the liquid level are depicted in standard score for a 10s time interval $[25s, 35s]$, respectively. Drawing of φ_1, φ_2 not to scale.

liquid surface. Hence, the spatial modes show coherent structures of the flow in terms of gray intensities, but with a highlighted gas-liquid interface.

The depicted mode pair (see Fig. 5) is also identified with the averaged slugging structure because of the clear similarity of the liquid level with the corresponding temporal coefficients and the shape of the spatial modes. Since the gas-liquid interface in φ_2 occupies the complete length of the field of view, it can be deduced, that the average slug is at least as long as the field of view. Therefore, an average slug body length scale L_s cannot be derived from the spatial mode. Nevertheless, the length scale $L^*_{POD} = 7.6$D can be derived from the temporal coefficient a_2, as well as $L^* = 6.7D$ from the liquid level over time. For this, the averaged translational velocity $\overline{v}_s = 2.85\frac{m}{s}$ and the averaged time interval $\overline{\Delta t_s}^{POD} = 0.26$s and $\overline{\Delta t_s} = 0.23$s are obtained as explained before in Section 4.1. Furthermore, the dominant frequency f and the energy content E of the selected mode pair is also provided by snapshot POD analysis. These parameters can be used for a statistical characterization of the slugging structures and are summarized in Table 4. Note that the dominant frequency $f = 1.4$Hz agrees with the averaged frequency of slug occurrence, where the number of counted slugs (72) is divided by the length of the considered time interval (50s).

5. Conclusion

To characterize the structures of two different slug flows statistically, an analysis with snapshot POD was performed and validated. For both examples, the most energetic mode pair was identified with the slugging structures and used for their characterization in space and time. Altogether, the snapshot POD with an additional mode coupling algorithm is a valid tool for the identification of coherent structures in horizontal slug flow and enables a quantitative characterization of the occurring liquid slugs by their temporal and spatial information.

Table 4
Parameters for statistical characterization of nitrogen – brine water slug flow from experimental data derived from snapshot POD results.

Coupled energy content $\boldsymbol{E}$ of mode pair (φ_1, φ_2) (see Equation (8))	55.9%
Frequency $\boldsymbol{f}$ of mode pair (φ_1, φ_2) (see Equation (7)) (Identified with slugging frequency)	1.4Hz
Averaged structure length $\boldsymbol{L^*_{POD}}$	7.6D

Credit author statement

M. Olbrich: Conceptualization, Methodology, Investigation, Software, Validation, Formal analysis, Visualization, Writing - Original Draft; E. Schmeyer: Software, Investigation; M. Bär: Conceptualization, Validation, Supervision, Writing - Review & Editing; M. Sieber: Methodology, Validation, Writing - Review & Editing; K. Oberleithner: Conceptualization, Validation, Supervision, Writing - Review & Editing; S. Schmelter: Conceptualization, Methodology, Investigation, Software, Validation, Supervision, Writing - Review & Editing.

Declaration of competing interest

The authors declare that they have no known competing financial interests or personal relationships that could have appeared to influence the work reported in this paper.

Acknowledgements

This work was supported through the Joint Research Project “Multiphase flow reference metrology”. This project has received funding from the EMPIR programme co-financed by the Participating States and from the European Union’s Horizon 2020 research and innovation programme. The authors would like to thank Terri Leonard and Marc MacDonald from TUV SUD NEL, who provided the experimental video observations.

Nomenclature

A, G, R	real valued matrices
D	inner pipe diameter
E	energy content of a corresponding mode pair
H	harmonic correlation matrix
L	pipe length
L_s	averaged slug body length derived from snapshot sequence
L_s^{POD}	averaged slug body length derived from spatial mode of snapshot POD
L^*	average slug structure length derived from liquid level time series
L^{*POD}	averaged slug structure length derived from temporal coefficient of snapshot POD
M	number of spatial points
N	number of snapshots
$a_i(t)$	i-th temporal coefficient
c_i	i-th eigenvector of A
f	dominant frequency of a corresponding mode pair
$g(x,y,t)$	snapshot sequence of a two-dimensional scalar field
$\overline{g}(x,y)$	temporal mean of $g(x,y,t)$

$g'(x,y,t)$	temporal fluctuations of $g(x,y,t)$
t	time variable
v_i	i-th eigenvector of R
$\bar{v}_s$	averaged translational velocity of the slugs
x,y	space variables
$\tilde{y}_{int}(x,t)$	sinusoidal interface displacement
$\alpha_{air}(x,y,t)$	gas volume fraction field
$\overline{\alpha}_{air}$	temporal mean of α_{air}
$\overline{\Delta t_s}$	averaged time interval of slugs passing by at one position derived from liquid level time series
$\overline{\Delta t_s}^{POD}$	averaged time interval of slugs passing by at one position derived from temporal coefficient of snapshot POD
λ_i	i-th eigenvalue of R
μ_i	i-th eigenvalue of A
$\phi_i(x,y)$	i-th spatial mode
$\widehat{\phi}_i(x,y)$	normalization of $\phi_i(x,y)$

References

[1] K. Taira, S.L. Brunton, S.T.M. Dawson, C.W. Rowley, T. Colonius, B.J. McKeon, O. T. Schmidt, S. Gordeyev, V. Theofilis, L.S. Ukeiley, Modal analysis of fluid flows: an overview, AIAA J. 55 (2017).

[2] B. Viggiano, O. Skjraasen, H. Schmann, M. Tutkun, R.B. Cal, Characterization of flow dynamics and reduced-order description of experimental two-phase pipe flow, Int. J. Multiph. Flow 105 (2018) 91–101.

[3] L. Sirovich, Turbulence and the dynamics of coherent structures. Part I: coherent structures, Q. Appl. Math. 45 (1987).

[4] M. Sieber, C. Paschereit, K. Oberleithner, "Spectral proper orthogonal decomposition", J. Fluid Mech. 792 (2016) 798–828.

[5] J. Polanski, M. Wang, Proper orthogonal decomposition as a technique for identifying two-phase flow pattern based on electrical impedance tomography, Flow Meas. Instrum. 53 (2016) 126–132.

[6] Frank T, "Numerical simulation of slug flow regime for an air-water two phase flow in horizontal pipes", in: The 11th International Topical Meeting on Nuclear Reactor Thermal-Hydraulics (NURETH-11), (Avignon, France).

[7] Fluent Inc., Fluent User's Guide 16.0, 2015.

[8] F.R. Menter, Two-equation eddy-viscosity turbulence models for engineering applications, AIAA J. 32 (1993).

[9] C.W. Hirt, B.D. Nichols, Volume of fluid method for the dynamics of free boundaries, J. Comput. Phys. 39 (1981) 201–225.

[10] Y. Egorov, Validation of CFD codes with PTS-relevant test cases, EVOL-ECORA-D07 (2004).

[11] Final Publishable JRP Report Multiphase Flow Metrology in Oil and Gas Production (ENG58), Euramet, 2018.

[12] A. Fiebach, E. Schmeyer, S. Knotek, S. Schmelter, Numerical simulation of multiphase flow in a vertically mounted Venturi flow meter, in: Proceedings of FLOMEKO, 2016.

[13] M. Olbrich, E. Schmeyer, L. Riazy, K. Oberleithner, M. Bär, S. Schmelter, Validation of simulations in multiphase flow metrology by comparison with experimental video observations, IOP Conf. Series: J. Phys. Conf. 1065 (2018).

[14] Y. Taitel, D. Barnea, A consistent approach for calculating pressure drop in inclined slug flow, Chem. Eng. Sci. 45 (1990) 1199–1206.

[15] H.H. Al-Kayiem, A.O. Mohmmed, Z.I. Al-Hashimy, Time R W, "Statistical assessment of experimental observation on the slug body length and slug translational velocity in a horizontal pipe", Int. J. Heat Mass Tran. 105 (2017) 252–260.

[16] Y.D. Baba, A.M. Aliyu, A.E. Archibong, M. Abdulkadir, L. Lao, H. Yeung, Slug length for high viscosity oil-gas flow in horizontal pipes: experiments and prediction, J. Petrol. Sci. Eng. 165 (2018) 397–411.

[17] C. Brossard, J.-C. Monnier, P. Barricau, F.-X. Vandernoot, Y. Le Sant, F. Champagnat, G. Besnerais, Principles and applications of particle image velocimetry, AerospaceLab J. (2009).

2.2 Publication II

Statistical characterization of horizontal slug flow using snapshot proper orthogonal decomposition

The analysis of horizontal slug flow with snapshot Proper Orthogonal Decomposition is deepened in this publication, based on the findings of Publication I (see Section 2.1). The representation of the slugs in the POD modes (research objective 1a) is further investigated, especially for the video data. Precise characterizations of the slugs are derived from the POD modes (research objective 1b) and the data requirements for a meaningful characterization of the slugs with snapshot POD (research objective 1c) are investigated.

In a first step, phase volume fraction fields of the same periodic slug flow from a numerical simulation are analyzed as in Publication I (see Section 2.1). For the dominant mode, which represents the slugs, it was found that the corresponding standardized temporal coefficient approximates best the standardized liquid level time series extracted at exactly that streamwise position in the region of interest, where the liquid intensity in the corresponding spatial mode is maximal. This fact contributes to a better understanding of the representation of the slugs in the POD modes and their characterization. Moreover, it enables a detailed validation of the representation of the slugs in the POD modes. The influence of the length of the observed pipe segment on this representation was further investigated. It was found that the accuracy of the representation of the liquid level time series in the temporal coefficient decreases in general with increasing length of the observed pipe segment. A similar behavior was noticed for the representation of the averaged slug in the spatial modes. Based on this analysis, the required length of the observed pipe segment for a meaningful temporal and spatial characterization of slug flow with snapshot POD was discussed. It was found that the length should be large enough to display the entire (averaged) slug, but also sufficiently small to avoid larger errors of its representation in the POD modes. In contrast to this, for a pure temporal characterization with the temporal coefficient, the length should be as small as possible. Furthermore, an optimal length of the observed pipe segment for the analysis of the considered data set with snapshot POD was found by a detailed error analysis. With this, a precise description of the slugs was derived from the dominant mode pair, including the common statistical time and length scales of slug flow, e.g., mean slug frequency and mean slug body length.

In a second step, RGB-intensity fields from highspeed video recordings of a gas - oil slug flow with hydrodynamic slugging from an experiment are analyzed. In this case, the length of the observed pipe segment is too small to display the entire averaged slug, similar to the experimental data in Publication I (see Section 2.1). Therefore, an artificial extension of the region of interest was developed that embeds frames next to time-shifted frames from the same video such that the averaged slug is visible entirely in the extended region of interest. This extension procedure is applied to the considered slug flow data set in a pre-processing step to enable also a spatial characterization of the slugs with snapshot POD. Based on the findings from the previous investigations, it is demonstrated that a precise statistical characterization of slug flow in space and time can also be derived from the dominant mode pair of a snapshot POD analysis for the considered video data from a slug flow experiment.

It was also discussed that, in general, the energy-representations of the POD modes correspond to the mean fluctuating intensities in the data. Moreover, the mean slug frequency is not represented in general by the mean frequency of the mode pair, which correspond to the mean dominant frequency of the temporal coefficients.

Altogether, in this publication was shown that the slugs are represented in the dominant mode pair of a snapshot POD analysis and that a precise statistical description of the slugs in space and time can be derived from this mode pair, at least if certain data requirements are fulfilled. Moreover it is demonstrated that snapshot POD provides this statistical characterization not only for the high quality phase volume fraction fields from a numerical simulation, but also for RGB-values of a noise-affected experimental video recording.

International Journal of Multiphase Flow 134 (2021) 103453

Contents lists available at ScienceDirect

International Journal of Multiphase Flow

journal homepage: www.elsevier.com/locate/ijmulflow

Statistical characterization of horizontal slug flow using snapshot proper orthogonal decomposition

Marc Olbrich[a,b,*], Markus Bär[a], Kilian Oberleithner[b], Sonja Schmelter[a]

[a] Physikalisch-Technische Bundesanstalt (PTB), Abbestr. 2-12, Berlin 10587, Germany
[b] Institute of Fluid Dynamics and Technical Acoustics, Technische Universität Berlin, Müller-Breslau-Straße 8, Berlin 10623, Germany

ARTICLE INFO

Article history:
Received 3 March 2020
Revised 11 August 2020
Accepted 27 August 2020
Available online 6 September 2020

Keywords:
Slug flow
Characterization
Proper orthogonal decomposition

ABSTRACT

Slug flow is an intermittent and complex gas-liquid flow pattern, that can cause severe problems in industrial operations and lead to large uncertainties in multiphase flow metering. These problems are primarily caused by the liquid slugs of the flow. In this context, different cases of slug flow in horizontal pipes are investigated to find a statistical characterization of the slugs in time and space. To achieve this, snapshot proper orthogonal decomposition (snapshot POD) with an additional mode coupling algorithm is employed, which provides an energy-ranked mode basis of the underlying coherent structures. It is shown that the characterization for the considered slug flows can be derived from the temporal and spatial information of the dominant mode pair. In that regard, the slug frequencies, the averaged slug body length and an energy representation of the slugs are obtained from this method. Furthermore, the accuracy of this characterization is shown and the influence of the size of the observed pipe section on its reliability is investigated.

1. Introduction

Multiphase flow metrology is subject to large uncertainties in flow metering, which typically reach values of up to 20% in the oil and gas industries (ENG, 2018). This also applies to the slug flow pattern since it is one of the most common gas-liquid flow regimes in multiphase transportation pipelines (Al-Kayiem et al., 2017). Furthermore, the piping and the multiphase flow measurement devices can significantly be affected by liquid slugs and the induced pressure fluctuations and vibrations (Hanratty, 2013). Therefore, a detailed investigation of the slug flow pattern in horizontal pipes is of special interest.

The slug flow pattern is characterized by a continuous liquid phase with coherent blocks of aerated liquid, which are separated by volumes of gas and moving on top of a slowly flowing liquid layer downstream the pipe at approximately the same velocity as the gas (Hanratty, 2013; Taitel and Dukler, 1977; Al-Safran, 2009), as shown in Fig. 1. These aerated liquid blocks are called slugs or slug structures. They are typically quantified by their length scales, such as slug body length L_s and slug unit length L_u, and corresponding time scales, such as slug frequency $f_s = T_s^{-1}$, where T_s is the time of a slug unit passing by at a fixed position (Al-Kayiem et al., 2017; Baba et al., 2018), as illustrated in Fig. 1. With this time scale, an averaged slug frequency can be calculated by

$$\bar{f}_s = \frac{1}{\bar{T}_s} \text{ with } \bar{T}_s = \frac{1}{N_s}\sum_{i=1}^{N_s} T_{s_i}, \tag{1}$$

where N_s denotes the number of slugs in the considered time interval (Dukler and Fabre, 1994).

Based on the slug initiation mechanism, slug flow in pipes can be classified into different categories, such as hydrodynamic and operationally induced slugging (Lu, 2015; Al-Safran, 2009). Generally, hydrodynamic slugging is intermittent and caused by instabilities at the stratified gas-liquid interface. Due to the inertia of the liquid and shear stress at the gas-liquid interface, waves form and grow to a sufficient height to fill the complete pipe cross section locally with liquid and block the gas flow. This blockage of liquid is then accelerated by the faster gas flow to form a slug. On the other hand, operationally induced slug flow is caused by operational transients and perturbations. In general, slug flow is a complex gas-liquid flow pattern, which leads to severe problems in industrial operations. The slugs can grow to large structures, moving at high velocities. So, they can have large momentum. This can induce stresses and vibrations, when they impact at surfaces of the piping (Hanratty, 2013). Furthermore, the pressure drop due to slug

* Corresponding author.
E-mail address: marc.olbrich@ptb.de (M. Olbrich).

https://doi.org/10.1016/j.ijmultiphaseflow.2020.103453

flow can be an order of magnitude higher, compared to other gas-liquid flow patterns (Taitel and Dukler, 1977).

These problems, as well as the high uncertainties in flow metering, are caused by the intermittent sequence of slugs moving along the pipe. To find solutions and gain understanding for such phenomena, it is essential to quantify these slug structures. In this paper, the method called *snapshot proper orthogonal decomposition* (snapshot POD) was implemented to achieve this quantification since it provides a statistical characterization of the slugs in space and time.

The snapshot POD is a modal decomposition, which extracts an energy-ranked mode basis of the coherent structures from the flow data. It is often used for the identification and characterization of coherent structures in singlephase turbulent flows (Sirovich, 1987; Lumley, 1967; Sieber et al., 2017). For multiphase flows, there are only a few references on POD. In Munir et al. (2015), POD was used to identify coherent turbulent structures, such as eddies, in gas-liquid flow. In Wang et al. (2016); Polansky and Wang (2017, 2018); Viggiano et al. (2018), POD was used for reduced order modelling with the aim of recognizing different flow patterns as well as the transition between them. In this context, the analyses were usually performed on cross-sectional measurements of the phase distribution in the pipe. Measured flow data were approximated by a reduced order model based on a small number of POD modes, which capture the dominant behavior of the flow pattern. In Viggiano et al. (2018), POD was applied to cross sectional tomography measurements of horizontal slug flow. They found a strong correlation between the temporal coefficient of a dominant POD mode and the liquid holdup in the pipe. From that, a timescale was derived to characterize the slugs. In summary, POD was used to find a low order description of large and complex multiphase flow data and to characterize horizontal slug flow in time.

In this contribution, the focus is not only on a temporal, but also on a spatial characterization of slug flow, derived from POD. For this, snapshot POD with an additional mode coupling algorithm (Sieber et al., 2017) is applied to data from horizontal slug flows using longitudinal sections of the pipe and observations from the side. In our previous work (Olbrich et al., 2019), the identification of the underlying coherent structure of the most dominant mode pair from snapshot POD with the slug structures were proposed and a characterization was attempted. The aim of this work is a detailed validation of the time and length scales of the slugs, which can be derived from the temporal coefficients and spatial modes of the most dominant mode pair. This validation is performed on data for an operationally induced periodic slug flow from a numerical simulation, as well as for a non-periodic experimental slug flow with hydrodynamic slugging.

2. Methods

2.1. Snapshot proper orthogonal decomposition

For the analysis of coherent structures in the slug flow regime, the snapshot POD is applied to spatially and temporally resolved data of this flow pattern. For this, let $(g(x,y,t_k))_{k=1,\dots,N}$ be a snapshot sequence of scalar or vector field on a two dimensional domain, considered as an XY-plane. Then, the data is decomposed as follows

$$g(x,y,t_k) = \bar{g}(x,y,t_k) + g'(x,y,t_k) = \bar{g}(x,y,t_k) + \sum_i a_i(t_k)\phi_i(x,y), \tag{2}$$

where $\bar{g}$ denotes the time-averaged data field, g' the corresponding fluctuations, a_i the ith temporal coefficient and ϕ_i the ith spatial mode. Furthermore, a_i and ϕ_i can be obtained from an eigenvalue decomposition of the correlation matrix of the fluctuations g' as follows. Let

$$G := \begin{bmatrix} g'(x_1,y_1,t_1) & \cdots & g'(x_1,y_1,t_N) \\ g'(x_1,y_2,t_1) & \cdots & g'(x_1,y_2,t_N) \\ \vdots & & \vdots \\ g'(x_1,y_{M_y},t_1) & \cdots & g'(x_1,y_{M_y},t_N) \\ \\ \vdots & & \vdots \\ g'(x_{M_x},y_1,t_1) & \cdots & g'(x_{M_x},y_1,t_N) \\ g'(x_{M_x},y_2,t_1) & \cdots & g'(x_{M_x},y_2,t_N) \\ \vdots & & \vdots \\ g'(x_{M_x},y_{M_y},t_1) & \cdots & g'(x_{M_x},y_{M_y},t_N) \end{bmatrix} \in \mathbb{R}^{M\times N} \tag{3}$$

be the matrix of the rearranged scalar field snapshot sequence, where $M = M_x \cdot M_y$ denotes the amount of spatial points of the domain and N the amount of snapshots. For a snapshot sequence of a vector field, every component is rearranged as above and stacked to obtain G (Taira et al., 2017). Hence, all spatial points of the ith snapshot are arranged in the ith column of G. Then a_i and ϕ_i are obtained from the eigenvalue decomposition of $R = \frac{1}{N}G^TG$:

$$Rv_i = \lambda_i v_i, \quad \text{for } i = 1,\dots,N \text{ with } \lambda_1 \geq \cdots \geq \lambda_N \geq 0. \tag{4}$$

Here, the temporal coefficient a_i is given by the scaled eigenvector v_i with respect to the eigenvalue λ_i as,

$$a_i := \sqrt{N\lambda_i}\, v_i, \quad \text{for } i = 1,\dots,N, \tag{5}$$

and the spatial mode

$$\phi_i(x,y) := \frac{1}{N\lambda_i}\sum_{k=1}^{N} a_i(t_k)g'(x,y,t_k), \quad \text{for } i = 1,\dots,N. \tag{6}$$

The temporal coefficient $a_i(t)$ (see Eq. (5)) reveals the dynamical behavior of the structure that is captured in the corresponding spatial mode $\phi_i(x,y)$, which provides spatial information. Further details can be found in Sirovich (1987); Sieber et al. (2016); Taira et al. (2017); Holmes et al. (2012).

2.2. Mode-coupling algorithm

Since the dynamics of periodic structures can be described by a pair of POD-modes, the mode-coupling algorithm proposed in Sieber et al. (2016) is used in addition. Related modes are identified by the spectral similarity of their temporal coefficients, which accounts for modes that are shifted by a quarter period. Such modes also show a similar amount of energy and appear pairwise in the POD spectrum, i.e. eigenvalues appear pairwise in the spectrum of R (see Eq. (4)), as mentioned in Oberleithner et al. (2014). The mode coupling is computed by an additional eigenvalue decomposition

$$Ac_i = \mu_i c_i \tag{7}$$

$$\text{with } A := \begin{bmatrix} a_1^2 & \cdots & a_N^2 \\ \vdots & \ddots & \vdots \\ a_1^N & \cdots & a_N^N \end{bmatrix}^T \cdot \left(\begin{bmatrix} a_1^1 & \cdots & a_N^1 \\ \vdots & \ddots & \vdots \\ a_1^{N-1} & \cdots & a_N^{N-1} \end{bmatrix}^T \right)^+ \in \mathbb{R}^{N\times N}, \tag{8}$$

where a_i^k denotes the kth entry of the ith temporal coefficient a_i and $(\cdot)^+$ denotes the Moore-Penrose pseudo inverse of the corresponding matrix. Note that this is a dynamic mode decomposition

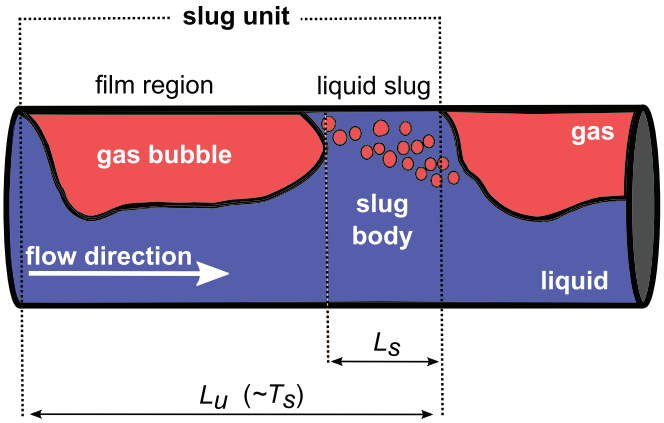

Fig. 1. Illustration of a slug unit in a longitudinal section of a pipe segment.

(Schmid, 2010; Tu, 2014) of the temporal coefficients. The similarity measure of the temporal coefficients a_i and a_j is given by

$$H_{i,j} := \mathrm{Im}\left(\sum_{k=1}^{N} c_k^i \bar{c}_k^j \,\mathrm{sgn}\left(\mathrm{Im}(\mu_k)\right)\right), \tag{9}$$

where $\bar{c}_k^j$ denotes the complex conjugate of c_k^j, Im the imaginary part and sgn the sign function. The corresponding matrix H is also called harmonic correlation matrix. The maxima of H correspond to the temporal coefficients with the highest spectral similarity, which allow an identification of the coupled modes. The dominant frequency $f_{i,j}$ of an identified mode pair (a_i, a_j) (equivalently denoted by (ϕ_i, ϕ_j)) is then derived from the corresponding eigenvalue μ_k (see Eq. (7)) by

$$f_{i,j} := \frac{\mathrm{Im}\left(\ln(\mu_k)\right)}{2\pi}. \tag{10}$$

To determine the combined energy content of the mode pair (a_i, a_j), the corresponding eigenvalues of the modal decomposition (see Eq. (4)) are summed as

$$E_{i,j} := \frac{\lambda_i + \lambda_j}{\sum_{k=1}^{N} \lambda_k}. \tag{11}$$

Note that for variables g with arbitrary units, such as phase volume fraction and RGB-intensity which are used in this paper, the term $E_{i,j}$ represents a mathematical energy distribution in terms of total variances or mean fluctuating intensities of the corresponding discrete time series in a_i and a_j (Sirovich, 1987; Wold et al., 1987). Thus, the largest eigenvalues reveal the POD-modes with the largest mean fluctuations. The term $E_{i,j}$ can only be identified with a physical energy if g has appropriate physical units, such as turbulent kinetic energy for a velocity vector field. For details, see Sieber et al. (2016).

3. Simulated slug flow

The simulation of a periodic air-water slug flow through a horizontal pipe with an inner diameter of $D = 0.054$m and a length of $L = 8$m, was adopted from Frank (2005). The considered slug flow consists only of periodically formed slugs, moving on top of the liquid layer. This attribute of the flow pattern simplifies the evaluation of the POD-modes and enables a basic validation of the characterization achieved by snapshot POD. The fluid properties and superficial velocities of this flow are given in Table 1.

For the computation, the pipe was discretized as an *O-grid* consisting of about 1.1 million nodes (45 nodes in radial, 104 nodes in angular, and 685 nodes in longitudinal direction). To generate a periodic formation of slugs in the pipe, a time-dependent sinusoidal

Table 1
Fluid properties and superficial velocities for numerical simulation.

Parameter	Air	Water
density in kg · m^{-3}	1.225	998.2
dyn. viscosity in Pa·s	$1.789 \cdot 10^{-5}$	$1.003 \cdot 10^{-3}$
superficial velocity in m · s^{-1}	1.0	1.0

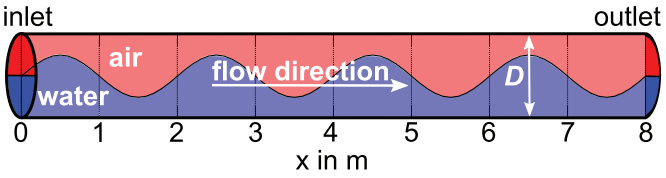

Fig. 2. Illustration of initial condition and geometry for the numerical simulation (not to scale)

Table 2
Spatial discretization schemes.

Variable	Method
Gradient	Green-Gauss node based
Pressure	Body force weighted
Momentum	Second order upwind
Volume fraction	Compressive
Turbulence parameters	First order upwind

displacement of the vertical position of the air-water interface is applied to this flow as introduced in Frank (2005). For this, the inlet is initialized with equally distributed phases in the inlet cross section, such that the lower half of the cross section is filled with water and the upper half is filled with air (see Fig. 2).

The initial condition is obtained from the vertical position of the interface $\tilde{y}_{int}$ by

$$\tilde{y}_{int}(x, t=0) = \frac{D}{4}\sin\left(2\pi\frac{4x}{L}\right) + \frac{D}{2}, \tag{12}$$

where t denotes the time and x the spatial component in flow direction (see Fig. 2). The time-dependent vertical position of the interface at the inlet is then given by

$$\tilde{y}_{int}(x=0, t) = \frac{D}{4}\sin\left(2\pi\frac{v\,4t}{L}\right) + \frac{D}{2}, \tag{13}$$

where $v = 2\mathrm{ms}^{-1}$ denotes the inlet gas or liquid velocity. This perturbation leads to a periodic slug formation in the pipe with a frequency of 1Hz (see Fig. 2). Furthermore, the walls of the pipe are treated as hydraulically smooth with no-slip boundary conditions applied for both phases. At the end of the pipe, a pressure outlet boundary condition is set.

The multiphase flow simulations were performed using the commercial CFD solver ANSYS FLUENT, version R18.2 (Fluent User's Guide, 2015). For this, an *unsteady Reynolds-averaged Navier-Stokes* (URANS) approach with the $k-\omega$-SST turbulence model was chosen (Menter, 1994). To model the gas-liquid interface the *volume of fluid* (VOF) method was applied within a mixture model (Hirt and Nichols, 1981). In addition, turbulence damping was included to model such flows with high velocity gradients at the interface (Egorov, 2004). The spatial discretization schemes are chosen as in Fiebach et al. (2016) and are stated in Table 2. For the time discretization, a bounded second order implicit scheme was applied. The Pressure-Implicit- with Splitting-of-Operator (PISO) algorithm together with an Algebraic-Multigrid (AMG) method is used for solving the discretized Reynolds-averaged Navier-Stokes equations.

In Fig. 3, a snapshot of the gas volume fraction field $\alpha_{air}(x, y, t_1)$ from a longitudinal section of the pipe is depicted. Here, the time-dependent interface displacement at the inlet is visible along

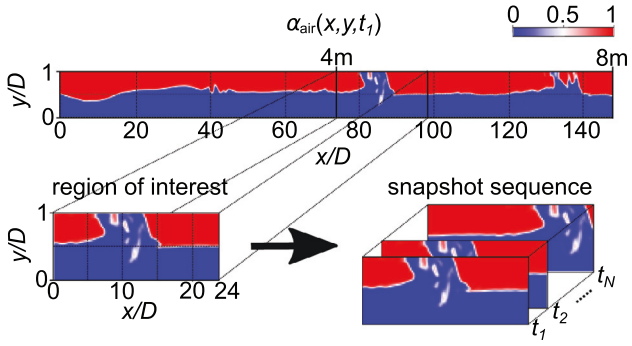

Fig. 3. Air volume fraction field α_{air} from the longitudinal section of the complete pipe, with the 24D long field of interest (not to scale) and illustration of the snapshot sequence.

Table 3
Fluid properties and superficial velocities for experiment.

Parameter	Nitrogen gas	Paraflex oil
density in kg · m^{-3}	11.4	829.32
dyn. viscosity in Pa·s	$1.8 \cdot 10^{-5}$	$16.07 \cdot 10^{-3}$
superficial velocity in m · s^{-1}	0.625	1.864

the upstream part of the pipe. Further downstream the water slugs are formed.

To ensure, that numerical effects from the initialization do not affect the flow field anymore and the simulated flow is well developed, the first seconds [0, T] of the simulated flow are discarded for the analysis, such that

$$T\frac{\bar{v}_{inlet}}{L_p} > 10, \tag{14}$$

with the averaged inlet velocity $\bar{v}_{inlet} = 2\text{ms}^{-1}$ and the length of the pipe $L_p = 8\text{m}$. Hence, before monitoring the flow, the time that the fluid of the initialization needed to left the pipe in average, has passed more than tenfold. Afterwards, the data are collected with a sample rate of 100Hz.

For the analysis of the simulated slug flow with snapshot POD, a snapshot sequence of gas volume fraction fields are collected from a longitudinal section of the pipe. For this, a 24D long pipe segment is considered, starting at $x/D \approx 74$ ($x = 4\text{m}$), where the liquid slugs are already formed (see Fig. 3). Furthermore, a time interval of 10s with 10 slugs is considered sufficient for a statistical characterization of this slug flow test case, since the slugs are formed periodically, with a similar propagation velocity, as well as similar length and shape due to the perturbation at the inlet.

4. Experimental slug flow

The experimental data of a horizontal gas-liquid slug flow is used to verify the characterization achieved by snapshot POD also for more complex types of slug flow. The experiment was performed by TÜV SÜD National Engineering Laboratory (NEL) as part of the project *Multiphase flow metrology in oil and gas production* (ENG, 2018). The experimental set-up is illustrated in Fig. 4. It consists of a straight horizontal pipe with an inner diameter of $D = 0.0972\text{m}$ and a length of approximately 100D, followed by a Perspex viewing section with a length of approximately 5D, where the slug flow was recorded from the side by a high-speed RGB-camera with a frame rate of 240fps. This section is followed by a complex measurement section with bends and vertical segments (ENG, 2018; Fiebach et al., 2016), but this part is of minor interest since the slugs in the horizontal pipe are investigated. The fluid properties and superficial velocities are listed in Table 3.

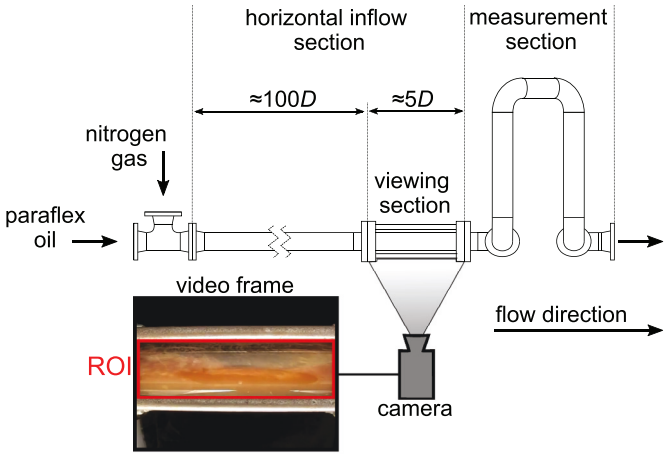

Fig. 4. Illustration of the experimental set-up with region of interest (ROI) for data extraction.

In the RGB-frames of the video recording, the oil appears to be reddish-brown and the black background is only visible for the transparent gas (see Fig. 4). Due to that, the red component of the RGB-frame is considered for the analysis with snapshot POD since it allows a clear distinction of the fluids. For the extraction of the snapshot sequence, a region of interest (ROI) is defined on the frames that includes only the visible area of the pipe segment (see Fig. 4). Since a statistical characterization of the slugs is sought, an interval of 60s with approximately 150 slugs is used for the analysis with snapshot POD.

4.1. Extension of the region of interest

For the spatial characterization of the slugs with snapshot POD, the size of the field should be sufficiently large, such that the averaged slug structure can be displayed entirely. However, for the considered experimental data, the observed averaged slug body length $\bar{L}_s \approx 6.3D$ is larger than the 4.2D long segment of the viewing section, visible in the video recordings. Because of this, an extension procedure based on cross correlation is applied to the video data.

The extension of the region of interest is done by embedding the frames into time-shifted frames from the same video, without a distortion of the slugs. Therefore, the averaged time is required that the slugging structures need to travel from inlet to outlet of the pipe segment in the frames. To determine this time, the normalized cross-correlation is used (Lewis, 2001). For this, pixel columns over time are extracted from the grayscale frames at the inlet and outlet of the viewing section, visible in the video (see Fig. 5a-c). These images are cross-correlated to obtain the temporal offset Δt in between the observed flow at inlet and outlet. This offset is given by the coordinates of the maximal cross-correlation coefficient. Here, the unique global maximum $\gamma_{max} = 0.84$ indicates a horizontal shift of 31 time steps from inlet to outlet. This time-shift is then used to identify the frames for the embedding. Furthermore, the pixel-wise mean absolute percentage error (MAPE) (Hyndman and Koehler, 2006) of the pixel columns over time at inlet and outlet, shifted by Δt, is given by 1.94%. In addition, the corresponding pixel-wise error in Fig. 5d indicates that the error is mostly located at the different reflection areas as well as the foamy areas in between the slugs. This is caused by different lighting conditions at the inlet and outlet. From this, it can be concluded that the variations in shape and translational velocity of the slugs are negligible over the distance of the 4.2D long pipe segment in the frame. These facts allow the region of interest to be extended by 4.2D in downstream and upstream direction, without distorting the slugs. Hence, the inlet of the pipe segment in the frame

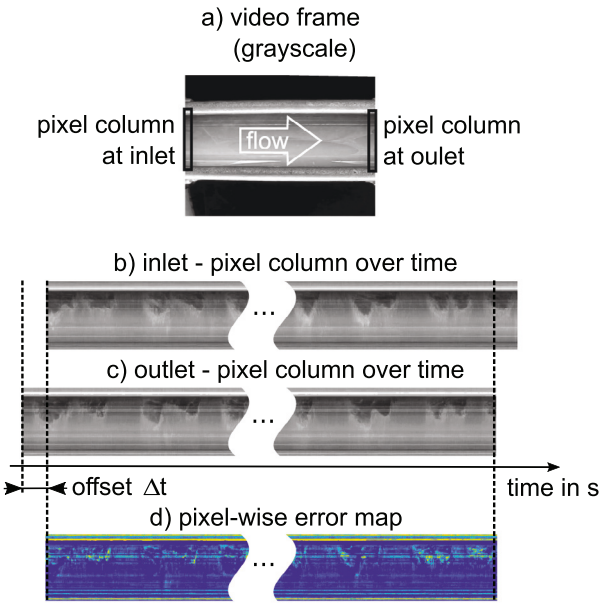

Fig. 5. Illustration of the cross-correlation procedure of the pixel column over time from grayscale frames (a) extracted at the inlet (b) of the field of view and the outlet (c), as well as the pixel-wise error map (d) of (b) and (c) shifted by Δt.

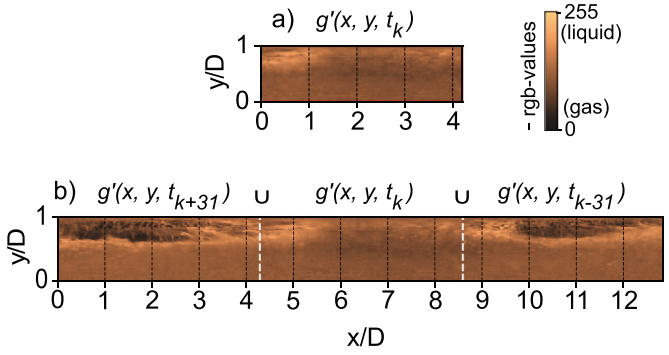

Fig. 6. Snapshot of the red component fluctuations $g'(x, y, t_k)$ at the time step $t_k \approx 3$s (a) and corresponding snapshot for the extended region of interest (b), consisting of the merged snapshots $g'(x, y, t_{k+31}) \cup g'(x, y, t_k) \cup g'(x, y, t_{k-31})$. Flow direction from left to right.

at t_k is then connected with the outlet of the pipe segment in the frame at t_{k+31}, to extent the region of interest by an additional segment length of $4.2D$ in upstream direction. With the same procedure, the region of interest is extended by $4.2D$ in downstream direction, using the frame at t_{k-31} (Fig. 6b). A similar procedure is often used for the visualization of a single slug, where consecutive frames need to be chosen and merged to display the slug, see ENG (2018); Wang et al. (2016). The proposed embedding is applied to all frames of the video, to generate a snapshot sequence with an approximately $12.6D$ long region of interest (see Fig. 6b), such that the averaged slug can be displayed entirely.

An averaged translational velocity of the slugs is also derived from the temporal offset Δt obtained from cross correlation. The calculated offset of 31 time steps correspond to $\Delta t \approx 0.13$s. Then a velocity of approximately 3.18ms^{-1} can be derived, with the distance of about 0.41m in between the inlet and the outlet of the visible segment of the viewing section. This velocity represents an averaged translational velocity of the large structures in the flow (Fig. 5b,c). Hence, it can be used to approximate the averaged translational slug velocity $\bar{v}_s$. This procedure is similar to the calculations of the slug velocity by cross correlation of the liquid holdup time series (Baba et al., 2018) except that it is based on flow images as in the calculations for optical velocimetry, such as PIV (Brossard et al., 2009). Thus, the calculated averaged translational slug velocity for the considered experiment is given by $\bar{v}_s = 3.18\text{ms}^{-1}$.

5. Results and discussion

5.1. Parameter for validation

For the validation of the snapshot POD results, the time series of the vertical position of the gas-liquid interface at a specific longitudinal position is required. This non-dimensional parameter represents the dynamics of the gas-liquid flow pattern, similar to the holdup parameter. It has a range of [0,1] with respect to the inner diameter of the pipe and is hereinafter also referred to as the *liquid level* over time at a certain position x, denoted by $h_L(t)$. For the considered gas volume fraction fields of the simulation data, the air-water interface can easily be identified in the longitudinal pipe sections by $\alpha_{air} = 0.5$. The vertical position of this interface is then collected over time at the desired position to obtain the liquid level over time. For a smooth representation of this parameter, a *Savitzky-Golay* filter with a window size of 21 sampling points and a polynomial degree of 3 is applied. This filter type is based on low-order polynomial regression and accounts also for small changes to represent the signal tendency more precisely, compared to standard type filters, such as moving average (Savitzky and Golay, 1964).

To extract this parameter from the high-speed video observations of the considered experiment for horizontal slug flow, the RGB color values of a vertical line through the horizontal pipe (pixel column) at a desired position are selected over time. Thus, an image is obtained, which represents a two dimensional projection of the slug flow from aside at one position over time (see Fig. 7a). The gas-liquid interface in this image was marked manually by the authors. Then the vertical position of the marked interface was extracted with an edge detection filter to obtain an approximation of the liquid level over time $h_L(t)$ (see Fig. 7b). The parameter $h_L(t)$ represents the dynamical behavior of the slug flow at a fixed position and is used to derive timescales for the slug structures.

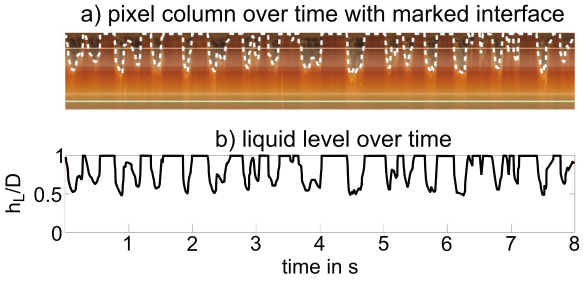

Fig. 7. Illustration of the procedure for liquid level extraction from high-speed video recordings of the experiments for horizontal slug flow, 8s of the flow extracted at the position $x/D = 2.2$ in the visible pipe segment.

5.2. Results for simulation data

In this section, a statistical characterization in space and time of the periodic air-water slug flow from a numerical simulation, described in Section 3, is presented. The characterization is derived from the most energetic mode pair (ϕ_1, ϕ_2) (see Fig. 8) of a snapshot POD analysis, and can clearly be verified since the considered

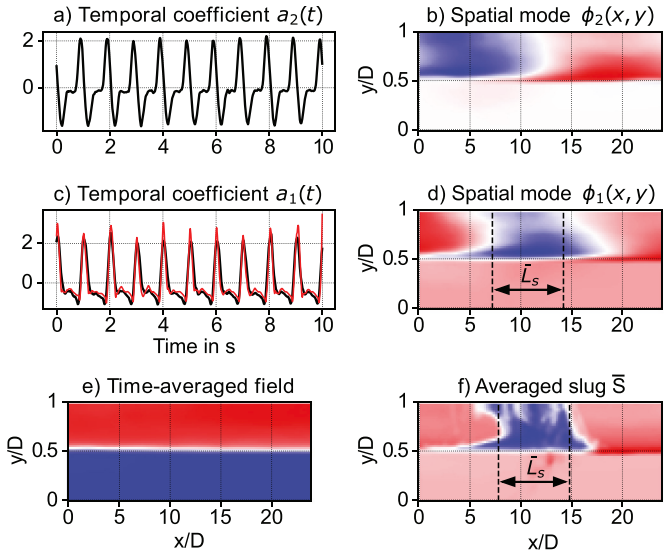

Fig. 8. Most energetic mode pair (ϕ_1, ϕ_2) with corresponding temporal coefficients $a_1(t)$, $a_2(t)$ (—) from snapshot POD in comparison with liquid level $h_L(t)$ (—) at $x/D = 11.3$, the averaged slug $\bar{S}$ and the time averaged air volume fraction field $\bar{\alpha}_{air}$, obtained from simulated data. The averaged slug body length $\bar{L}_s = 7\,D$ is indicated in *d*) and *f*). Note that a_1, a_2, h_L are depicted in standard score and the drawings are not to scale.

slug flow is periodic with an averaged slug frequency $\bar{f}_s = 1$Hz (see Eq. (1)) and similar slug structures. Furthermore, at the position, where the snapshot sequence was extracted, this flow only consists of slugs and the corresponding film regions. Due to that, the slugs are well recognizable and do not interfere with other structures, such as large amplitude waves.

In Fig. 8a-d, the most energetic mode pair with corresponding temporal coefficients is shown. The underlying coherent structure of this mode pair is identified with the slug structures, as proposed in Olbrich et al. (2019). In detail, this identification can be concluded from the following.

The temporal coefficients a_1, a_2 in standard score, i.e.:

$$z(a_i)(t) := \frac{a_i(t) - \bar{a}_i}{\sigma(a_i)}, \tag{15}$$

where $\bar{a}_i$ denotes the mean value and $\sigma(a_i)$ denotes the standard deviation of a_i (Larsen and Marx., 2012), coincide with the liquid level h_L in standard score, especially in width and periodicity of the peaks. Thus, the underlying coherent structure, described by (a_1, a_2), shows the same dynamical behavior as the slug structures in the flow, which are represented by the liquid level h_L. Note that, the standard score is considered for the comparison of the time series, because a_i and h_L have different ranges. Furthermore, the structures displayed in the spatial modes can be identified with the averaged slug (see Fig. 8f). Note that, the modes of a mode pair are shifted to each other. Hence, the focus for further analysis is on a_1 and ϕ_1, because for this, the structures are fully resolved within the considered viewing section.

The mean relative error δ of the variables h_L and a_1 in standard score is given by

$$\delta(z(h_L), z(a_1)) := \frac{100}{n} \frac{\Sigma_{j=1}^{n} |z(a_1)(t_j) - z(h_L)(t_j)|}{\max z(h_L) - \min z(h_L)} = 6.14\%. \tag{16}$$

Moreover, the averaged slug frequency $\bar{f}_s = 1$Hz obtained from h_L is equal to that, obtained from a_1. Note that, for the calculation of $\bar{f}_s$ and the corresponding time intervals in between the slug fronts T_{s_i} from the time series, a threshold of $z(a_1) = z(h_L) = 1$ was set. Such a threshold-procedure is often used to identify slugs in time series of the liquid holdup (Zhao et al., 2015). Another important aspect for the comparison of the time series a_i and h_L is the x-position in the pipe segment, where the liquid level is considered. For this, the correct position was found to be the streamwise position of the highest blue (liquid) intensity $x = 11.3\,D$ in the spatial mode ϕ_1, since the corresponding temporal coefficient a_1 represents also the dynamics of the gas and liquid distribution, shown in ϕ_1. Therefore, the liquid level time series was extracted at $x = 11.3\,D$ as described in Section 5.1. In conclusion, the dynamical behavior of the liquid level is represented sufficiently accurate by the temporal coefficient a_1. Due to that, a temporal characterization of the slug flow can be derived from a_1.

Table 4
Statistical characterization of simulated slug flow from most energetic mode pair.

Energy content $E_{1,2}$	49.7 %
Averaged slug frequency $\bar{f}_s$	1Hz
Averaged slug body length $\bar{L}_s$	7 D

Furthermore, the averaged slug $\bar{S}$ (Fig. 8f) and the spatial mode ϕ_1 (Fig. 8d) show a strong correlation with a maximal normalized cross correlation coefficient (Lewis, 2001) of $\max(\gamma(\bar{S}, \phi_1)) = 0.88$, without an offset in the coordinates of $\max(\gamma)$. Hence, the liquid structure displayed in ϕ_1 matches the averaged slug $\bar{S}$ and the averaged slug body length $\bar{L}_s = 7\,D$ can be derived from ϕ_1; Explanations of $\bar{S}$ later in the text. Note that, the normalized cross correlation coefficient is a reliable measure for feature tracking or template matching. It is independent of feature size and changes in image amplitude. Details can be found in Lewis (2001). In the analysis of this contribution, the MATLAB function `normxcorr2d` from the image processing toolbox is used to compute γ.

In addition to that, the energy content $E_{1,2} = 49.7\%$ (Eq. (11)) and the averaged dominant frequency $f_{1,2} = 1$Hz (Eq. (10)) of the coupled mode pair (ϕ_1, ϕ_2) is obtained from the snapshot POD with mode coupling. For this test case, $f_{1,2}$ coincides with $\bar{f}_s$ since the slug flow is periodic. However, for non-periodic slug flow with additional waves, $f_{1,2}$ and $\bar{f}_s$ may differ, since $f_{1,2}$ represents a mean dominant frequency of the corresponding time series given by the temporal coefficients (a_1, a_2) and not the inverse mean time in between consecutive slugs, such as $\bar{f}_s$.

Altogether, a statistical characterization for the considered slug flow in space and time can be derived from the most energetic mode pair (ϕ_1, ϕ_2) and is summarized in Table 4.

For the comparison of the liquid structure shown in ϕ_1 with the averaged slug from the flow, the latter needs to be at the same position as the structure shown in ϕ_1. Thereby, the influence of the variation in slug shape at different streamwise positions, caused by, e.g.: slug growth, can be avoided. Therefore, the averaged slug $\bar{S}$ (see Fig. 8f) is extracted from the considered snapshot sequence of the air-volume fraction field, where the times of the slugs at the desired position in the pipe segment are determined from the times of the local maxima of the temporal coefficient. For better comparability, the time-averaged field $\bar{\alpha}_{air}$ (see Fig. 8e) is subtracted from the selected snapshots.

5.3. Influence of the field length

In this section, the influence of the field length on the temporal coefficient as well as on the spatial mode is presented. Here, the primary focus is on the accuracy of the temporal coefficient and the liquid level, as well as the spatial mode and the time-averaged slug. To determine the accuracy, the error δ and the maximal normalized cross correlation coefficient γ_{max} is considered, as described in Section 5.2. Generally, a clear negative trend in accuracy was noted with increasing length of the region of interest. The detailed results are presented in the following.

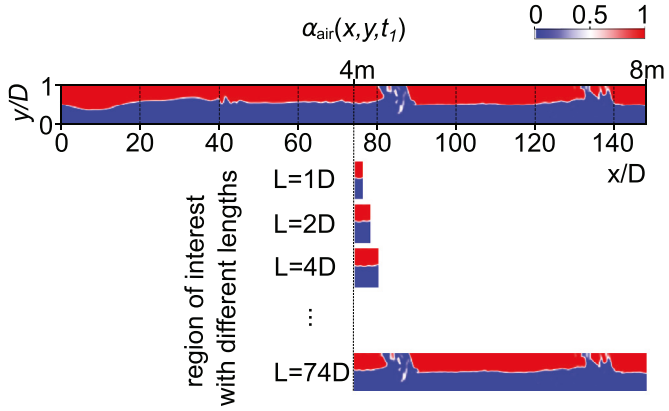

Fig. 9. Illustration of the region of interest with different lengths. Drawings are not to scale.

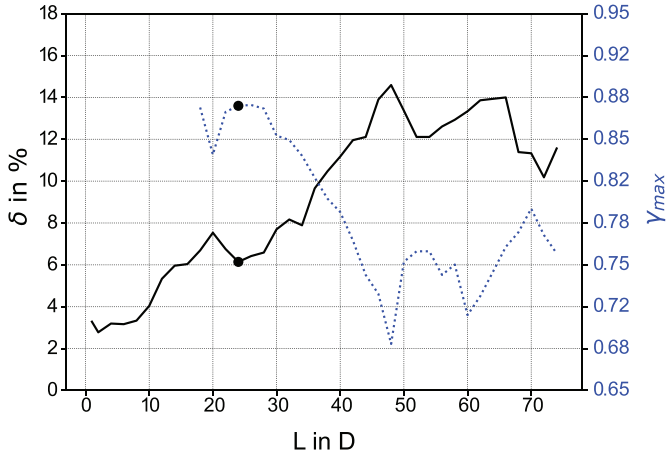

Fig. 10. Mean relative error $\delta(z(h_L), z(a))$ (——) of the temporal coefficient a and the liquid level h_L in standard score (left axis), as well as the maximal normalized cross correlation coefficient $\gamma_{max} = \max(\gamma(\bar{S}, \phi))$ (·····) of the averaged slug $\bar{S}$ and the spatial mode ϕ (right axis) for increasing lengths L of the region of interest are depicted. The marker (•) indicates the values at $L = 24\,D$, which was used for the analysis in Section 5.2.

For this investigation, the snapshot POD was performed on snapshot sequences, extracted from regions of interest with 38 different lengths $L = 1\,D, 2\,D, 4\,D, \ldots, 74\,D$, starting at $x/D \approx 74$ ($x =$ 4m) of the horizontal pipe (see Fig. 9). In the further, only the mode of the most energetic mode pair is considered, where the corresponding temporal coefficient matches the liquid level over time at the position of maximal blue intensity in the spatial mode, such as a_1 in Section 5.2. This mode is hereinafter denoted as ϕ and a respectively.

The mean relative error $\delta(z(h_L), z(a))$ is growing for increasing length L (see Fig. 10). One reason for this trend is the calculation of the temporal coefficient a from the temporal correlation matrix R of the spatially averaged gas volume fraction fields (see Eq. (4)). Due to the not normalized spatial averaging of the snapshots in the POD algorithm, small structures, such as single slugs, are underrepresented in larger regions of interest. Furthermore, spatial averages of neighboring snapshots, where the same structure is at a slightly different position, become more similar for larger regions of interest. This leads to a broader temporal correlation, and results in a smoother and wider temporal coefficient with lower amplitude and lower energy ratio (see Fig. 11a,d,g,j). Hence, the representation of the slugs in the temporal coefficient becomes more imprecise for increasing L, relative to the detailed liquid level h_L. For $L > 48\,D$, when a second slug start to be visible in the region of interest simultaneously, the error δ decreases (see Fig. 10).

Note that the energy content of the mode pairs that correspond to the given modes in Fig. 11 decrease for increasing ROI length: $E_{1D} = 73,7\%$, $E_{20D} = 54,9\%$, $E_{40D} = 40.4\%$ with a slight increase of energy, when the second slug starts to be visible simultaneously $E_{60D} = 41.7\%$.

To obtain meaningful results of the measure γ in the comparison of the spatial mode ϕ with the averaged slug $\bar{S}$, only the regions of interest with the lengths $L \geq 18\,D$ are considered, since the slugs need to be fully visible in the region of interest, from the beginning of the slug front to the end of the slug rear.

The normalized cross correlation coefficient γ_{max} shows a clear average decay with increasing length L (see Fig. 10) and has an inverse behavior of δ. This can be explained by the fact, that the spatial mode ϕ is calculated as the weighted average of the fluctuations of the snapshots, where the weights are given by the values of the temporal coefficient and the corresponding eigenvalue (see Eq. (6)). Thus, the error δ in the temporal representation of the slugs in a propagates in their spatial representation in ϕ. In detail, the broader and more inaccurate the peaks in the temporal coefficient, the more weight is put on snapshots with slugs in slightly shifted position for the calculation of ϕ. Thus, the averaged slug visible in ϕ appear to be blurred for increasing L (see Fig. 11e-k).

In addition to that, slugs accelerate and change shape as they move downstream the pipe. For larger L, this phenomenon is also having more influence on the averaging processes in the computation of a and ϕ and can cause negative effects on the accuracy.

Altogether, it can be concluded, that for a meaningful approximation of the dynamics and shape of the slugs in a and ϕ respectively, the length L of the region of interest should be sufficiently small. For this example, $L \leq 30\,D$ was found to give reasonable results, since $\delta \leq 8\%$ and $\gamma_{max} \geq 0.85$. Note that $L = 24\,D$ was chosen for the analysis in Section 5.2 because δ attains a local minimum at $\delta = 6.14\%$ and $\gamma_{max} = 0.8766$ is sufficiently high (see Fig. 10).

5.4. Results for experimental data

In this section, a statistical characterization in space and time of the nitrogen gas - paraflex oil slug flow described in Section 4 is presented. Following the same procedure as in the periodic slug flow in Section 5.2, the characterization of the experimental slug flow is also derived from the most energetic mode pair (ϕ_1, ϕ_2) of a snapshot POD analysis. First, the results for the original region of interest are presented, which focus on the temporal characterization of the slugs, since the short region of interest does not resolve the averaged slug. After this, the results for the extended region of interest are presented, which allow also a spatial characterization of the slugs.

5.4.1. Results for original region of interest

In Fig. 12a-d, the most energetic mode pair with corresponding temporal coefficients is shown. This mode pair is similar to the mode pair of the periodic slug flow from the numerical simulation (Fig. 8a-d), and the underlying coherent structure of this mode pair is also identified with the slugs. Note that the ordering of the single modes in the mode pair is different compared to the simulated slug flow test case.

The temporal coefficient a_2 coincides with the liquid level over time $h_L(t)$ at $x/D = 2.2$ (Fig. 12c) with a mean error $\delta(z(h_L), z(a_2)) = 10.3\%$. The corresponding spatial mode ϕ_2 (Fig. 12d) indicates, that the pipe segment is completely filled with the brown paraflex oil, without a recognizable slug tail and slug rear. The same holds for the averaged slug $\bar{S}$ (Fig. 12f), since the averaged slug is longer than the region of interest. Due to that,

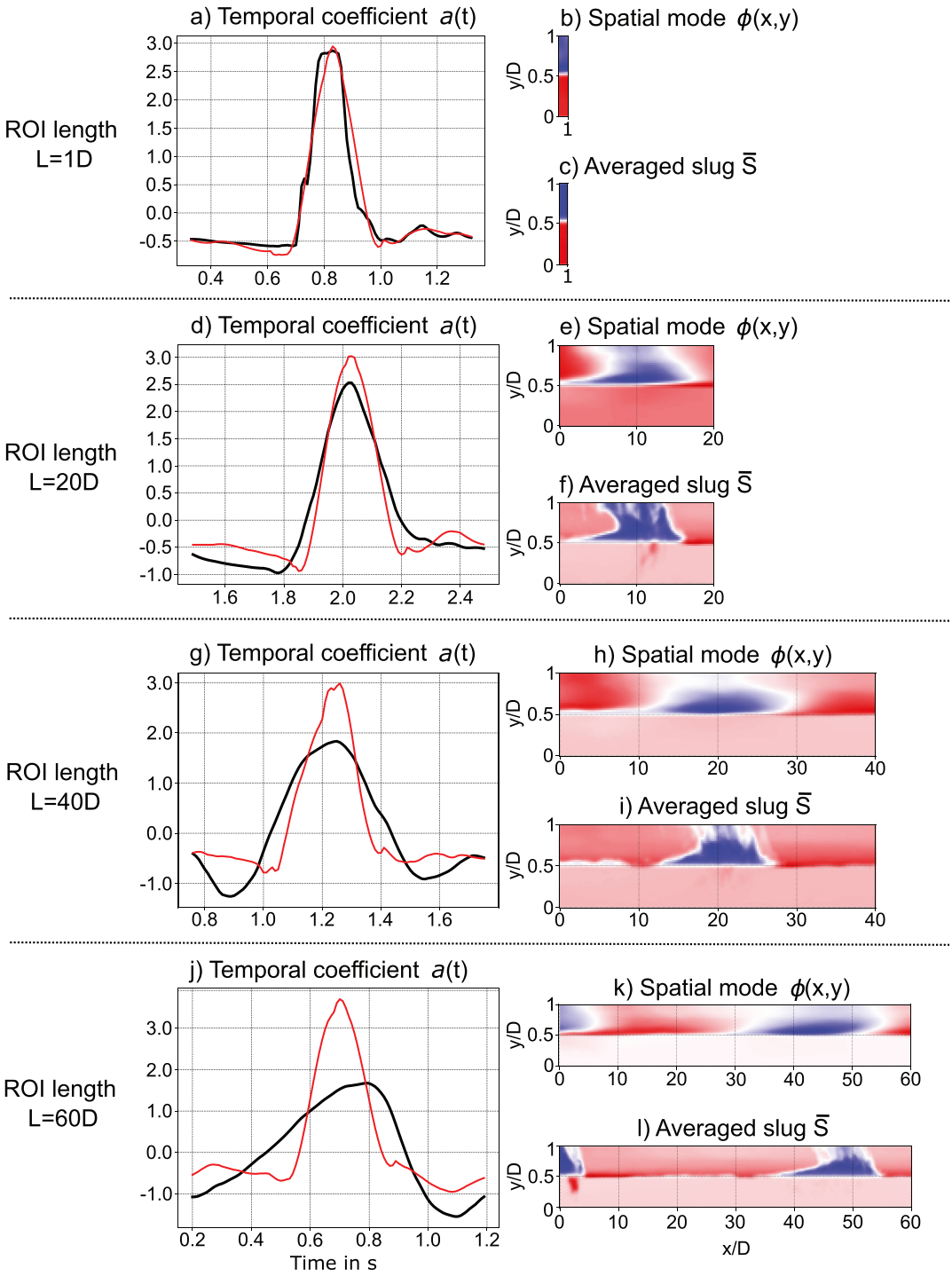

Fig. 11. Illustration of one peak of the temporal coefficient a (—), that represents the second slug in the flow data, in comparison with liquid level h_L in standard score (—) extracted at the position of maximal blue intensity in the corresponding spatial mode (a,d,g,j), as well as the corresponding spatial mode (b,e,h,k) and the averaged slug (c,f,i,l) for the different lengths $L \in \{1\,D, 20\,D, 40\,D, 60\,D\}$. Energy content of corresponding mode pairs: $E_{1D} = 73,3\%$, $E_{20D} = 54,9\%$, $E_{40D} = 40.4\%$, $E_{60D} = 41.7\%$. Drawings are not to scale.

the averaged slug body length $\bar{L_s}$ cannot be derived from the spatial mode. Nevertheless, a temporal characterization of the slug flow can be derived from the temporal coefficient, as mentioned in Viggiano et al. (2018); Olbrich et al. (2019). The temporal coefficient a_2 represents the dynamics of the large structures in the flow, such as slugs. Hence, an average slug frequency can be derived from it. Here, a threshold of $z(a_2) = z(h_L) = 0.5$ was set to detect the slug fronts. That corresponds to an absolute value in the liquid level of $h_L = 0.93$. This allows to distinguish between large amplitude waves and slugs, but not separate slugs by larger entrained bubbles, floating in the upper part of the slug. Then, the averaged slug frequency is given by $\bar{f_s} = 2.53$Hz. Using the same threshold for the temporal coefficient in standard score $z(a_2)$ the calculations of the averaged slug frequency results in $\bar{f_s} = 2.57$Hz. In addition to that, the mean frequency of the mode pair is given by $f_{1,2} = 2.26$Hz. The difference in between $f_{1,2}$ and $\bar{f_s}$ can be explained by the fact that, $f_{1,2}$ represents a mean dominant frequency of the corresponding time series given by the temporal coefficients

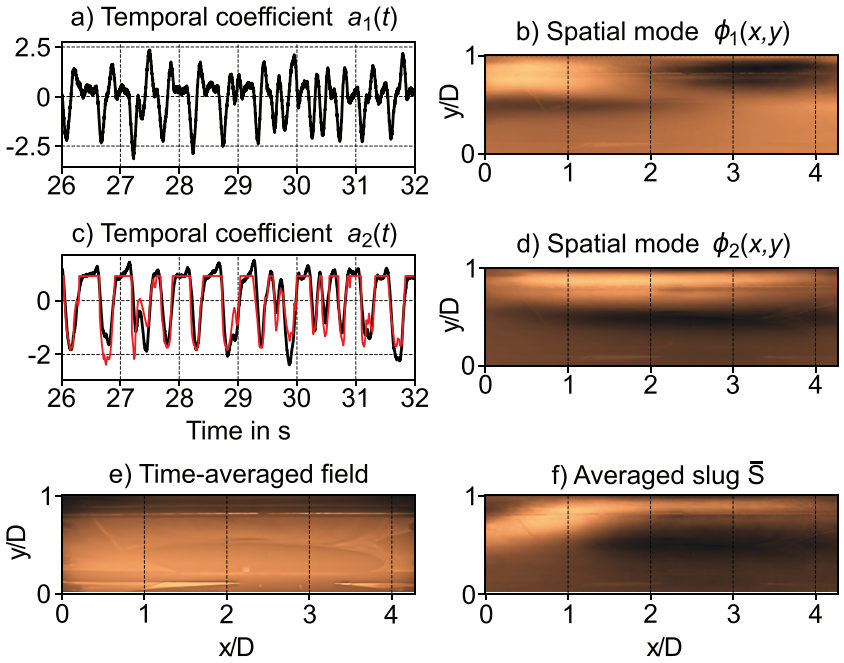

Fig. 12. Most energetic mode pair (ϕ_1, ϕ_2) with corresponding temporal coefficients $a_1(t)$, $a_2(t)$ (—) from snapshot POD in comparison with liquid level $h_L(t)$ (—) at $x/D = 2.2$, the averaged slug $\bar{S}$ and the time averaged air volume fraction field $\bar{\alpha}_{air}$, obtained from experimental data. The averaged slug is too long for the viewing section, as visible in *d*) and *f*). Note that a_1, a_2, h_L are depicted in standard score and the drawings are not to scale.

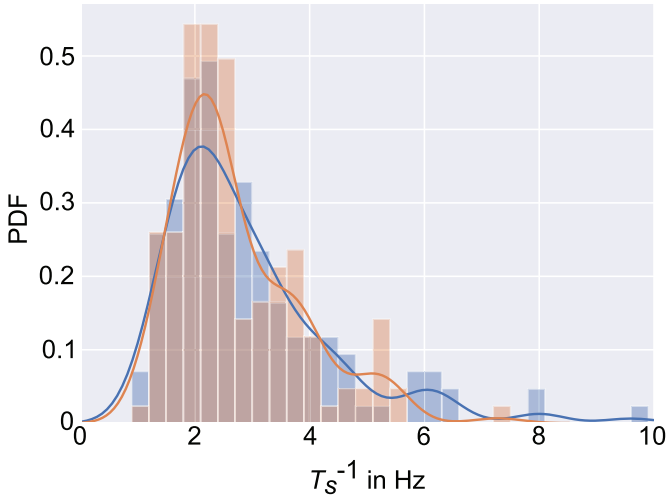

Fig. 13. The probability density function (PDF) of slug frequency $f_s = T_s^{-1}$ obtained from the liquid level over time h_L at $x/D = 2.2$ (—) and the temporal coefficient a_2 (—) with corresponding histogram for h_L (■) and a_2 (■).

Table 5
Statistical parameters for the slug frequencies f_s from the liquid level h_L and the temporal coefficient a_2.

parameter	h_L	a_2
mean $\bar{f}_s$	2.53Hz	2.57Hz
median $\tilde{f}_s$	2.58Hz	2.47Hz
standard deviation $\sigma(f_s)$	5.30Hz	5.50Hz

(a_1, a_2), whereas $\bar{f}_s$ denotes the inverse mean time in between consecutive slugs, as mentioned already in Section 5.2. Since this slug flow is non-periodic, a distribution of the slug frequency can provide a more detailed characterization of the slug flow, compared to a single mean value and allows further validation of the temporal characterization by snapshot POD.

In Fig. 13, the probability density function as well as the corresponding normalized histogram of the inverse time in between consecutive slugs T_s^{-1}, obtained from the liquid level h_L as well as the temporal coefficient a_2, are given. Here, a threshold of $z(a_2) = z(h_L) = 0.5$ and a uniform bin size of 0.3Hz was used. The probability density functions and corresponding histograms calculated from the temporal coefficient a_2 and liquid level h_L provide similar statistical parameters as shown in Table 5. The small discrepancy is primarily caused by the overestimation of large waves in the temporal coefficient.

In addition to the temporal characterization from the temporal coefficient, a spatial characterization of the averaged slug can be derived from the time series under knowledge of the averaged translational slug velocity $\bar{v}_s$, see e.g. Viggiano et al. (2018); Baba et al. (2018). In this case, $\bar{v}_s = 3.18\text{ms}^{-1}$, see Section 4.1. Using the same threshold $z(a_2) = z(h_L) = 0.5$, as before, the time intervals from the slug front to rear are detected and averaged. Then, the averaged slug body length $\bar{L}_s$ can be approximated by multiplication of the averaged interval with $\bar{v}_s$. This leads to $\bar{L}_s = 5.94D$ for the temporal coefficient $a_2(t)$ and $\bar{L}_s = 6.3D$ for the liquid level $h_L(t)$.

5.4.2. Results for extended region of interest

To show that the snapshot POD can also provide a spatial characterization of an experimental slug flow in the spatial modes, the snapshot POD is performed on the frame embedded snapshot sequence with the extended region of interest (see Section 4.1). The results are presented in the further. This extended region of interest with about $12.6D$ in length is long enough to display the averaged slug with an averaged slug body length of $\bar{L}_s = 6.3D$ entirely. In Fig. 14, the most energetic mode pair is depicted. Note that the discontinuities, visible in Fig. 14b,d,e, arise from the differences in illuminance and lighting conditions in between inlet and outlet of the viewing section in the video recordings. Here, the inlet-region is more illuminated, than the outlet-region. This leads to the discontinuities at the position $x/D = 4.2$ and $x/D = 8.4$, where outlet

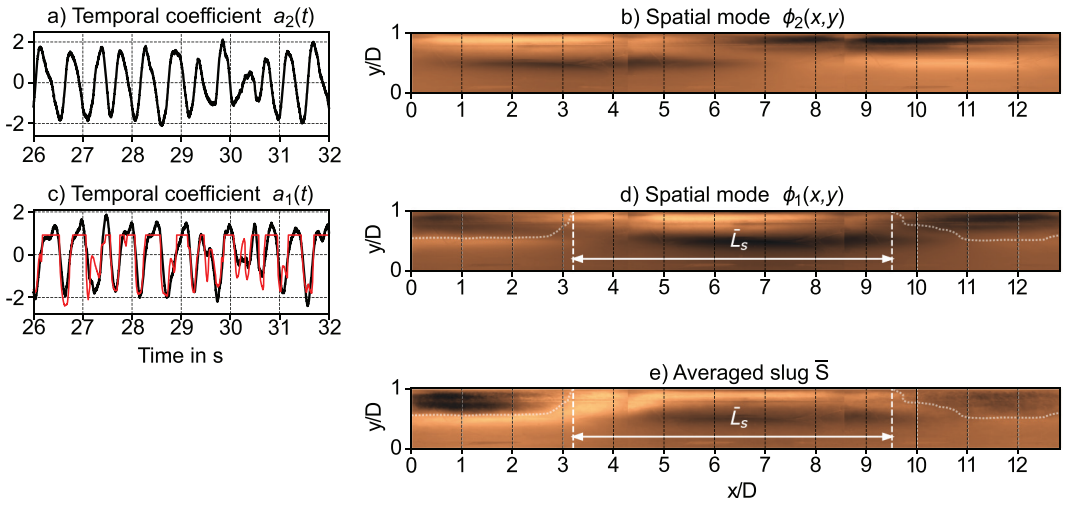

Fig. 14. Most energetic mode pair (ϕ_1, ϕ_2) with corresponding temporal coefficients $a_1(t)$, $a_2(t)$ (——) from snapshot POD in comparison with liquid level $h_L(t)$ (——) at $x/D = 6.6$ and the averaged slug $\bar{S}$ (see e), obtained from experimental data with extended region of interest. The gas liquid interface from the averaged slug $\bar{S}$ is highlighted (.....) in *d*) and *e*). Furthermore, the averaged slug body length $\bar{L}_s = 6.3D$ is indicated in *d*) and *e*). Note that a_1, a_2, h_L are depicted in standard score and the drawings are not to scale.

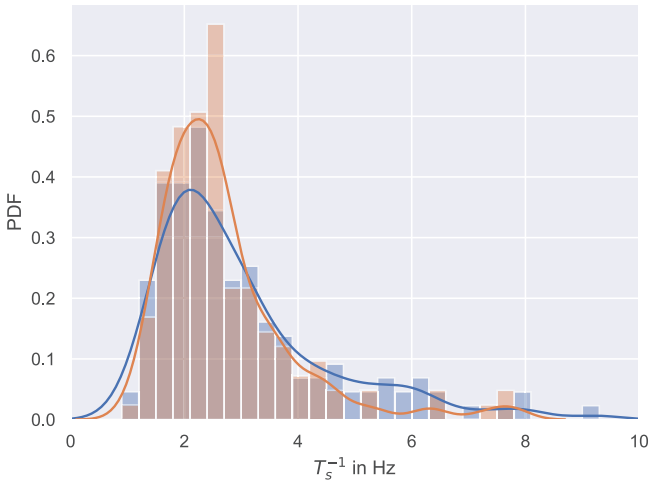

Fig. 15. The probability density function (PDF) of slug frequency $f_s = T_s^{-1}$ obtained from the liquid level over time h_L at $x/D = 6.6$ (——) and the temporal coefficient a_1 (——) for the extended region of interest with corresponding histogram for h_L (■) and a_1 (■).

Table 6
Statistical parameters for the slug frequencies f_s from the liquid level h_L and the temporal coefficient a_1 for the extended region of interest.

parameter	h_L	a_1
Mean $\bar{f}_s$	2.53Hz	2.72Hz
Median $\tilde{f}_s$	2.61Hz	2.58Hz
Standard deviation $\sigma(f_s)$	5.53Hz	5.03Hz

Table 7
Statistical characterization of the slug flow experiment from the most energetic mode pair.

Energy content $E_{1,2}$	25.2 %
Averaged slug frequency $\bar{f}_s$	2.72Hz
Averaged slug body length $\bar{L}_s$	6.3 D

and inlet were merged for the embedding. As discussed before, the underlying coherent structure of this mode pair is identified with the slug structures in the flow.

Following the same analysis of the temporal coefficient as before in Section 5.4.1, the mean relative error of a_1 and h_L in standard score is given by $\delta(z(h_L), z(a_1)) = 12.1\%$, which is 1.8% larger then the corresponding error for the results of the original region of interest. This is in line with the observed trend in Fig. 10, where the error increases with increasing length of the region of interest and the time series become smoother with broader peaks of lower amplitude. Due to that, the threshold for the slug frequency calculations was adjusted to a lower value of $z(a_1) = 0.34$, to match best the averaged slug frequency, obtained by the liquid level h_L with a threshold of $z(h_L) = 0.5$. The probability density function as well as the statistical parameters for the calculations of the slug frequencies are shown in Fig. 15 and Table 6, respectively.

As can be seen in Fig. 15, the PDF and the corresponding histogram obtained from a_1 follow the main trend of those, obtain from the liquid level h_L. Furthermore a_1 and h_L provide similar statistical parameters of the slug frequency, as shown in Table 6.

However, the difference of the PDF's for the liquid level and the temporal coefficient is larger, compared to the original region of interest (Fig. 13), due to the larger difference of the liquid level and the temporal coefficient. Note that, the values obtained from h_L are slightly different compared to Section 12, because h_L was extracted at a different x-position in the pipe segment, due to the larger region of interest. Here, it can be concluded, that the temporal coefficient a_1 represents the main temporal features of the slugs in this experiment.

Furthermore, the spatial mode ϕ_1 is representing the averaged slug $\bar{S}$, as shown in Fig. 14d,e. For reasons of clarity, the gas-liquid interface of $\bar{S}$ is marked in Fig. 14e and superimposed on the spatial mode ϕ_1 in Fig. 14d. Here, the averaged slug with an averaged slug body length of $\bar{L}_s \approx 6.3D$ is recognizable in the spatial mode ϕ_1 (see Fig. 14d).

Finally, the results of the analysis for the snapshot sequence with the extended region of interest is given in Table 7, since the

parameters can be derived from the snapshot POD results without any further information.

6. Conclusion

A procedure for the statistical characterization of horizontal slug flow based on the dominant mode pair from snapshot POD was introduced in this paper. Furthermore, the achieved characterization was validated in detail by comparison to information extracted from data on the liquid level. For this, a periodic slug flow from a numerical simulation as well as a non-periodic experimental slug flow were considered. It was shown that the temporal coefficients of the corresponding mode pair represent the dynamics of the gas-liquid interface and that the corresponding spatial modes exhibit a dominant structure, which was identified with the averaged slug. Consequently, parameters for the characterization of the slugs in time, such as averaged slug frequency and the corresponding probability density function, can be derived from one of the two temporal coefficients of the dominant mode pair. In addition to that, the averaged slug body length can be obtained from the corresponding spatial mode if the region of interest is large enough to resolve the averaged slug. Here, the snapshot POD provides this information not only for the high quality phase volume fraction fields from a numerical simulation, but also for RGB-values of a noise-affected experimental video recording. Furthermore, the influence of the length of the region of interest on the accuracy of the achieved characterization was investigated under usage of the simulation data. In this regard, a clear negative trend in accuracy for increasing length was noted. Consequently, the region of interest should have the necessary length to resolve the averaged slug entirely, but should remain sufficiently short to avoid larger errors in the parameters for a characterization in space and time. If only a characterization in time is sought, the region of interest should be chosen as short as possible. Altogether, snapshot POD provides a reliable statistical characterization in time and space for the considered horizontal slug flows. Prospectively, the snapshot POD can be used as a tool for comparing data from a numerical simulation to measurements from a corresponding experiment.

Declaration of Competing Interest

The authors declare that they have no known competing financial interests or personal relationships that could have appeared to influence the work reported in this paper.

CRediT authorship contribution statement

Marc Olbrich: Conceptualization, Methodology, Investigation, Software, Validation, Formal analysis, Visualization, Writing - original draft. **Markus Bär:** Conceptualization, Validation, Supervision, Writing - review & editing. **Kilian Oberleithner:** Conceptualization, Validation, Supervision, Writing - review & editing. **Sonja Schmelter:** Conceptualization, Methodology, Investigation, Software, Validation, Supervision, Writing - review & editing.

Acknowledgements

This work was supported through the Joint Research Project *Multiphase flow reference metrology* (16ENG07). This project has received funding from the EMPIR programme co-financed by the Participating States and from the European Union's Horizon 2020 research and innovation programme.

The authors would like to thank Terri Leonard and Marc MacDonald from TÜV SÜD National Engineering Laboratory (NEL), who provided the experimental video observations, as well as Sebastian Heidenreich, Nando Farchmin, and Vasco Worlitzer from PTB for the useful discussions.

References

Al-Kayiem, H.H., Mohmmed, A.O., Al-Hashimy, Z.I., Time, R.W., 2017. Statistical assessment of experimental observation on the slug body length and slug translational velocity in a horizontal pipe. Int. J. Heat Mass Transf. 105, 252–260.

Al-Safran, E., 2009. Investigation and prediction of slug frequency in gas/liquid horizontal pipe flow. J. Petrol.Sci. Eng. 69 (1), 143–155.

Baba, Y.D., Aliyu, A.M., Archibong, A.E., Abdulkadir, M., Lao, L., Yeung, H., 2018. Slug length for high viscosity oil-gas flow in horizontal pipes: Experiments and prediction. J. Petrol.Sci. Eng. 165, 397–411.

Brossard, C., Monnier, J., BARRICAU, P., Vandernoot, F., Le Sant, Y., Champagnat, F., Le Besnerais, G., 2009. Principles and applications of particle image velocimetry. AerospaceLab (1) p.1–11.

Dukler, A.E., Fabre, J., 1994. Gas-liquid slug flow. Multiph. Sci. Technol. 8 (1–4), 355–469.

Egorov, Y., 2004. Validation of CFD Codes with PTS-Relevant Test Cases. Technical Report. EVOL-ECORA-D07.

Fiebach, A., Schmeyer, E., Knotek, S., Schmelter, S., 2016. Numerical simulation of multiphase flow in a vertically mounted venturi flow meter. In: The 17th International Flow Measurement Conference (FLOMEKO 2016), Hilton Hotel, Sydney, Australia. http://metrology.asn.au/flomeko2016/papers/57cfbc44b9d2b-flomeko_paper_af_es_sk_ss_rev.pdf

Final Publishable JRP Report and associated Annex A - Multiphase Flow Metrology in Oil and Gas Production (ENG58), 2018. Technical Report. EURAMET.

Fluent User's Guide, 2015. 16.0. Fluent Inc.

Frank, T., 2005. Numerical simulation of slug flow regime for an air-water two-phase flow in horizontal pipes. In: The 11th International Topical Meeting on Nuclear Reactor Thermal-Hydraulics (NURETH-11), Popes' Palace Conference Center, Avignon, France. http://www.drthfrank.de/publications/2005/Frank_slug_flow_NURETH-11_2005.pdf

Hanratty, T.J., 2013. Physics of Gas-Liquid Flows. Cambridge University Press.

Hirt, C., Nichols, B., 1981. Volume of fluid (vof) method for the dynamics of free boundaries. J. Comput. Phys. 39 (1), 201–225.

Holmes, P., Lumley, J.L., Berkooz, G., Rowley, C.W., 2012. Turbulence, Coherent Structures, Dynamical Systems and Symmetry, 2 Cambridge University Press.

Hyndman, R.J., Koehler, A.B., 2006. Another look at measures of forecast accuracy. Int. J. Forecast. 22 (4), 679–688.

Larsen, R.J., Marx., M.L., 2012. Introduction to Mathematical Statistics and Its Applications, 5th Edition, 5. Prentice Hall.

Lewis, J., 2001. Fast normalized cross-correlation. Ind. Light Magic 10.

Lu, M., 2015. Experimental and Computational study of Two-Phase Slug flow. Imperial College London Ph.D. thesis.

Lumley, J.L., 1967. The structure of inhomogeneous turbulent flows. In: Yaglom, A.M., Tatarski, V.I. (Eds.), Atmospheric Turbulence and Radio Wave Propagation, pp. 166–178. Moskow: Nauka, 1967

Menter, F.R., 1994. Two-equation eddy-viscosity turbulence models for engineering applications. AIAA J. 32 (8), 1598–1605.

Munir, S., Siddiqui, M.I., Heikal, M., Abdul Aziz, A.R., de Sercey, G., 2015. Identification of dominant structures and their flow dynamics in the turbulent two-phase flow using pod technique. J. Mech. Sci. Technol. 29 (11), 4701–4710.

Oberleithner, K., Rukes, L., Soria, J., 2014. Mean flow stability analysis of oscillating jet experiments. J. Fluid Mech. 757, 1–32.

Olbrich, M., Schmeyer, E., Baer, M., Sieber, M., Oberleithner, K., Schmelter, S., 2019. Identification of coherent structures in horizontal slug flow. In: The 18th International Flow Measurement Conference (FLOMEKO 2019), LNEC, Lisbon, Portugal. http://flomeko2019.lnec.pt/flomeko2019_proceedings.pdf

Polansky, J., Wang, M., 2017. Proper orthogonal decomposition as a technique for identifying two-phase flow pattern based on electrical impedance tomography. Flow Measur. Instrum. 53, 126–132.

Polansky, J., Wang, M., 2018. Vertical annular flow pattern characterisation using proper orthogonal decomposition of electrical impedance tomography. Flow Measur. Instrum. 62, 281–296.

Savitzky, A., Golay, M.J.E., 1964. Smoothing and differentiation of data by simplified least squares procedures.. Anal. Chem. 36 (8), 1627–1639.

Schmid, P.J., 2010. Dynamic mode decomposition of numerical and experimental data. J. Fluid Mech. 656, 5–28. doi:10.1017/S0022112010001217.

Sieber, M., Paschereit, C.O., Oberleithner, K., 2016. Spectral proper orthogonal decomposition. J. Fluid Mech. 792, 798–828.

Sieber, M., Paschereit, O., Oberleithner, K., 2017. Advanced identification of coherent structures in swirl-stabilized combustors. J. Eng. Gas Turbines Power.

Sirovich, L., 1987. Turbulence and the dynamics of coherent structures. part i: Coherent structures. Quart. Appl. Math. 45, 561–571.

Taira, K., Brunton, S.L., Dawson, S.T.M., Rowley, C.W., Colonius, T., McKeon, B.J., Schmidt, O.T., Gordeyev, S., Theofilis, V., Ukeiley, L.S., 2017. Modal analysis of fluid flows: An overview. AIAA J. 55 (12), 4013–4041.

Taitel, Y., Dukler, A., 1977. A model for slug frequency during gas-liquid flow in horizontal and near horizontal pipes. Int. J. Multiph. Flow 3 (6), 585–596.

Tu, J.H., 2014. On dynamic mode decomposition: Theory and applications. Journal of Computational Dynamics 1, 391. doi:10.3934/jcd.2014.1.391. 2158-2491_2014_2_391

Viggiano, B., Skjæraasen, O., Schümann, H., Tutkun, M., Cal, R.B., 2018. Characterization of flow dynamics and reduced-order description of experimental two-phase pipe flow. Int. J. Multiph. Flow 105, 91–101.

Wang, Q., Polansky, J., Karki, B., Wang, M., Wei, K., Qiu, C., Kenbar, A., Millington, D., 2016. Experimental tomographic methods for analysing flow dynamics of gas-oil-water flows in horizontal pipeline. J. Hydrodyn. Ser. B 28 (6), 1018–1021.

Wold, S., Esbensen, K., Geladi, P., 1987. Principal component analysis. Chemometrics and Intelligent Laboratory Systems 2 (1), 37–52. doi:10.1016/0169-7439(87)80084-9. Proceedings of the Multivariate Statistical Workshop for Geologists and Geochemists

Zhao, Y., Lao, L., Yeung, H., 2015. Investigation and prediction of slug flow characteristics in highly viscous liquid and gas flows in horizontal pipes. Chem. Eng. Res. Des. 102, 124–137. doi:10.1016/j.cherd.2015.06.002.

2.3 Publication III

Comparing temporal characteristics of slug flow from tomography measurements and video observations

In the course of the previous investigations, an approximation of the liquid level time series as well as time scales of slug flow have been derived from video recordings. This temporal quantification of slug flow needs to be validated. In that regard, the temporal quantification of horizontal slug flow from highspeed video recordings is evaluated in this publication, where reliable parameters from an conventional tomography measurement technique are used as a reference (research objective 2).

For these investigations, the liquid level time series extracted from video recordings and the derived time scales of the slugs are compared to liquid volume fraction measurements of an electrical capacitance tomography (ECT) measurement system for two different horizontal oil-gas slug flow experiments. In a first step, the comparability of the time series from the video recordings and the cross-sectional tomography measurements is discussed. In this context, an approximation of the liquid level time series is constructed from the volumetric tomography measurements and a correction of the refractive effects from the transparent pipe wall in the video recordings is developed to achieve a comparability of the parameters from the two different measurement techniques. In a second step, the liquid level time series extracted from video observations are qualitatively compared with the time series from the tomography measurements. The same is done with the temporal slug characteristics.

Altogether, in this publication is shown that the characterizing time scales of slug flow from video recordings are in good agreement with the ones from the tomography measurement data. However, the liquid level time series from the video observations are systematically overestimated, compared to the tomography measurement data.

Measurement: Sensors 18 (2021) 100222

Contents lists available at ScienceDirect

Measurement: Sensors

journal homepage: www.sciencedirect.com/journal/measurement-sensors

Comparing temporal characteristics of slug flow from tomography measurements and video observations

ARTICLE INFO

Keywords
Slug flow
Interface dynamics
Tomography
Video observation

ABSTRACT

In industrial operations, the slug flow pattern can lead to serious problems, that are mostly caused by the liquid slugs of the flow. Hence, a detailed description of the slug flow pattern is of special interest. In this context, the temporal flow characteristics that are derived from high-speed video observations of the flow, are compared to tomography measurements. For this, the liquid level time series as well as the temporal slug characteristics of two different slug flow experiments are considered. It is shown that the liquid level time series from the video observations are systematically overestimated, but the slug dynamics are in good agreement.

1. Introduction

The slug flow pattern is a common gas-liquid flow regime in multiphase transportation pipelines, and can cause severe problems, such as large pressure fluctuations and vibrations [1,4]. These problems are primarily caused by the liquid slugs of the flow [5]. Thus, an accurate description of these slugs can contribute to the solution of such problems.

In this context, we have investigated different methods for a statistical characterization [6,7] as well as numerical modelling of horizontal slug flow [8,9] in previous works. For the validation of these methods and models, the vertical position of the gas liquid interface at a fixed position in flow direction was extracted from video recordings of the slug flow experiments, for details see [7]. In these video recordings the slug flow is observed from the side. The extracted time series is a non-dimensional parameter that represents the dynamics of the gas-liquid flow pattern, similar to the holdup parameter. It has a range of [0,1] with respect to the inner diameter of the pipe and is referred to as the *liquid level over time*.

In this contribution, the reliability of the liquid level time series extracted from video recordings is evaluated. For this purpose, it is compared with liquid volume fraction measurements of an electrical capacitance tomography (ECT) measurement system for two different horizontal oil-gas slug flow experiments. The focus of this investigation lies not only on a comparison of the time series from the ECT and the video system, but also on a comparison of the temporal characterizations of the liquid slugs, that can be derived from the time series.

2. Methods

In this chapter, the experimental setup, the considered horizontal slug flows, the tomography system, the video recordings and the procedure of extracting the time series are introduced.

2.1. Experimental set-up

The experiments were performed by TÜV SÜD National Engineering Laboratory (NEL) and DNV [4].

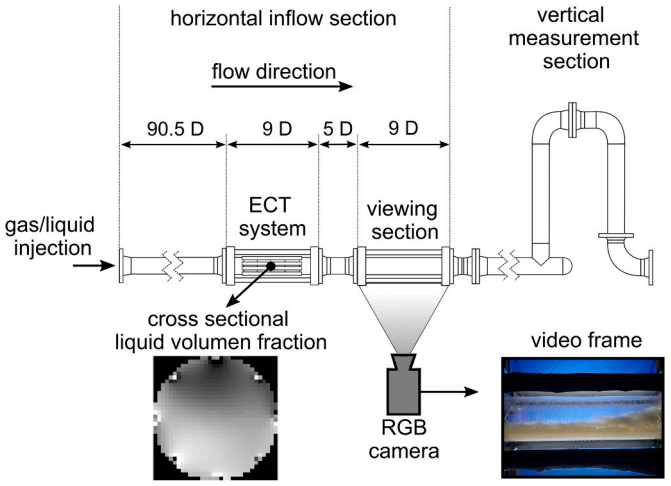

Fig. 1. Illustration of the experimental setup (drawing not to scale).

https://doi.org/10.1016/j.measen.2021.100222

Available online 22 September 2021

Table 1
Fluid properties and superficial velocities.

Slug flow exp.	Oil density in kg/m^3	Gas density in kg/m^3	Superficial gas vel. in m/s	Superficial liquid vel. in m/s
NR. 1 *(NEL)*	816.80 (*Paraflex HT9*)	10.79 (*Nitrogen*)	2.39	2.39
NR 2. *(DNV)*	823.44 (*Exxsol D120*)	10.44 (*Nitrogen*)	2.40	2.40

The experimental set-up is illustrated in Fig. 1. It consists of a straight horizontal pipe with an inner diameter of $D = 66.64$ mm and a length of 90.5 D, followed by an ECT measurement system and a transparent Perspex viewing section. This horizontal inflow section is followed by a complex measurement section with bends and vertical segments [4]. However, for our investigations, the latter section is of minor interest. The ECT-system is an *Atout APL-C-900 research system* and provides a snapshot sequence of cross-sectional liquid volume fraction measurements embedded in a rectangular grid with a spatial resolution of 32x32 px and a samplerate of 350 Hz, for details of the ECT system see [3]. At the transparent viewing section, the flow is recorded from the side by an RGB-camera with a spatial resolution of 1920 x1080 px and a framerate of 100 fps for the experiment at NEL and a framerate of 240 fps for the experiment at DNV. The two experiments show different types of slug flow. The fluid properties and superficial velocities of the considered slug flows are listed in Table 1.

2.2. Time series from the ECT system

The ECT-system provides spatially and temporally resolved data sets of the considered slug flows. These data sets consist of liquid volume fraction fields in the pipe cross section, which are measured over time with a constant sample rate of 350 Hz. From these measurements, two time series are derived. The first ones are the time series of the cross-sectionally averaged liquid volume fraction, denoted by $\alpha_L^{tomo}(t)$. The second ones are the time series of the vertical position of the gas-liquid interface, extracted from the vertical centreline of the cross-sectional measurement, denoted by $h_L^{tomo}(t)$. This is illustrated in Fig. 2. The interface in the stacked centreline image (see Fig. 2 on the right) is detected by calculating for every time t, the median of the vertical position in the centreline column, where $0.4 < \alpha_L < 0.5$ holds. The stacked centreline image (see Fig. 2 on the right) was found to represent best the side view of the flow, captured in the videos. Hence, $h_L^{tomo}(t)$ is a reasonable parameter for a comparison with the liquid level time series from the videos. Please note that under this construction of h_L^{tomo}, it does not follow from $h_L^{tomo} = 1$, that $\alpha_L^{tomo} = 1$.

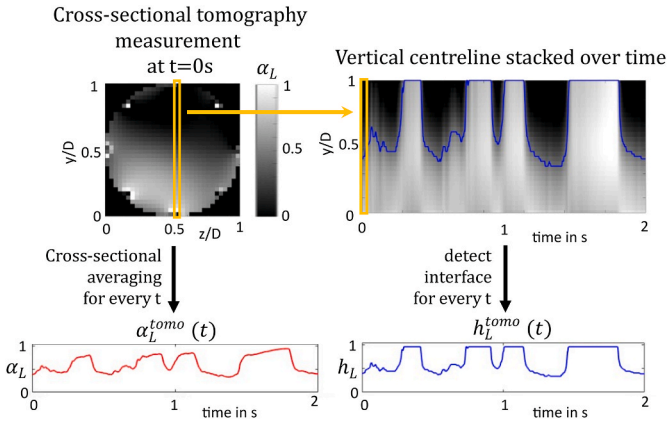

Fig. 2. Illustration of time series extraction of tomography data for Slug flow 2.

2.3. Time series from video recordings

The RGB-camera provides a snapshot sequence of the flow, recorded from the side, that represents a two-dimensional projection of the three-dimensional flow. To extract time series from this data set, a vertical pixel column through the pipe at a fixed x-position is stacked over time, similar to the vertical centreline image of the tomography data (see Fig. 2). Then, the interface is marked by hand to get a liquid level time series representation from the video recordings, denoted as $h_L^{video}(t)$, see [7,9]. The refractive effects of the transparent Perspex pipe wall are corrected, to achieve a better comparability with the measured time series from the ECT-system. For this correction as well as the extraction of the pixel column, the height of the projected inner diameter onto the outer pipe wall h_{max} is needed (see Fig. 3a). Since this height is not

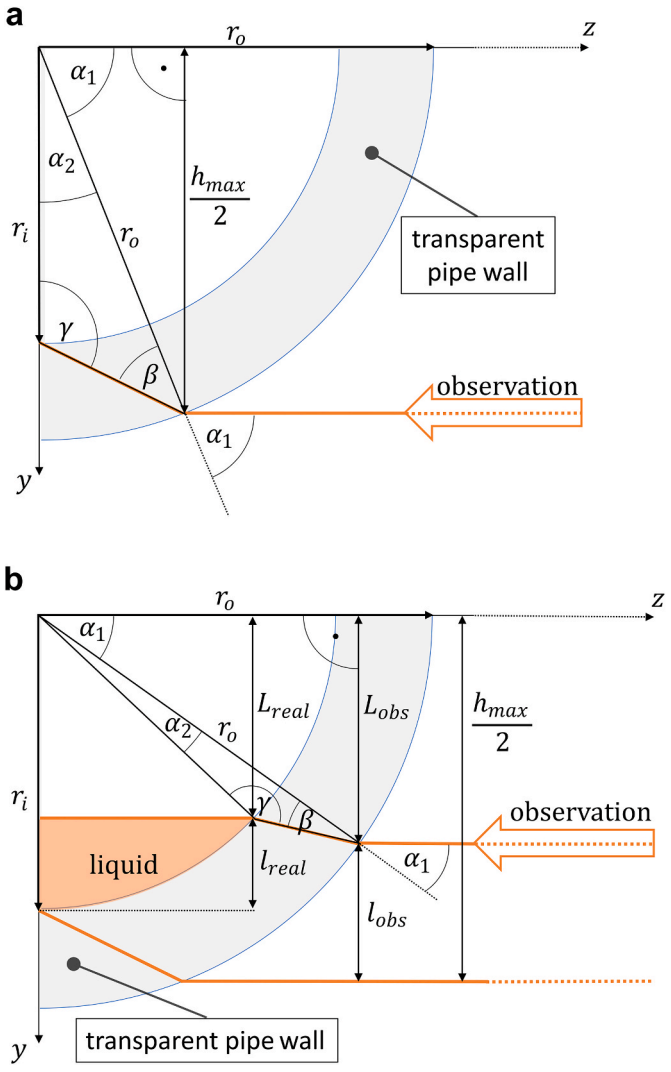

Fig. 3. Calculation of the projected inner diameter h_{max} onto the outer pipe wall (**a**), and correction of the refractive effects of the transparent pipe wall (**b**), illustrated for the fourth quadrant of the pipe cross section.

clearly assignable in the video frames, it is calculated by finding $\frac{h_{max}}{2} \in [r_i, r_o]$ with

$$\alpha_1 = \arcsin\left(\frac{h_{max}}{r_o}\right) \text{ and } \beta = \arcsin\left(\frac{n_{air}}{n_{perspex}}\sin(\alpha_1)\right), \text{ such that}$$

$$r_i = \frac{r_o}{\sin(\gamma)}\ \sin(\beta), \tag{1}$$

where the inner radius of the pipe is given by $r_i = 33.32\,mm$, the outer radius of the pipe is given by $r_o = 50\,mm$. Here, the angle of incidence α and the angles $\gamma = \pi - \alpha_2 - \beta$, $\alpha_2 = \frac{\pi}{2} - \alpha_1$ are calculated with trigonometric functions, see Fig. 3. The angle of refraction β is given by the law of refraction [2], where the indices of refraction are given as $n_{air} = 1.0$ and $n_{perspex} = 1.49$. This results in $h_{max} = 44.5299\,mm$. In a similar procedure as in (1), the refractive effects of the transparent pipe wall for the observed liquid level $l_{obs} \in [0, 1]$ with respect to h_{max} can be corrected, to get the correct liquid level $l_{real} \in [0, 1]$ with respect to the inner diameter D, see Fig. 3b. Here l_{real} is given as

$$l_{real} = \begin{cases} \dfrac{|r_i - L_{real}|}{D},\ if\ l_{obs} \le 0.5\ , \\ 1 - \dfrac{|r_i - L_{real}|}{D},\ else, \end{cases} \tag{2}$$

where $L_{real} = \sin(\alpha_1 + \alpha_2)r_i$, $L_{obs} = h_{max}(0.5 - l_{obs})$, the angle of incidence $\alpha_1 = \arcsin\left(\frac{L}{r_o}\right)$, the angles $\alpha_2 = \pi - \gamma - \beta$ and $\gamma = \pi - \arcsin\left(\frac{r_o}{r_i}\sin(\beta)\right)$ are calculated by means of trigonometric functions. Furthermore, the angle of refraction β is derived from the law of refraction, as given in (1). Please note that this correction was established under the assumption, that the ray of light for the observation is in parallel to the z-axis of the pipe cross-section.

3. Results

For a quantitative comparison, the time series from the ECT-system and the video recording are shifted in time to show the same time interval of the flow using the maximum of the cross-correlation function. This leads to a common total time of the time series for the analysis of 117 s for Slug flow 1 and 100 s for Slug flow 2.

For the comparison of the time series from the ECT-system and the video recording, their statistical parameters, as well as temporal slug characteristics are considered. In particular, we determine the slug unit time t_u and the slug body time t_b, where the slug unit time t_u is the time interval between two consecutive slug fronts and the slug body time t_b is the time interval from slug front to slug rear. To detect slug fronts and slug rears in the time series, a thresholding technique is applied, for details see [9]. These thresholds are set for all time series individually and are given in Table 2. In Fig. 4, the time series α_L^{tomo}, h_L^{tomo} and h_L^{video} of Slug flow 1 and 2 are shown for a time of 5 s with the corresponding threshold lines. As it can be seen in Fig. 1, Slug flow 1 has short slugs and several waves with larger amplitudes. For this flow, entrained bubbles in the slugs and waves as well as layers of foam in between these structures were observed in the videos. In contrast to this, Slug flow 2 consists of larger slugs and less waves. Please note, due to the two different types of slug flow, the level of agreement for the evaluation methods may vary.

In Fig. 5, the boxplots with the statistical parameters, such as mean,

Table 2
Threshold values for slug detection.

Time series	Slug flow 1	Slug flow 2
α_L^{tomo}	0.7	0.65
h_L^{tomo}	0.75	0.8
h_L^{video}	0.9	0.9

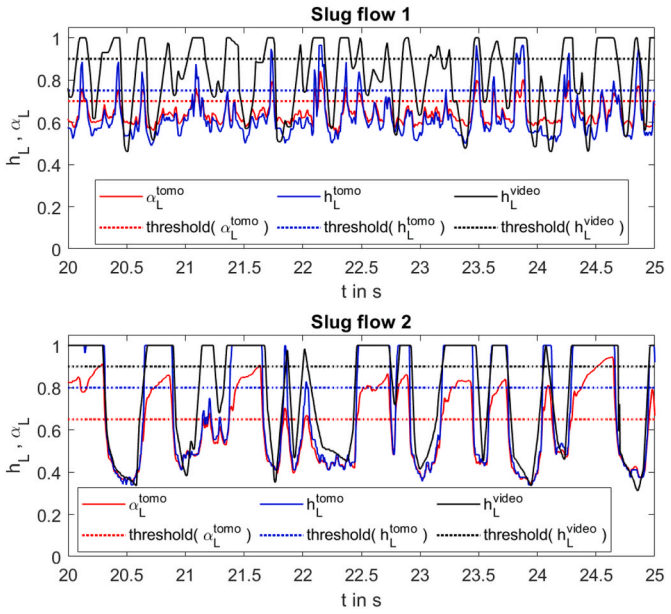

Fig. 4. The time series of Slug flow 1 and 2 from tomography α_L^{tomo}, h_L^{tomo} and video recordings h_L^{video} shown for 5s with their corresponding threshold lines.

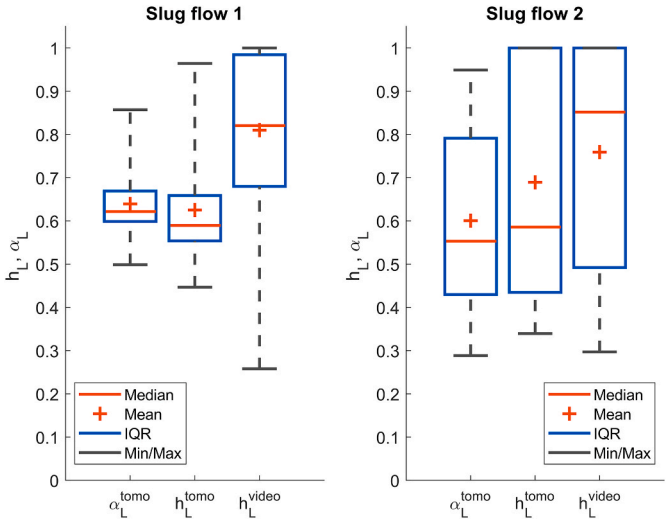

Fig. 5. Boxplots of the time series of slug flow 1 and 2 from tomography α_L^{tomo}, h_L^{tomo} and video recordings h_L^{video}.

median, interquartile range (IQR), minimum and maximum values are given for the time series α_L^{tomo}, h_L^{tomo} and h_L^{video} of Slug flow 1 and 2. Here, a systematic difference between the time series can be seen. The liquid volume fraction α_L^{tomo} is a volumetric parameter, derived from the complete pipe cross-section by averaging and therefore accounts for changes in all three dimensions of the flow, especially along the z-axis. This averaging leads to low values and a small range (interval in between Minimum and Maximum) compared to the other time series. In contrast to this, the liquid level h_L^{video} is derived from a two-dimensional projection of the three-dimensional flow, which does not account for changes in the z-direction, since they are not visible in the videos. The liquid level time series from tomography h_L^{tomo} is a reasonable approximation of h_L^{video} and therefore h_L^{video} shows a better agreement with h_L^{tomo}, compared to α_L^{tomo}. However, h_L^{tomo} is based on liquid volume fraction data in the centreline of the pipe cross-section, and therefore also dependent on the distribution of the phases along the z-axis.

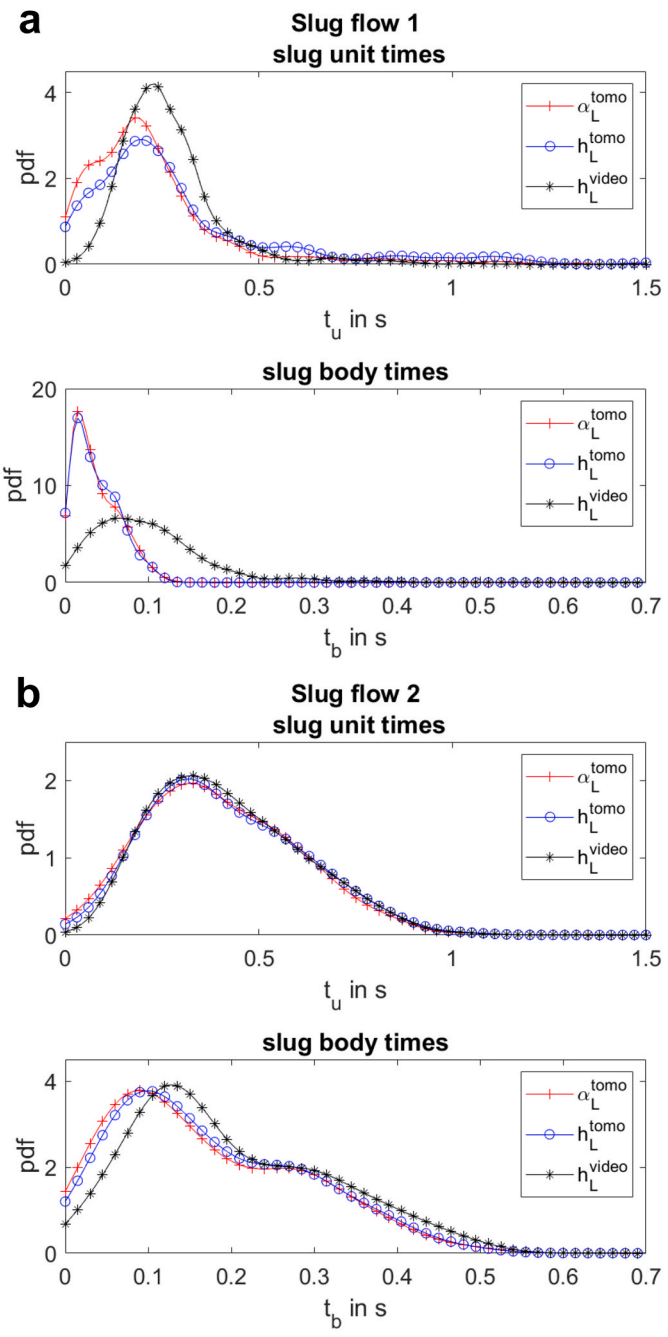

Fig. 6. Probability density functions (pdf) of t_u and t_b derived from α_L^{tomo}, h_L^{tomo} and h_L^{video} for slug flow 1 and 2.

Apart from the changes of the flow in between the location of the ECT and camera-system along the pipe, foamy layers and entrained gas bubbles are also leading to a discrepancy of the time series from tomography and video recordings. This is caused by the foamy layers, that are assigned to the liquid phase, when the interface is extracted from the video recordings, because the classification of foam into liquid or gas is not obvious for camera-based flow observations from the side. The same holds for entrained gas bubbles in the waves or slugs. In contrast to this, the tomography system only measures the liquid phase, leading to lower values for α_L^{tomo} and h_L^{tomo}, compared to h_L^{video}. In Fig. 6a and b, the probability density functions of the slug unit times t_u and slug body times t_b derived from all three time series are presented for Slug flow 1 and 2.

In contrast to the larger differences of the statistical parameters of the time series themself, the slug characteristics t_u and t_b show better agreement. This is especially true for the slug unit times t_u that are directly related to the slug frequency, see [7,9]. The slug body times t_b derived from h_L^{video} are slightly overestimated with respect to α_L^{tomo} and h_L^{tomo} because the time series themself show the same behaviour.

4. Conclusions

In this paper, the liquid level time series extracted from RGB-video recordings of two horizontal slug flows were compared to liquid level and liquid volume fraction time series derived from a tomography measurement system. The liquid level time series from the video recordings show a systematic overestimation with respect to the time series from the tomography system. In contrast to this, the derived temporal characteristics of the liquid slugs show good agreement, especially the slug unit times, which are the inverse of the slug frequencies. From this, it can be concluded, that the temporal characterization of horizontal slug flow derived from the liquid level parameter from RGB-video recordings give reasonable results.

Acknowledgments

This work was supported through the Joint Research Project *Multiphase flow reference metrology* (16ENG07). This project has received funding from the EMPIR programme co-financed by the Participating States and from the European Union's Horizon 2020 research and innovation programme.

References

[1] H.H. Al-Kayiem, A.O. Mohmmed, Z.I. Al-Hashimy, R.W. Time, Statistical assessment of experimental observation on the slug body length and slug translational velocity in a horizontal pipe, Int. J. Heat Mass Tran. 105 (2017) 252–260.
[2] M. Born, E. Wolf, Principles of Optics: Electromagnetic Theory of Propagation, Interference and Diffraction of Light, Cambridge University Press, 1999.
[3] R. Drury, A. Hunt, J. Brusey, Identification of horizontal slug flow structures for application in selective cross-correlation metering, Flow Meas. Instrum. 66 (2019) 141–149.
[4] Final Publishable Report - Multiphase Flow Reference Metrology (16ENG07), Technical Report, EURAMET, 2020.
[5] T.J. Hanratty, Physics of Gas-Liquid Flows, Cambridge University Press, 2013.
[6] M. Olbrich, E. Schmeyer, M. Bär, M. Sieber, K. Oberleithner, S. Schmelter, Identification of coherent structures in horizontal slug flow, Flow Meas. Instrum. 76 (2020).
[7] M. Olbrich, M. Bär, K. Oberleithner, S. Schmelter, Statistical characterization of horizontal slug flow using snapshot proper orthogonal decomposition, Int. J. Multiphas. Flow 134 (2021).
[8] S. Schmelter, M. Olbrich, E. Schmeyer, M. Bär, Numerical simulation, validation, and analysis of two-phase slug flow in large horizontal pipes, Flow Meas. Instrum. 73 (2020).
[9] S. Schmelter, S. Knotek, M. Olbrich, A. Fiebach, M. Bär, On the influence of inlet perturbations on slug dynamics in horizontal multiphase flow - a computational study, Metrologia 58 (2021).

Marc Olbrich*
Physikalisch-Technische Bundesanstalt (PTB), Abbestr. 2-12, 10587 Berlin, Germany
Institute of Fluid Dynamics and Technical Acoustics, Technische Universität Berlin, Müller-Breslau-Straße 8, 10623 Berlin, Germany

Andrew Hunt
Atout Process Ltd, 26-28 West Street, Bridport, DT6 5QP, United Kingdom

Terri Leonard
TÜV SÜD National Engineering Laboratory, East Kilbride, Glasgow, G75 0QF, United Kingdom

Dennis S. van Putten
DNV, Energieweg 17, 9743 AN, Groningen, the Netherlands

Markus Bär
Physikalisch-Technische Bundesanstalt (PTB), Abbestr. 2-12, 10587 Berlin, Germany

Kilian Oberleithner
Institute of Fluid Dynamics and Technical Acoustics, Technische Universität Berlin, Müller-Breslau-Straβe 8, 10623 Berlin, Germany

Sonja Schmelter
Physikalisch-Technische Bundesanstalt (PTB), Abbestr. 2-12, 10587 Berlin, Germany

* Corresponding author.
E-mail address: marc.olbrich@ptb.de (M. Olbrich).

2.4 Publication IV

Deep learning based liquid level extraction from video observations of gas–liquid flows

A fast and reliable non-intrusive method for the approximation of the liquid level time series from video data can serve as a useful tool in industrial and academic operations, where a temporal quantification of separated and intermittent flow patterns, such as stratified wavy or slug flow, is needed. In that regard, the accurate and efficient extraction of the liquid level time series from video observations of separated and intermittent flow patterns with a novel deep learning based image processing technique is investigated in this publication (research objective 3).

For this, a deep-learning based image processing method is presented, that consists of a certain type of a deep convolutional neural network, called U-net, and several pre- and post-processing steps. The U-net was trained and tested with video data from horizontal slug flows for the task of segmenting liquid and gas regions in the video frame data. For the training procedure and the quantification of accuracy and error values in the validation process, hand-labelled segmentation maps were used as reference. The consistency of these hand-labelled data and the predictions from the U-net was shown in an inter-observer reliability test. For further evaluations of this model, additional independent video data were used, which show different fluids, settings, and flow pattern.

Altogether, it is shown in this publication that the presented method accurately extracts the liquid level time series from the considered video data. It can handle different types of data, even unseen data sets. Furthermore, it can overcome various noise effects, which are generally included in such image or video data. Once, the net is successfully trained, it predicts highly accurate segmentation maps in very short time, such this the liquid level time series can be extracted accurately and efficiently from the raw video data.

International Journal of Multiphase Flow 157 (2022) 104247

Contents lists available at ScienceDirect

International Journal of Multiphase Flow

journal homepage: www.elsevier.com/locate/ijmulflow

Deep learning based liquid level extraction from video observations of gas–liquid flows

Marc Olbrich [a,b,*], Leili Riazy [c], Tobias Kretz [a], Terri Leonard [d], Dennis S. van Putten [e], Markus Bär [a], Kilian Oberleithner [b], Sonja Schmelter [a]

[a] Physikalisch-Technische Bundesanstalt (PTB), Abbestr. 2-12, 10587 Berlin, Germany
[b] Institute of Fluid Dynamics and Technical Acoustics, Technische Universität Berlin, Müller-Breslau-Straße 8, 10623 Berlin, Germany
[c] Cardiovascular Magnetic Resonance, Experimental and Clinical Research Center, Charité Campus Buch, Lindenberger Weg 80, 13125 Berlin, Germany
[d] TÜV SÜD National Engineering Laboratory (NEL), East Kilbride, Glasgow G75 0QF, United Kingdom
[e] DNV, Energieweg 17, 9743 AN Groningen, The Netherlands

ARTICLE INFO

Dataset link: https://gitlab1.ptb.de/mfm2/liquid_level_extraction_unet

Keywords:
Multiphase flow
Gas–liquid interface
Deep learning
Image processing
Convolutional neural network
Videometry

ABSTRACT

The slug flow pattern is one of the most common gas–liquid flow patterns in multiphase transportation pipelines, particularly in the oil and gas industry. This flow pattern can cause severe problems for industrial processes. Hence, a detailed description of the spatial distribution of the different phases in the pipe is needed for automated process control and calibration of predictive models. In this paper, a deep-learning based image processing technique is presented that extracts the gas–liquid interface from video observations of multiphase flows in horizontal pipes. The supervised deep learning model consists of a convolutional neural network, which was trained and tested with video data from slug flow experiments. The consistency of the hand-labelled data and the predictions of the trained model have been evaluated in an inter-observer reliability test. The model was further tested with other data sets, which also included recordings of a different flow pattern. It is shown that the presented method provides accurate and reliable predictions of the gas–liquid interface for slug flow as well as for other separate flow patterns. Moreover, it is demonstrated how flow characteristics can be obtained from the results of the deep-learning based image processing technique.

1. Introduction

Multiphase flow phenomena are often encountered in different sectors of the energy industry, particularly in the oil and gas production, where the two phases of liquid and gas are flowing simultaneously through transportation pipelines (Lin et al., 2020). Field measurements of these flows have a high degree of uncertainty, reaching up to 20% (Elliott et al., 2021). Based on the operating conditions, different flow patterns can form, which describe the spatial distribution of the two phases in the pipe (Hanratty, 2013). One of the most common flow patterns in multiphase transportation pipelines is the slug flow pattern (Al-Kayiem et al., 2017).

Slug flow is characterized by a continuous liquid phase with coherent blocks of aerated liquid, which are separated by volumes of gas, see Fig. 1, left. These aerated blocks of liquid are called slugs. They are moving downstream the pipe on top of a slowly flowing liquid layer at approximately the same velocity as the gas (Hanratty, 2013; Taitel and Dukler, 1977; Al-Safran, 2009). The slug flow pattern can cause severe problems in industrial operations. The pressure drop due to slug flow can be an order of magnitude higher compared to other gas–liquid flow patterns (Taitel and Dukler, 1977), such as stratified or wavy flow, where the two phases are separated by a smooth or wavy interface (Hanratty, 2013). Furthermore, the intermittent sequence of liquid slugs, which can grow to large structures, induces vibrations and stresses when impacting on surfaces of the piping (Hanratty, 2013). These problems can also affect the multiphase flow measurement devices significantly. Thus, a detailed characterization of the flow pattern is required and had already been the subject of many investigations, see, e.g., Pedersen et al. (2017), Olbrich et al. (2020) and Drury et al. (2019). Parameters that are typically used for a characterization of this flow pattern are temporal and spatial scales of the liquid slugs as well as their translational velocities. Spatial scales are for example the slug body length L_b and the slug unit length L_u, i.e. the distance between the slug front and slug rear or between two consecutive slug fronts, respectively. Their corresponding time scales, the slug unit time T_u and the slug body time T_b, are defined as the time that a slug body or a slug unit needs to pass by at a fixed position. Another often used parameter

* Corresponding author at: Physikalisch-Technische Bundesanstalt (PTB), Abbestr. 2-12, 10587 Berlin, Germany.
E-mail address: marc.olbrich@ptb.de (M. Olbrich).

https://doi.org/10.1016/j.ijmultiphaseflow.2022.104247
Received 5 November 2021; Received in revised form 15 June 2022; Accepted 4 September 2022
Available online 10 September 2022

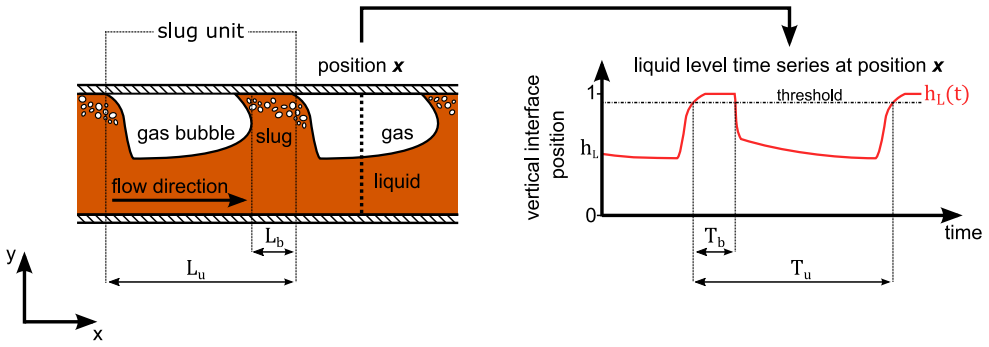

Fig. 1. Illustration of slug flow in a horizontal pipe (left side) with a slug unit, the slug unit length L_u, and the slug body length L_b, as well as the liquid level time series $h_L(t)$ at a fixed position $\boldsymbol{x}$ (right side) with the slug unit time T_u and the slug body time T_b for a given threshold.

is the mean slug frequency, defined as

$$\bar{f}_s = \frac{1}{\bar{T}_u} \quad \text{with} \quad \bar{T}_u = \frac{1}{N_s}\sum_{i=1}^{N_s} T_{u_i}, \tag{1}$$

where N_s denotes the number of slug units in the considered time interval, see Al-Kayiem et al. (2017), Baba et al. (2018), Dukler and Fabre (1994) and Olbrich et al. (2021a). The length and time scales of slug flow are illustrated in Fig. 1. These characteristics are often measured with non-intrusive imaging techniques, such as videometric approaches, where the flow is observed with a high-speed camera through a transparent pipe segment (do Amaral et al., 2013). The flow parameters provided by these type of measurement techniques were used for example to identify the flow pattern (Baghernejad et al., 2019), to verify and investigate flow pattern maps (Crawford, 2018), to investigate shapes of slugs and bubbles for specific operating conditions (do Amaral et al., 2013), to validate numerical simulations (Olbrich et al., 2018), as well as to investigate the effects of slug frequency on induced pipe stresses and develop predictive models and correlations (Mohmmed et al., 2019).

One way to obtain these characteristic parameters is to consider the time series of the vertical position of the liquid–gas interface at a fixed x-position in the pipe, as illustrated on the right side of Fig. 1. This non-dimensional parameter has a range of $[0, 1]$ with respect to the inner pipe diameter D and is hereinafter referred to as the *liquid level time series* at a fixed position x, denoted by $h_L(t)$ (Olbrich et al., 2021a; Schmelter et al., 2021a). It reveals the dynamics of the spatial distribution of the two phases in the pipe and can therefore reliably indicate slugs, waves or other liquid structures, similarly to the hold-up parameter, see Olbrich et al. (2021b). Typically, for analyses of hold-up or liquid level time series, the conventional length and time scales of slug flow are calculated by simple thresholding procedures, see Zhao et al. (2015), Baba et al. (2018), Schmelter et al. (2021a) and Olbrich et al. (2020, 2021b) and Fig. 1.

In this paper, the liquid level time series are derived from high-speed video recordings of gas–liquid flows observed from the side through a transparent pipe section. These flows are two-phase gas–oil and gas–water flows, as well as three-phase gas–oil–water flows, where the liquid phase is a homogeneous mixture of oil and water. For this, a deep learning based image processing technique has been developed. In an earlier work, the time series have been extracted from the video data using a fixed sequence of image filters, see Olbrich et al. (2018). This was similar to other approaches in the field, see e.g., do Amaral et al. (2013) and provided reasonable results for the video data with (exactly) the same conditions it was developed for, such as the colours of the fluids and the background as well as lighting and reflections. However, changes in these conditions as well as noisy data led to incorrect liquid level estimations, and individual adaptations were needed. In contrast to this, deep learning models have the potential to overcome such difficulties and to provide reliable and more versatile image processing techniques.

Deep learning describes a family of learning algorithms in the field of machine learning and artificial intelligence (Emmert-Streib et al., 2020). It is used to learn complex and robust prediction models, e.g., multi-layer neural networks with many hidden units, directly from the data without the need of carefully engineering suitable features (Emmert-Streib et al., 2020; LeCun et al., 2015). Deep learning has a wide range of applications in science, business, and technology, e.g., image or speech recognition, see LeCun et al. (2015), Krizhevsky et al. (2017), Ronneberger et al. (2015) and Graves et al. (2013). However, in the field of multiphase flows, deep learning has only rarely been applied. In the following, we give a short summary on such applications.

For the numerical simulations of multiphase flows, deep learning models were trained for example to approximate the governing equations, estimate simulation errors, predict flow parameters, as well as closure coefficients, see e.g., Wang and Lin (2020), Bao et al. (2020) and Ma et al. (2015). Other applications of deep learning models are for example the correction or prediction of certain parameters for multiphase flow measurements, such as flow rates, phase fractions or velocities, see e.g., Yan et al. (2018), Alakeely and Horne (2021), Dang et al. (2019) and Li et al. (2021). Furthermore, in Lin et al. (2020), a deep learning model is used to predict different two-phase flow patterns in inclined pipes based on superficial velocities of the individual phases and inclination angles. Moreover, image processing techniques based on deep convolutional neural networks have been presented in Poletaev et al. (2020), Haas et al. (2020) and Cerqueira and Paladino (2021) for the detection, reconstruction, and analysis of gas bubbles in vertical pipes and micro-channels, for the recognition of flow patterns in micro pulsating heat pipes (Kamijima et al., 2020; Ahmad et al., 2022) as well as for the extraction of relevant water regions as pre-processing step for two-phase PIV-measurements in the field of ship and ocean engineering (Yu et al., 2021). For the quantification of separated and intermittent gas–liquid flow patterns in horizontal pipes, such as stratified wavy or slug flow, such advanced image processing techniques have not been reported. For this, image filter based methods are typically used, which are sensitive to changes in image quality, contrast, and recording set-up. The deep-learning based image processing technique presented here overcomes these problems to certain extent and provides a quantification for other separated flow pattern, namely, stratified, wavy, plug, and slug flow.

The proposed deep-learning model was trained in a supervised manner to correctly predict the liquid level time series from video recordings of gas–liquid flows. The model, a convolutional neural net, was extensively trained and tested with video data from real slug flow experiments and classifies each region in a video frame into its respective phase being either liquid or gas. For supervised learning the data has to be labelled. To do so, the respective video frames were used to create hand-labelled segmentation maps. Furthermore, the consistency of the hand-labelled data and the predictions of the trained model have been evaluated in an inter-observer reliability test. For further

evaluations of the reliability and versatility of the trained model, data from experiments are considered, which differ from the ones used for training and testing. These data also include an experiment with a different flow pattern, namely a stratified wavy flow.

2. Methods

In this section, the architecture of the convolution neural network as well as the experiments, the data, and its acquisition are described. Furthermore, it is explained, how the deep learning model is used with pre- and post-processing steps to extract the liquid level time series from the video data of the experiments. Moreover, the training and test procedure for the deep learning model is described. Finally, the accuracy and error metrics are provided that are used to evaluate the trained model.

2.1. Convolutional neural network

Deep convolutional neural networks are state-of-the-art machine learning techniques for image classification and segmentation problems (Dhillon and Verma, 2020; Aloysius and Geetha, 2017). In this paper, the liquid level extraction is considered as an image segmentation problem, where regions of liquid and gas need to be identified and segmented in the video frames. For this purpose, a specific convolutional neural network, the so-called U-net, was chosen. This architecture was introduced by Ronneberger et al. (2015) and has been successfully applied in many image-to-image learning problems, e.g., computer tomography, see Mao et al. (2016), Dosovitskiy et al. (2015) and Jin et al. (2017). The U-net is able to achieve accurate results with only few labelled training data and was therefore taken in this paper. The structure was altered from its original form and adapted from Sterbak (2018). The final architecture is illustrated in Fig. 2. An RGB-image input with the dimensions of 128×1024 px is passed through several layers of convolutions comprising a contracting part (left part of the U-shape), a bottleneck with minimal dimension in the centre of the U-shape and an expansive part (right part of the U-shape). The contracting part transfers the input image into a feature map with lower spatial dimensions but a higher number of feature channels. The expansive part generates the resulting segmentation map with the same spatial dimensions as the input image from the lower dimensional feature maps. In Fig. 2, the blue rectangles represent multi-channel feature maps. Here, their dimensions are also given, where the first two entries of the 3-tuple are related to the spatial dimensions (height and length) of the input image and the last entry corresponds to the number of feature channels. The basic operation in this network is the 3×3-convolution, which is followed by a batch normalization operation and a rectified linear unit (ReLU) as activation function. For the contracting part, the spatial dimensions are down-sampled with 2×2-max-pooling operations with stride 2. After each max pooling operation the number of features produced by the 3×3-convolution is doubled. For the expansive part, the feature-maps are up-sampled by 3×3-(up)-convolutions, which halve the number of feature channels, but double the number of spatial dimensions. For additional information in the reconstruction of the higher dimensional map, the feature maps from the corresponding level of the contracting part are copied and concatenated after each up-convolution. Finally, the segmentation map results from a 1×1-convolution and an activation operation using the Sigmoid function. The operations are illustrated as coloured arrows in Fig. 2. For details on the architecture and the operations, see Ronneberger et al. (2015) and Sterbak (2018).

2.2. Experiments

The used deep-learning model was trained and tested with data from video observations of horizontal gas–liquid flows. These flows are two-phase gas–oil or gas–water flows, as well as three-phase gas–oil–water flows, where the liquid phase is a homogeneous mixture of oil and water. The experiments were performed by TÜV SÜD NEL and DNV as part of the projects *Multiphase flow metrology in oil and gas production* (MultiFlowMet I) (Crawford, 2018) and *Multiphase flow reference metrology* (MultiFlowMet II) (Pieper, 2020).

Table 1
Laboratory that conducted the experiments, the set-up for the video recordings (see Fig. 3) and fluid properties for some operating conditions that are used in the experiments.

Lab	Set-up	Fluid	Density in $\mathrm{kg\,m^{-3}}$	Viscosity in cP	Temp. in °C	Pressure in bar (g)
MultiFlowMet I						
NEL	1 & 2	Paraflex oil Brine Water Nitrogen gas	831.40 1037.89 11.51	16 1.15 0.018	20	9
MultiFlowMet II						
NEL	3	Paraflex HT9 Brine Water Nitrogen gas	815.10 1024.19 10.5	7.32 0.65 0.019	45	9
DNV	4	Exxsol D120 Brine Water Nitrogen gas	827.55 1031.69 10.46	5.10 1.04 0.018	18	8

The experimental set-ups are illustrated in Fig. 3. They consist of a horizontal inflow section followed by a vertical measurement section, but here the latter part is of minor interest since the flows in the horizontal pipe are investigated. For the set-up of the MultiFlowMet I project, the horizontal inflow section consists of a straight horizontal pipe with an inner diameter $D = 0.0972\,\mathrm{m}$ and two different lengths $L_{\mathrm{inflow}} \in \{100D, 500D\}$, followed by a transparent Perspex viewing section with a length of $L_{\mathrm{viewSec}} = 5D$. For the set-up of the MultiFlowMet II project, the horizontal inflow section consists of a straight horizontal pipe with an inner diameter $D = 0.066\,64\,\mathrm{m}$ and three different lengths $L_{\mathrm{inflow}} \in \{100D, 300D, 600D\}$, followed by a transparent Perspex viewing section with a length of $L_{\mathrm{viewSec}} = 9D$.

In Table 1, the laboratory that conducted the experiments, the recording set-up for the video data (see also Fig. 3), the fluids and their properties for some operating conditions are given for the two projects, for details see Crawford (2018) and Pieper (2020). In Table 2, the superficial velocities and lengths of the horizontal inflow sections L_{inflow} of the considered two- and three-phase flows of MultiFlowMet I and MultiFlowMet II are given, respectively. For all flows except the stratified wavy flow of Experiment Nr. 13, the slug flow pattern was observed. Please note that, for the stratified wavy flow experiment Nr. 13 and for the slug flow experiments Nr. 1–7 and Nr. 9–12, the interface is clearly visible from the side, which is necessary for the algorithm to work. These experiments have been considered in the training, testing, and evaluation procedure (see Sections 3.1 and 3.3). For the slug flow experiments Nr. 8, 14, 15, and 16, the gas–liquid interface is (partially) unrecognizable due to dispersed phenomena, such as foam or spray. These flows have been considered for the investigations on the limitations of the proposed image processing technique, see Section 4.

The flows were recorded at the viewing sections from the side using a high-speed RGB-camera with a frame rate of 240fps. For each experimental set-up, two different video recording set-ups were used, see Fig. 3. The set-ups 1, 2 and 3 were recorded at NEL, and set-up 4 was recorded at DNV. In set-up 1, the Paraflex oil has an orange–brown colour, the background is black and the viewing section is illuminated from the front. In set-up 2, the Brine water is of grey colour but slightly transparent, the background has a dark blue colour and the viewing section is illuminated from below. In set-up 3, the Paraflex oil (HT9) has a red-brown colour, the background is blue and the viewing section is illuminated from the front. And in set-up 4, the Exxsol oil (D120) is ocher-green, the background has a blue colour and the viewing section is illuminated from behind. Please note that nitrogen gas is

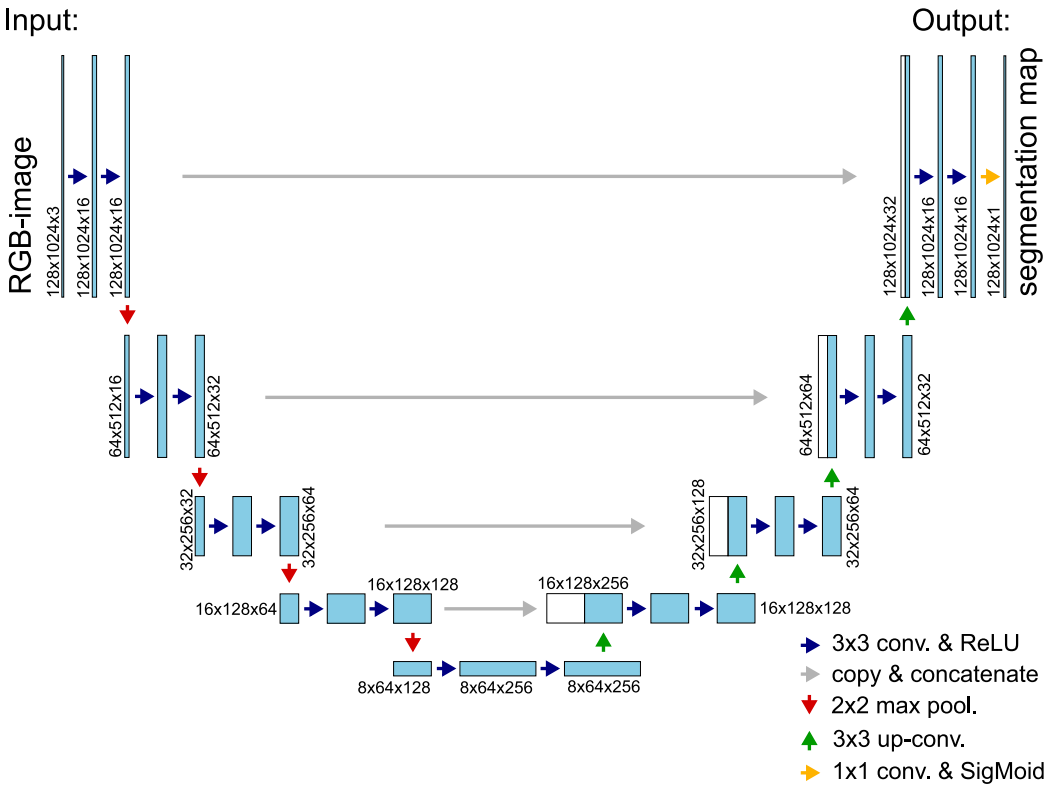

Fig. 2. Illustration of the architecture of the U-net. (For interpretation of the references to colour in this figure legend, the reader is referred to the web version of this article.)

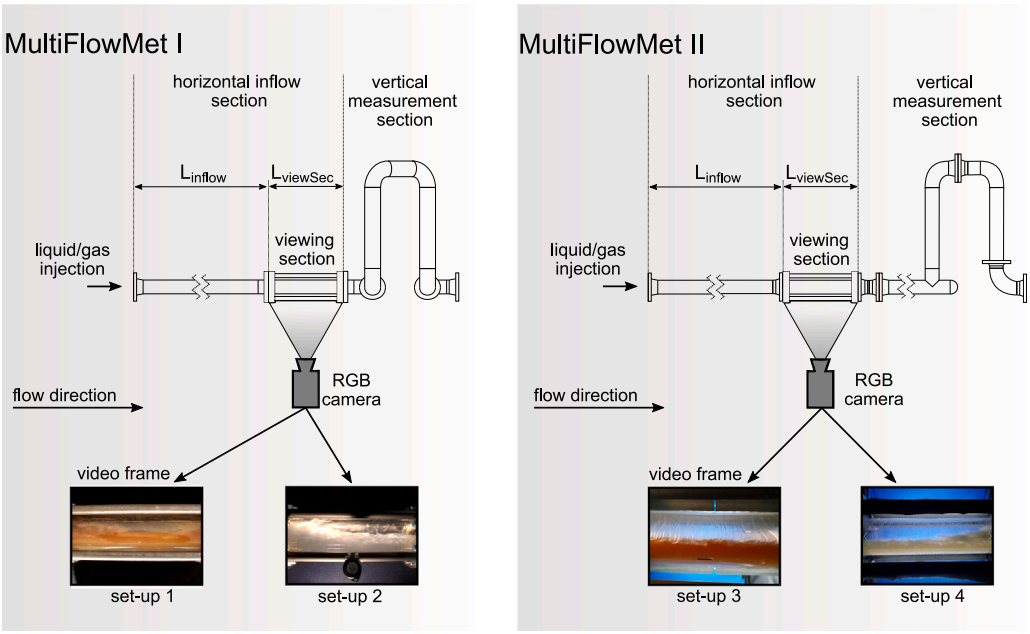

Fig. 3. Illustration of the experimental setting of the projects MultiFlowMet I and MultiFlowMet II with the different recording set-ups. (For interpretation of the references to colour in this figure legend, the reader is referred to the web version of this article.)

transparent and colourless, similar to other common gases in the oil and gas industry, e.g., natural gas and argon (Pieper, 2020). Hence, the background colour is visible through the gas for all recording set-ups. Furthermore, for the three-phase gas–oil–water flows recorded in set-up 1, 3 and 4, the watercut is relatively small. Hence, the water does not form a separate liquid layer and the liquid phase appears in the video observations as a homogeneous oil–water mixture with similar colour as the oil. In Tables 3 and 6, the video recording set-up as well as the recorded time (length of the videos) are given for the considered experiments of MutliFlowMet I and II.

2.3. Pre- and post-processing

The U-net, described in Section 2.1, is used to segment liquid and gas regions in parts of the video frames. However, before the U-net is applied, the video frames need to be prepared in several

Table 2
Superficial velocities $v_s^{oil}, v_s^{water}, v_s^{gas}$ and lengths of inflow section L_{inflow} in inner diameters D for the considered experiments of the MultiFlowMet I & II project.

Experiment	Superficial velocities in $m\,s^{-1}$			L_{inflow}
	v_s^{oil}	v_s^{water}	v_s^{gas}	in D
MultiFlowMet I				
Nr. 1	1.349	0	1.692	100, 500
Nr. 2	1.869	0	0.627	100
Nr. 3	1.930	0	0.751	100, 500
Nr. 4	2.547	0	3.185	100, 500
Nr. 5	0.986	0.328	2.849	100
Nr. 6	1.963	0.638	0.892	100
Nr. 7	0	1.847	0.678	100
Nr. 8	3.386	0	1.276	100
MultiFlowMet II				
Nr. 9	0.822	0	3.285	100, 300, 600
Nr. 10	1.218	0	1.179	100, 300, 600
Nr. 11	1.610	0	0.704	100, 300, 600
Nr. 12	2.390	0.006	2.398	100
Nr. 13	0.475	0	3.246	100
Nr. 14	2.352	1.559	1.548	100
Nr. 15	0.399	0	7.699	100
Nr. 16	0.739	0.470	11.442	100

pre-processing steps. Furthermore, to extract a time series from the gas–liquid segmentation maps of the U-net, additional post-processing steps are necessary.

In Fig. 4, the complete processing pipeline of the liquid level extraction from the video observations is illustrated. The first step is to extract a vertical line (pixelcolumn) through the pipe at a fixed x-position for every frame, i.e., time step, and stack it. From this procedure, an RGB-pixelcolumn over time is obtained, which represents the phase distribution along the observed vertical line through the pipe and its temporal changes at a fixed x-position. Because of this, the gas–liquid interface visible in this image is associated with the liquid level time series with respect to the inner pipe diameter. Under this construction, the frame rate of the video represents the sample rate of the time series. Therefore, the RGB-pixelcolumn over time provides the basis for further calculations. In the second step, the RGB-pixelcolumn over time is interpolated to a uniform height (y-component) of $128\,px$ and cut into segments with a length (t-component) of $1024\,px$, to meet the input dimension criterion for the chosen U-net architecture. In the third step, the evenly sized segments are normalized to reduce the influence of disturbances in the video recording set-up, such as differences in luminance or colour. For this normalization, the *z-score* (also called statistical standardization or standard score, see Larsen and Marx (2012)) is applied RGB-component wise. This step completes the pre-processing and the standardized image segments are passed to the U-net to perform the segmentation. The output of the U-net is a continuous segmentation map with values in $[0, 1]$, where 1 (white) indicates gas and 0 (black) indicates liquid. In the first post-processing step, the continuous segmentation maps are binarized (with a threshold of 0.5) to obtain a sharp gas–liquid interface. Afterwards, the segments are concatenated in correct order to get a segmentation map for the complete RGB-pixelcolumn over time. In the last step, the vertical position of the gas–liquid interface (edge between black and white regions) is detected in the binarized and concatenated segmentation map. In case of multiple vertical interface positions at one time step, such as for bubbles or droplets, the values are averaged to get a unique representation of the interface over time. This ensures the property of a mathematically well-defined function for the extracted liquid level time series in case of multiple vertical interface positions such that it can be used for further time series analyses. It should be noted that this averaging can lead to a misrepresentation of certain flow structures in the liquid level time series. With this procedure the liquid level time series are obtained from the video recordings of multiphase flows. The code for the extraction of the liquid level time series from the RGB-pixelcolumns over time is available as Jupyter Notebook in Olbrich et al. (2021c).

2.4. Training and testing

The U-net was trained and tested with data from horizontal gas–liquid slug flows. For this, the video data of 18 different slug flows were used. That includes data from 9 experiments of the MultiflowMet I project and 9 experiments of the MultiflowMet II project, specifically Nr. 1 – 6, as well as Nr. 9 – 11 for all inflow lengths, see Table 3. For the testing in the optimization process of the training procedure, a subset of the data is needed, which is disjoint to the training data. Here, the randomly chosen two experiments Nr. 5 - $100D$ and Nr. 11 - $300D$ are used for testing and the remaining 16 experiments are used for training. Please note that the naming of the individual experiments are given in the form of (Nr. - L_{inflow}).

To prepare the video data for the training of the U-net, the RGB-pixel-columns over time are extracted and normalized as described in Section 2.3 and Step 1 – 4 in Fig. 4. Furthermore, binary segmentation masks are needed as reference in the training and testing process, which represent a correct classification into gas and liquid. These masks were generated from hand-labelled gas–liquid interfaces in the RGB-pixelcolumns over time for all experiments. They have a sharp interface with values of 1 for gas and 0 for liquid. Since they are extracted from the RGB-pixelcolumns over time, the masks represent an approximation of the temporally resolved gas volume fraction fields in a vertical line through the pipe at a fixed position. In the training and testing of the U-net, the masks are compared with the predicted segmentation maps to determine an accuracy for the prediction. For this, the masks are also transformed into evenly sized segments of $128 \times 1024\,px$ (see Step 2 in Fig. 4). This results in 483 pairs of evenly sized RGB-segments and corresponding mask segments for the training set as well as 61 of such pairs for the test set.

Since the segmentation includes only 2 classes, i.e., gas and liquid, the *binary accuracy* function was chosen as accuracy metric, see Eq. (2) and Chollet et al. (2015). Furthermore, for the training process the stochastic gradient descent optimization method *adaptive moment estimation (ADAM)* was set together with the *binary cross-entropy*-loss function and a dropout of 5%. Details can be found in Ronneberger et al. (2015), Sterbak (2018), Chollet et al. (2015) and Kingma and Ba (2017). For the training, the dropout-layer is located after every max-pooling operation in the contracting part of the U-net and after every concatenation-operation in the expansive part of the U-net, see Fig. 2. Furthermore, a mini batch size of 32 was used to train the U-net over a maximum number of 50 epochs. Early stopping (Prechelt, 1998) was applied. For details, see Sterbak (2018) and Chollet et al. (2015). The model was trained and tested using *python* version 3.7, *tensorflow* version 2.3 and *Keras* version 2.4.3, see Chollet et al. (2015) and Abadi et al. (2015). The implementation of the model, the code for the training of the model as Jupyter Notebook, and the weights of the trained model are available in Olbrich et al. (2021c).

2.5. Accuracy and error metrics

In this section, the metrics are given, which are used to evaluate the segmentation maps from the U-net as well as the extracted liquid level time series.

The binary accuracy of a predicted segmentation map A^{pred} and a corresponding mask A^{mask} is given by

$$acc_{bin}(A^{pred}, A^{mask}) = \frac{1}{N_t \cdot N_y} \sum_{i=1}^{N_t} \sum_{j=1}^{N_y} \phi\left(A_{ij}^{pred}, A_{ij}^{mask}\right), \quad (2)$$

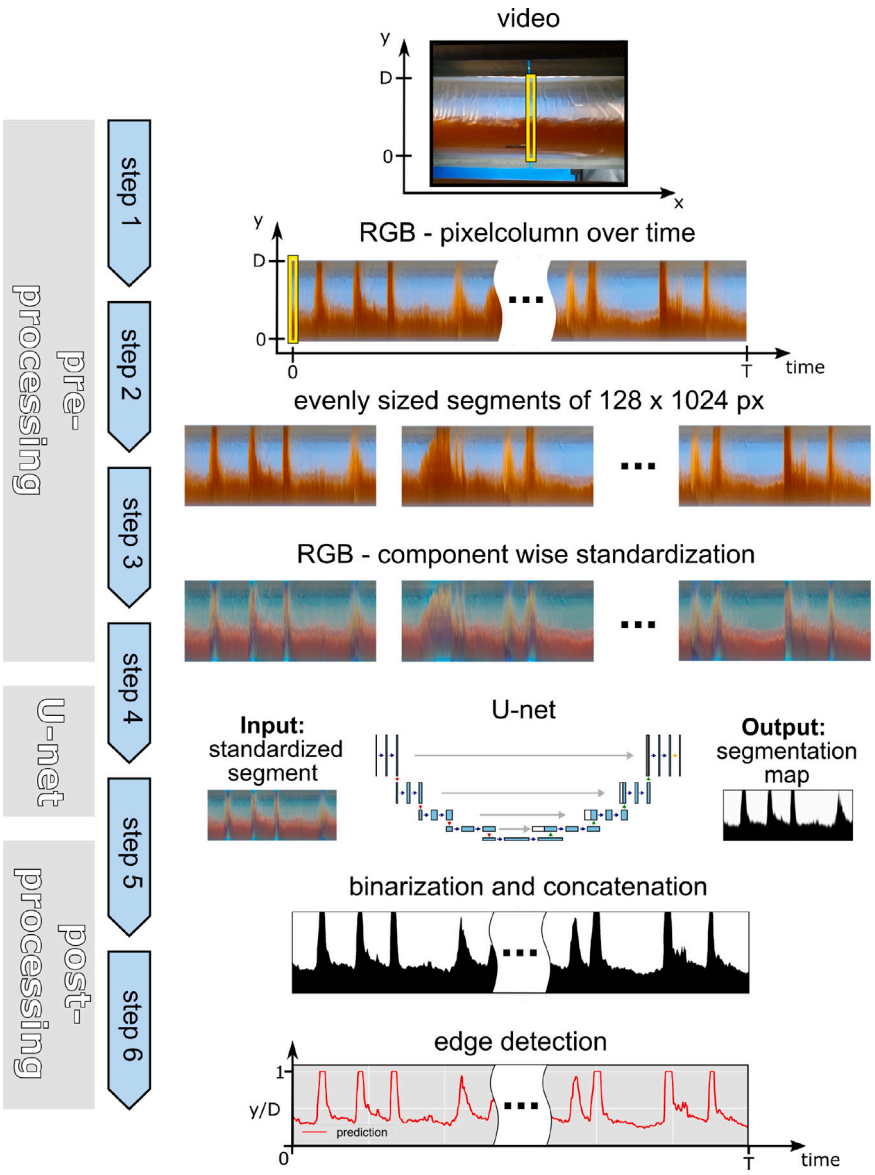

Fig. 4. Illustration of the processing pipeline from the raw video observations to the final liquid level time series. (For interpretation of the references to colour in this figure legend, the reader is referred to the web version of this article.)

where N_t and N_y denote the number of pixels of the mask in t-direction and y-direction, respectively, and the pixelwise binary evaluation function ϕ is given by

$$\phi(A_{ij}^{\text{pred}}, A_{ij}^{\text{mask}}) = \begin{cases} 1, & \text{if } A_{ij}^{\text{pred}} > 0.5 \wedge A_{ij}^{\text{mask}} > 0.5 \\ 1, & \text{if } A_{ij}^{\text{pred}} \leq 0.5 \wedge A_{ij}^{\text{mask}} \leq 0.5 \\ 0, & \text{else.} \end{cases} \tag{3}$$

Then, ϕ indicates if a pixel in the predicted segmentation map was successfully classified as gas or liquid. This function is pre-implemented in the open source software library *Keras*, see Chollet et al. (2015).

The deviation of the liquid level times series, which are extracted from the hand-labelled segmentation map h_L^{mask} and the U-net output h_L^{pred} can be measured in terms of the mean absolute error (MAE), given by

$$\epsilon(h_L^{\text{pred}}, h_L^{\text{mask}}) = \frac{1}{N_t} \sum_{i=1}^{N_t} \left| h_L^{\text{pred}}(t_i) - h_L^{\text{mask}}(t_i) \right|. \tag{4}$$

3. Results

In this section, the results of the liquid level extraction with the deep learning model are presented for the training and testing procedure, as well as for additional evaluations on different data sets. The results include the accuracy of the predicted segmentation maps with respect to the hand-labelled masks and the mean absolute error of the extracted liquid level time series. Furthermore, the consistency of the hand-labelled data and the prediction is investigated in an inter-observer reliability test. Moreover, the limitations of the proposed image processing technique are demonstrated and discussed.

3.1. Training and testing

The U-net was trained on a set of 483 pairs and tested on a set of 61 pairs of RGB-images from horizontal slug flow and corresponding masks, as described in Sections 2.3 and 2.4. The training was terminated after 42 epochs due to early stopping. The best model was found after 31 epochs. For this model, a mean binary accuracy of 97.91%

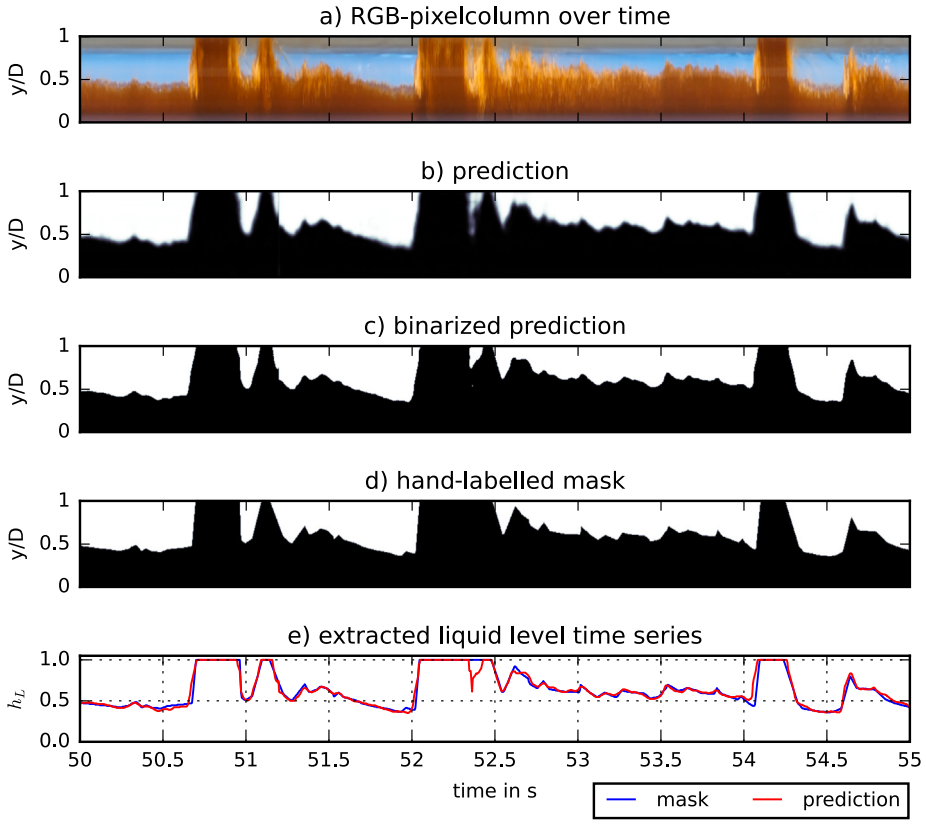

Fig. 5. Prediction of the U-net and extracted liquid level from Experiment Nr. 10 - 100D in comparison with hand-labelled mask for the interval [50 s, 55 s].

for the training set and a mean binary accuracy of 97.74% for the test set, was achieved. These accuracies are high compared to the reported training and test accuracies in between 89% and 98.7% of other successfully trained deep-learning based gas and liquid segmentation models, see e.g. Cerqueira and Paladino (2021), Yu et al. (2021) and Ahmad et al. (2022).

In Fig. 5, the RGB-pixelcolumn over time from Experiment Nr. 10 - 100D, the prediction of the U-net, its binarization, the corresponding hand-labelled mask, as well as the extracted liquid level time series are given. Please note that, Experiment Nr. 10 - 100D belongs to the training set. The prediction of the U-net and its binarization show good agreement with the mask. Furthermore, the gas and liquid regions are segmented in more detail in the prediction, compared to the hand-labelled mask, as can be seen for instance at the slug between 52 s and 52.5 s in Fig. 5. Here, the hand-labelled mask shows one larger slug, but the prediction shows two slugs, which are separated by a short gas bubble and foam. Due to the foamy areas between the rear of the first slug and the front of the second slug, this (optical) separation is not obvious. Nevertheless, the separation of the two slugs can be verified in the RGB-pixelcolumn over time, see Fig. 5a. Hence, in this case, the prediction from the trained model is more consistent and detailed compared to the hand-labelled mask on which it was trained.

In Table 3, the binary accuracy (see Eq. (2)) of the predictions and the masks in full length, as well as the mean absolute error (see Eq. (4)) of the extracted liquid level time series from prediction and mask are given for all experiments used for training and testing. The binary accuracy of the segmentation maps varies from 96.86% to 98.85% and the mean absolute error of the liquid level time series varies from 1.15% to 3.12%. From these high accuracies and low errors for the training and testing, it can be concluded, that the model performs well for the considered types of data. Furthermore, since the net accurately predicts the segmentation maps also for the two test sets that were not used in training, it is able to generalize to unseen data from both experimental set-ups, respectively.

Table 3
The number of the experiment, the recording set-up, the recorded time (length of the video), the belonging to training or test set, the binary accuracy $acc_{\text{bin}}(A^{\text{pred}}, A^{\text{mask}})$ (see Eq. (2)) of the predicted segmentation map and corresponding mask as well as the mean absolute error $\epsilon(h_L^{\text{pred}}, h_L^{\text{mask}})$ (see Eq. (4)) of the liquid level time series, extracted from prediction h_L^{pred} and mask h_L^{mask} are given for all experiments used for training and testing.

Experiment (Nr. - L_{inflow})	Set-up	Rec. time in s	Training or Test	acc_{bin} in %	ϵ in %
Nr. 1 - 100D	1	122	Training	98.01	2.00
Nr. 1 - 500D	1	150	Training	98.65	1.38
Nr. 2 - 100D	1	150	Training	97.91	2.08
Nr. 3 - 100D	1	150	Training	98.17	1.82
Nr. 3 - 500D	1	150	Training	98.85	1.15
Nr. 4 - 100D	1	150	Training	97.40	2.59
Nr. 4 - 500D	1	150	Training	97.73	2.26
Nr. 6 - 100D	1	150	Training	97.15	2.85
Nr. 9 - 100D	3	122	Training	96.86	3.12
Nr. 9 - 300D	3	126	Training	97.61	2.41
Nr. 9 - 600D	3	121	Training	97.73	2.31
Nr. 10 - 100D	3	122	Training	97.54	2.45
Nr. 10 - 300D	3	125	Training	98.37	1.62
Nr. 10 - 600D	3	123	Training	98.47	1.52
Nr. 11 - 100D	3	122	Training	97.86	2.13
Nr. 11 - 600D	3	123	Training	98.12	1.84
Nr. 11 - 300D	3	123	Test	97.72	2.26
Nr. 5 - 100D	1	150	Test	97.75	2.42

3.2. Inter-observer test

In this section, the inter-observer reliability is considered to evaluate the consistency of the hand-labelled data sets, which were used for the training of the U-net. For this, three independent observers have labelled the gas–liquid interface for the first 60 s of four chosen experiments from the training and test set, namely Nr. 5 - 100D, Nr. 6 - 100D, Nr. 9 - 100D and Nr. 10 - 300D (see Table 3). Please note

Table 4
The Pearson-correlation values for the pairwise comparison of the different labels.

Experiment	$r(h_L^{\text{obs}_1}, h_L^{\text{obs}_2})$	$r(h_L^{\text{obs}_1}, h_L^{\text{obs}_3})$	$r(h_L^{\text{obs}_2}, h_L^{\text{obs}_3})$
Nr. 5 - $100D$	0.973	0.965	0.969
Nr. 6 - $100D$	0.920	0.981	0.880
Nr. 9 - $100D$	0.938	0.914	0.931
Nr. 10 - $300D$	0.985	0.981	0.977

Table 5
The Pearson-correlation values for the pairwise comparison of the prediction with the different labels.

Experiment	$r(h_L^{\text{pred}}, h_L^{\text{obs}_1})$	$r(h_L^{\text{pred}}, h_L^{\text{obs}_2})$	$r(h_L^{\text{pred}}, h_L^{\text{obs}_3})$
Nr. 5 - $100D$	0.970	0.970	0.962
Nr. 6 - $100D$	0.954	0.933	0.901
Nr. 9 - $100D$	0.970	0.962	0.939
Nr. 10 - $300D$	0.993	0.987	0.981

that, the U-net was trained and tested with labels from Observer 1. The inter-observer or inter-rater reliability (IRR) is defined as the degree of relationship between the labels of different observers that are operating independently (Kottner and Dassen, 2008; Tinsley and Weiss, 1975). Here, the IRR for the hand-labelled time series is quantified by the normalized cross-correlation coefficient. In the IRR-context, this coefficient is also referred to as *Pearson's r* or *Pearson-correlation*, see Kottner and Dassen (2008) and Berman (2016).

For every experiment, the labelled data sets of the different observers show a strong correlation to each other with values in between 0.88 and 0.985, see Table 4. This indicates a high degree of relation between the hand-labelled liquid level time series of the different observers. Hence, the hand-labelled liquid level time series show consistency and reliability among the different observers and are therefore suited for the training of the U-net. This correlation was calculated using the function *pearsonr* of python's SciPy module (Virtanen et al., 2020). Please note that, it returned p-values for the null-hypothesis significance testing of less then 0.001 for all cases. Furthermore, this analysis is applied to the prediction of the U-net to quantify the degree of relation between the prediction and the labels of the independent observers, see Xiao et al. (2017).

As given in Table 5, the Pearson-correlation values for the pairwise comparisons of the prediction and the labels of the different observers reach from 0.901 to 0.993 with p-values of less then 0.001 for all cases. This shows a strong correlation in a similar range as for the observers (see Table 4), and therefore, indicates a consistency between the predictions of the U-net and the labels of the independent observers.

In addition to the Pearson-correlation, the pointwise errors between the hand-labelled time series of the different observers as well as between the labels and the prediction of the U-net are considered. For a quantification of the error between the observers, the three time series of the pointwise errors between the different observers $|h_L^{\text{obs}_i}(t_k) - h_L^{\text{obs}_j}(t_k)|_{k=1,\dots,N_t}$ for $i \neq j \in \{1,2,3\}$ are ensemble-averaged (Walburn et al., 1983) to obtain one time series of the average pointwise error in between the observer for every experiment, i.e.,

$$\langle |h_L^{\text{obs}_i} - h_L^{\text{obs}_j}| \rangle (t_k) = \frac{1}{3} \sum_{i \neq j \in \{1,2,3\}} |h_L^{\text{obs}_i}(t_k) - h_L^{\text{obs}_j}(t_k)|, \text{ for every } t_k. \quad (5)$$

The same is done for the comparison of h_L^{pred} and $h_L^{\text{obs}_j}$ with $j \in \{1,2,3\}$. These ensemble-averages are shown as boxplots on the right side of Fig. 6. Here, the boxplots represent the distribution of these errors. It can be seen that, the statistical quantities (mean, median) and ranges (interquartile range and range between 5th and 95th percentile) of the errors are smaller for $\langle |h_L^{\text{pred}} - h_L^{\text{obs}_j}| \rangle$ compared to $\langle |h_L^{\text{obs}_i} - h_L^{\text{obs}_j}| \rangle$ for all experiments. On the left side of Fig. 6, the range in between the minima and maxima of the liquid level time series for every time point, labelled by the three observers, are given for the interval of 5 s. This range represents a tolerance in the observation of the gas–liquid interface or the liquid level. In addition to this, the liquid level time series from the prediction of the U-net is superimposed. Here, it can be seen that, the predicted time series is near or in the tolerance range.

Table 6
The number of the experiment, the recording set-up, the recorded time (length of the video), the binary accuracy $acc_{\text{bin}}(A^{\text{pred}}, A^{\text{mask}})$ (see Eq. (2)) of the predicted segmentation map and corresponding mask as well as the mean absolute error $\epsilon(h_L^{\text{pred}}, h_L^{\text{mask}})$ (see Eq. (4)) of the liquid level time series, extracted from prediction h_L^{pred} and mask h_L^{mask} for the three additional independent evaluations.

Experiment (Nr. - L_{inflow})	Set-up	Rec. time in s	acc_{bin} in %	ϵ in %
Nr. 7 - $100D$	2	60	96.99	3.00
Nr. 12 - $100D$	4	60	95.41	4.92
Nr. 13 - $100D$	3	60	97.68	2.32

Altogether, the hand-labelled parameters of the different observers have a strong correlation as well as low pointwise errors between each other. Hence, this parameter shows consistency in between the observers and is therefore a reliable parameter for the training of the U-net. Furthermore, the comparison of the predicted liquid level time series with the observers show not only similarly strong correlation values, but also smaller statistical quantities of the considered pointwise errors. Hence, the predictions of the U-net also provide liquid level time series, which are consistent with respect to the different observers.

3.3. Further evaluations on different data sets

For further evaluations on the reliability and versatility of the trained model, data from three additional experiments are considered, which differ from the ones used for training and testing.

The model was trained and tested for Paraflex oil–nitrogen slug flows with black or blue background (recording set-up 1 and 3), see Fig. 3 and Section 2.4. In contrast to this, the flows considered in this section are either recorded in a different set-up with different fluids, or for a different flow pattern. They inlcude the brine water–nitrogen slug flow experiment Nr. 7 - $100D$ from recording set-up 2 with grey liquid colour and dark blue background, the Exxsol oil–nitrogen slug flow experiment Nr. 12 - $100D$ from recording set-up 4 with an ocher-green liquid colour, and the stratified wavy Paraflex oil–nitrogen flow experiment Nr. 13 - $100D$ from recording set-up 3. Please note that, also the lighting conditions and occurring reflections differ from the training and test set, e.g., reflections in the back of the pipe for Experiment Nr. 7 - $100D$ and white colour on top of the slugs for Experiment Nr. 12 - $100D$, see Fig. 7. These differences are causing changes in contrast and RGB-intensity values. Together with the different flow pattern, this leads to a change in conditions for the model, compared to the training and testing data.

In Table 6, the binary accuracy of the prediction and the corresponding hand-labelled masks as well as the mean absolute error of the extracted liquid level time series are given. For the Brine water–nitrogen slug flow of Experiment Nr. 7 - $100D$, the binary accuracy of 96.99% and the error value of 3% are in the same ranges as for the training and testing that are $[96.86\%, 98.85\%]$ and $[1.15\%, 3.12\%]$, respectively. The same holds for the stratified wavy flow of Experiment Nr. 13 - $100D$, with a binary accuracy of 97.68% and an error of 2.32%. The prediction for the slug flow experiment Nr. 12 - $100D$ did not achieve such high accuracy as the other experiments. Nevertheless, with a binary accuracy of 95.41% and an error of 4.92%, it is still close to the other values and a reasonable result.

In Fig. 7, the RGB-pixelcolumn over time with the extracted liquid levels from the prediction and the hand-labelled mask are given for a time interval of 5 s for experiment Nr. 7 - $100D$, Nr. 12 - $100D$ and Nr. 13 - $100D$. As it can be seen in Fig. 7(i), the liquid level from the prediction for the brine water - nitrogen slug flow experiment Nr. 7 - $100D$ shows a frequent underestimation in foamy areas in between shorter slugs.

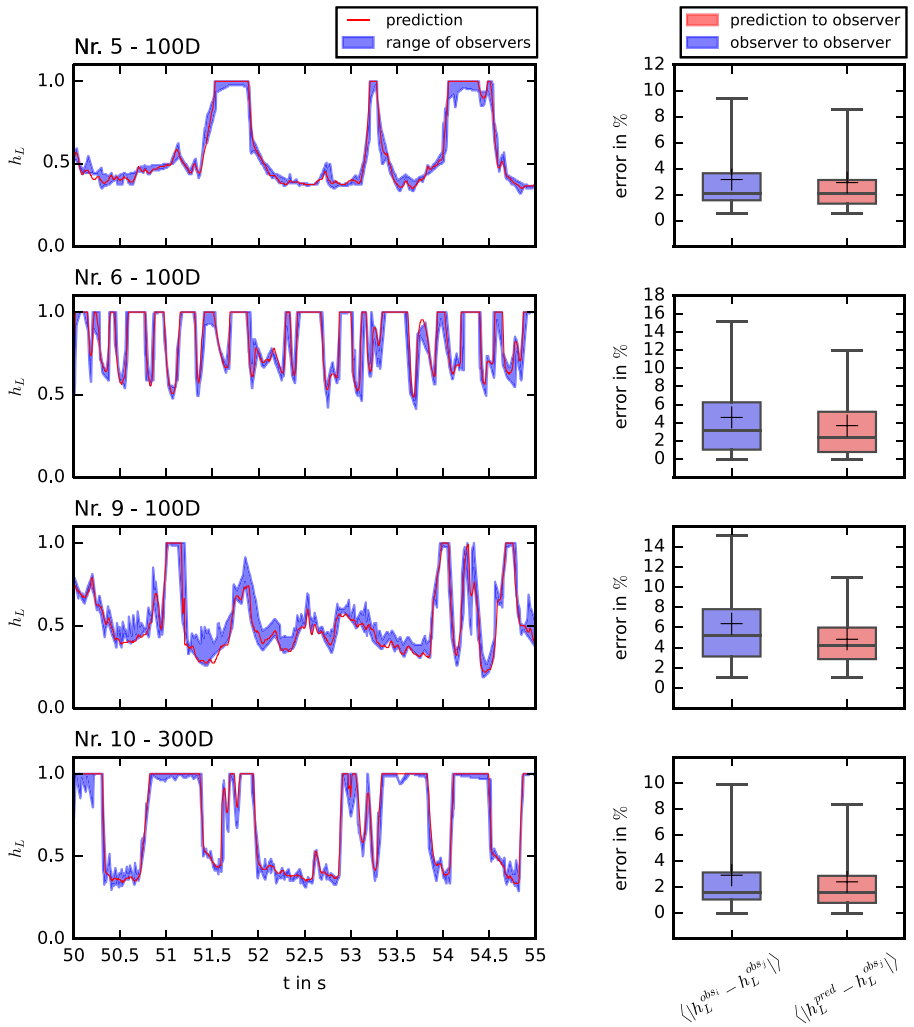

Fig. 6. Inter-observer comparison with prediction for the slug flow experiments Nr. 5 - 100D, Nr. 6 - 100D, Nr. 9 - 100D and Nr. 10 - 300D. **Left:** range of hand-labelled liquid level time series by the three independent observers and superimposed prediction for 5 s. **Right:** Boxplots of the ensemble-averaged point wise differences between the observers and between prediction and observers. Please note, the whiskers in the boxplots represents the 5th and 95th percentile, the coloured box represents the interquartile range (Q3-Q1), the horizontal line in the box represents the median, and the black cross represents the mean. (For interpretation of the references to colour in this figure legend, the reader is referred to the web version of this article.)

For the Exxsol oil - nitrogen slug flow experiment Nr. 12 - 100D in Fig. 7(ii), the prediction shows differences for slugs that are close to each other, see for instance the slugs at [50 s, 50.5 s] and [52 s, 52.5 s]. Furthermore, for this flow, the slug rears are predicted later compared to the mask. One reason for this is the liquid film that flows down on the inner walls of the pipe after a slug passed by. This also causes the top of the slugs to appear smeared out in the RGB-pixelcolumn over time and leads to the differences in between prediction and mask. Apart from the aforementioned deviations, the liquid level time series from the prediction and mask are in good agreement for all three flows.

In addition to this evaluation, the two previously unseen slug flow experiments Nr. 7 - 100D and Nr. 12 - 100D are further validated in the same manner as in the inter-observer test in Section 3.2. Therefore, the three independent observers have labelled the gas–liquid interface of these two slug flows. For the validation, the Pearson-correlation r between the different observers, as well as between the prediction and the observers, are considered, see Tables 7 and 8. Furthermore, the ensemble-averaged pointwise errors $\langle|h_L^{\text{pred}} - h_L^{\text{obs}_j}|\rangle$ and $\langle|h_L^{\text{obs}_i} - h_L^{\text{obs}_j}|\rangle$ are considered for this evaluation, see Fig. 8.

For the two additional experiments, the hand-labelled data sets of the different observers show a strong correlation to each other with values in between 0.922 and 0.974 and p-values of less then 0.001, see Table 7. These values are similar to the ones obtained for the inter-observer test in Section 3.2 and indicate a high degree of relation between the hand-labelled liquid level time series of the different observers. The Pearson-correlation values for the pairwise comparisons of the prediction and the labels of the different observers reach from 0.868 to 0.967 with p-values of less then 0.001, see Table 8. This also shows a strong correlation and, therefore, indicates a consistency between the predictions of the U-net and the labels of the independent observers.

Table 7
The Pearson-correlation values for the pairwise comparison of the different labels.

Experiment	$r(h_L^{\text{obs}_1}, h_L^{\text{obs}_2})$	$r(h_L^{\text{obs}_1}, h_L^{\text{obs}_3})$	$r(h_L^{\text{obs}_2}, h_L^{\text{obs}_3})$
Nr. 7 - 100D	0.974	0.958	0.953
Nr. 12 - 100D	0.941	0.942	0.922

As mentioned in the discussion of Fig. 7, the predictions of the liquid level time series for Experiment Nr. 7 - 100D and Nr. 12 - 100D show some systematic deviations from the hand-labelled data. For the previously unseen nitrogen-water slug flow Experiment Nr. 7 - 100D, the prediction of the liquid level at the aerated liquid film region behind the slugs is often lower compared to the hand-labelled data. Moreover, for the previously unseen nitrogen–oil–water slug flow Experiment

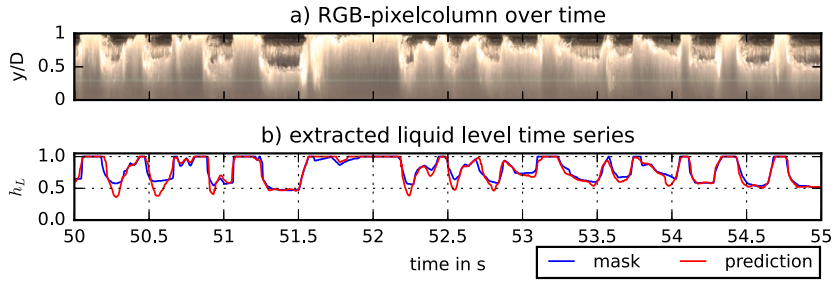

(i) Experiment Nr. 7 - 100D

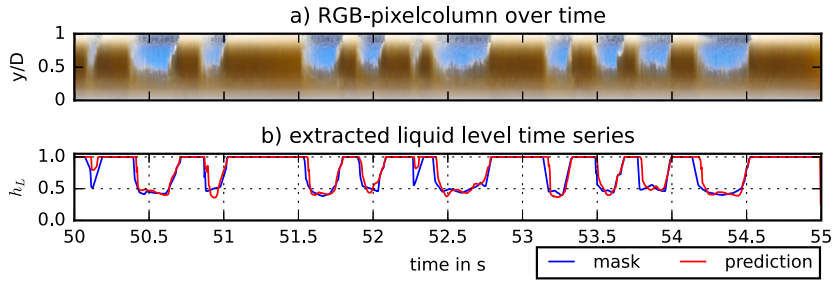

(ii) Experiment Nr. 12 - 100D

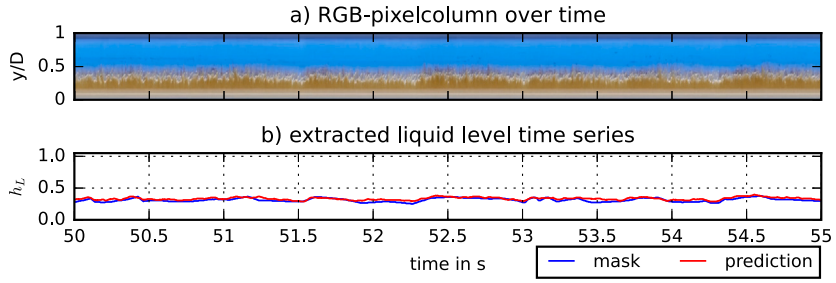

(iii) Experiment Nr. 13 - 100D

Fig. 7. Visualization of the results for three untrained flows and set-ups. For each experiment, the RGB-pixelcolumn over time and the extracted liquid level from the binarized prediction and the corresponding mask are given for the time interval [50 s, 55 s]. (For interpretation of the references to colour in this figure legend, the reader is referred to the web version of this article.)

Table 8
The Pearson-correlation values for the pairwise comparison of the prediction with the different labels.

Experiment	$r(h_L^{\text{pred}}, h_L^{\text{obs}_1})$	$r(h_L^{\text{pred}}, h_L^{\text{obs}_2})$	$r(h_L^{\text{pred}}, h_L^{\text{obs}_3})$
Nr. 7 - 100D	0.967	0.957	0.946
Nr. 12 - 100D	0.905	0.900	0.868

Nr. 12 - 100D, the slug rears often appear later in the prediction compared to the hand-labelled data. This is also shown in Fig. 8. This behaviour leads to slightly lower (but still high) Pearson-correlation values between the prediction and the observers for Experiment Nr. 12 - 100D compared to Experiment Nr. 7 - 100D. Furthermore, this also leads to a slightly larger variation in the ensemble-averaged pointwise errors $\langle |h_L^{\text{pred}} - h_L^{\text{obs}_j}| \rangle$, compared to $\langle |h_L^{\text{obs}_i} - h_L^{\text{obs}_j}| \rangle$ for both experiments, see Fig. 8. Nevertheless, the liquid level predictions of both experiments are near or in the tolerance range of the observers, see left side of Fig. 8. Moreover, the statistical parameters of the ensemble-averaged pointwise errors between the predictions and the observers $\langle |h_L^{\text{pred}} - h_L^{\text{obs}_j}| \rangle$ are very similar to the ones between the different observers $\langle |h_L^{\text{obs}_i} - h_L^{\text{obs}_j}| \rangle$, see right side of Fig. 8. Hence, for the two difficult unseen slug flow experiments Nr. 7 - 100D and Nr. 12 - 100D, a strong consistency between the prediction and the observers can be concluded.

In the further, slug flow characteristics are calculated from the extracted liquid level time series for Experiment Nr. 12 - 100D. The characteristics considered in this paper are the slug unit times T_u, the slug body times T_b, as well as their mean values, the mean slug frequency $\bar{f}_s$, the mean slug unit length $\bar{L}_u$, the mean slug body length $\bar{L}_b$, as well as the mean translational velocity of the slugs $\bar{u}_{\text{slug}}$, see Fig. 1 and Eq. (1). Considering these slug characteristics that can be obtained from the predicted time series exemplifies the physical insights provided by the results of the proposed image processing technique. It also allows further validation of the predicted time series. In that regard, it is shown that the predicted liquid level time series provide reasonable slug characteristics, also for the unseen data of Experiment Nr. 12 - 100D with the lowest accuracy and largest error values of all considered cases ($acc_{\text{bin}}(A^{\text{pred}}, A^{\text{mask}}) = 95.41\%$, $\epsilon(h_L^{\text{pred}}, h_L^{\text{mask}}) = 4.92\%$), see Tables 3 and 6.

In Fig. 9a, the predicted and hand-labelled liquid level time series of Experiment Nr. 12 - 100D are given for a time interval of 5 s, similar to Fig. 7(ii). For the calculation of the slug unit times T_u and slug body times T_b, a threshold value of 0.95 has been set to detect the slug fronts

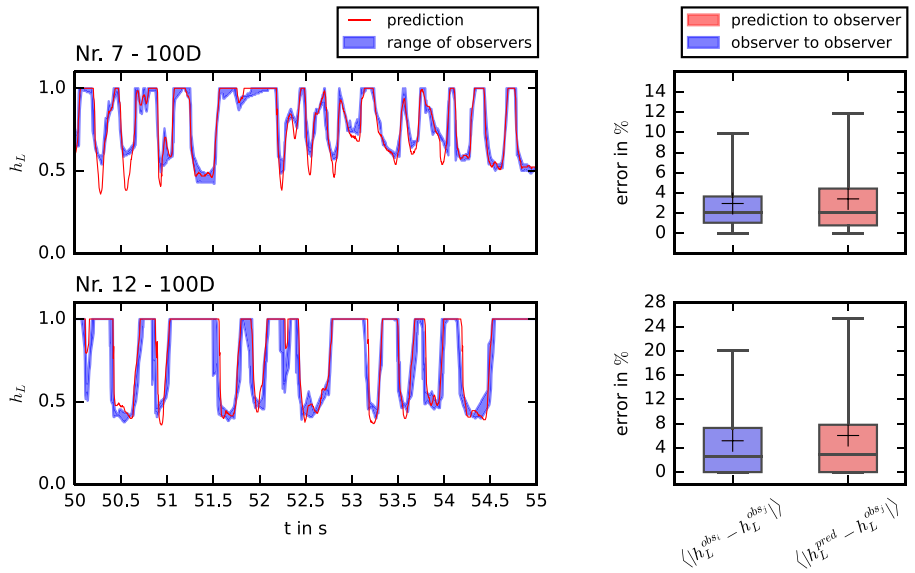

Fig. 8. Inter-observer comparison with prediction for the slug flow experiments Nr. 7 - 100D and Nr. 12 - 100D. **Left:** range of hand-labelled liquid level time series by the three independent observers and superimposed prediction for 5 s. **Right:** Boxplots of the ensemble-averaged point wise differences between the observers and between prediction and observers. Please note, the whiskers in the boxplots represents the 5th and 95th percentile, the coloured box represents the interquartile range (Q3-Q1), the horizontal line in the box represents the median, and the black cross represents the mean. (For interpretation of the references to colour in this figure legend, the reader is referred to the web version of this article.)

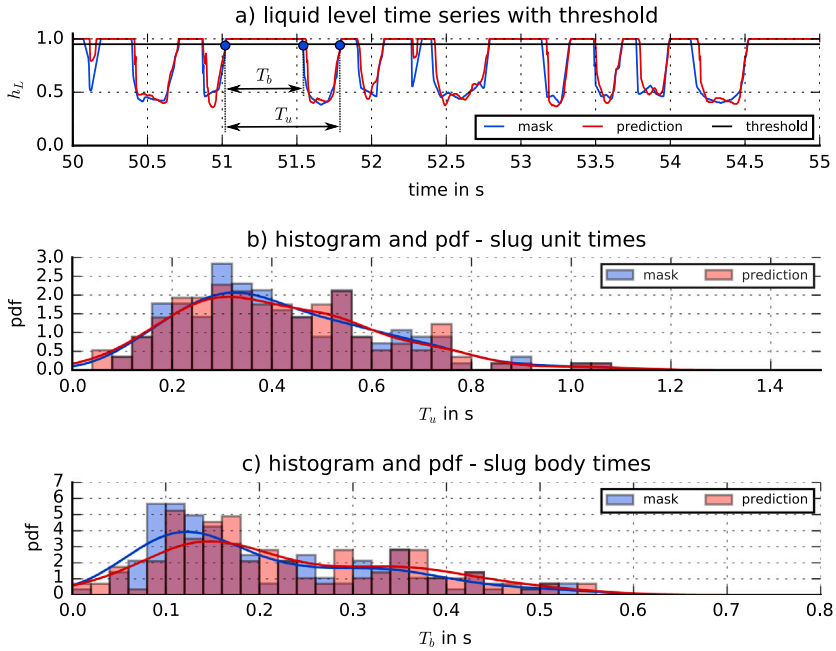

Fig. 9. The predicted and hand-labelled liquid level time series h_L^{mask} and h_L^{pred} for Experiment Nr. 12 - 100D with the threshold of 0.95 for slug detection (see a), histograms and probability density functions (pdf's) of the slug unit times T_u (see b) and slug body times T_b (see c) in comparison. Here, an illustration of the calculation of T_u and T_b is given in the time series plot (see a).

and slug rears in the time series, as illustrated in Fig. 9a. Please note that thresholding is the conventional procedure for this task, see Zhao et al. (2015), Baba et al. (2018) and Schmelter et al. (2021a), and therefore also applied in this investigation. Generally, the choice of the threshold values for the detection of slugs in the time series is not obvious and needs to be chosen individually for every time series. It should not be too high, otherwise larger slugs are separated by their entrained gas bubbles. However, it should also be chosen high enough to avoid the miscounting of large amplitude waves (Schmelter et al., 2021a). Furthermore, the histograms and probability density functions (pdf's) of the calculated slug unit times T_u and the slug body times T_b are given in Fig. 9b and c for both, the hand-labelled and predicted liquid level time series. It can be seen that the predicted time series provide similar values for T_u and T_b compared to the hand-labelled time series. This is especially the case for the slug unit times T_u with nearly identical pdf's. The histograms and pdf's for the slug body times show a slight shift to larger values for the prediction compared to the hand-labelled time series. This is caused by the later prediction of the slug rears in the predicted liquid level time series, as already discussed for Fig. 7(ii). Furthermore, the mean slug frequency $\bar{f}_s$ can directly be obtained from the mean slug unit time $\bar{T}_u$, see Eq. (1),

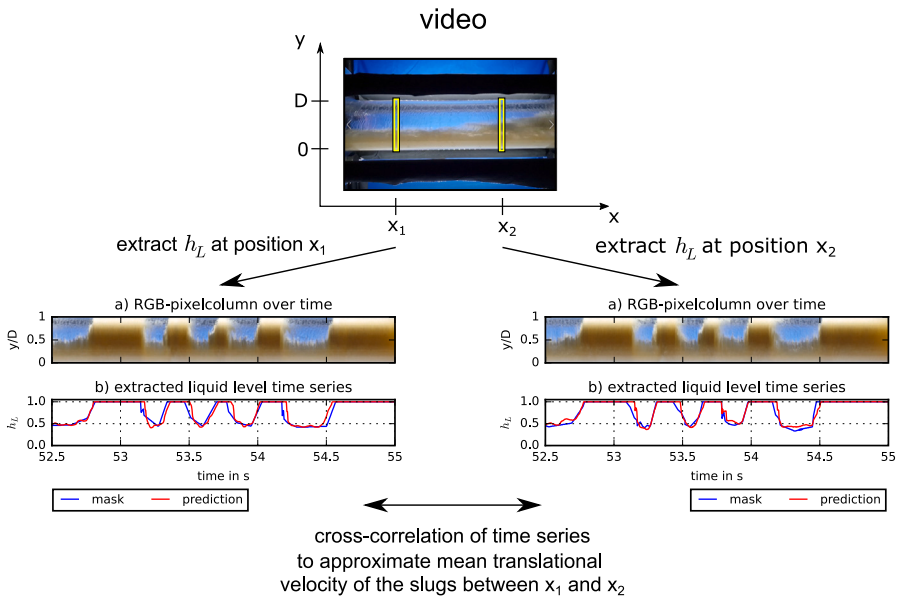

Fig. 10. Illustration of the calculation of the mean translational slug velocity $\bar{u}_{\text{slug}}$.

which is about 2.4 Hz for both time series, see also Table 9. In addition, the mean translational velocity of the slugs is calculated for the hand-labelled and predicted liquid level time series. This was achieved by a cross-correlation analysis, which is typically used to calculate the mean translational velocity and approximate the length scales L_u and L_b of the slugs from hold-up and liquid level time series, see Baba et al. (2018), Viggiano et al. (2018) and Olbrich et al. (2021a). For this, the proposed image processing technique is applied to extract the liquid level time series at two different positions x_1 and x_2 along the pipe in the video with a distance of 2.2 inner diameters D, as illustrated in Fig. 10. For the comparison, also hand-labelled liquid level time series have been considered for these positions. Then, the time lags of the time series from position x_1 and x_2 are calculated by using the cross-correlation coefficient for the time series, resulting in 8 time steps (0.033 s) for the prediction and 7 time steps (0.029 s) for the hand-labelled time series with a sample rate of 240 Hz. Then, the mean translational velocity of the slugs $\bar{u}_{\text{slug}}$ is obtained by dividing the distance between x_1 and x_2 (0.146 m) by the calculated time lag (0.033 s for the prediction and 0.029 s for the hand-labelled time series), resulting in $\bar{u}_{\text{slug}} = 4.390\,\text{m s}^{-1}$ for the prediction and $\bar{u}_{\text{slug}} = 5.017\,\text{m s}^{-1}$ for the hand-labelled time series, see also Table 9.

Moreover, the mean slug body length L_b and the mean slug unit length L_u are approximated by multiplying the corresponding mean time scales $\bar{T}_u$ and $\bar{T}_b$ with the mean translational slug velocity $\bar{u}_{\text{slug}}$. The approximated length scales for both, the prediction and the hand-labelled time series can also be found in Table 9. Altogether, the slug flow characteristics obtained by the predicted liquid level time series are in good agreement with the ones from the hand-labelled time series. This holds in particular for the temporal scales ($\bar{T}_u, \bar{T}_b, \bar{f}_s$). For the spatial scales ($\bar{L}_u$ and $\bar{L}_b$), on the other hand, slight deviations between the predicted and the hand-labelled data can be observed due to the one time step difference in the lag detected in the cross-correlation procedure. Hence, this analysis also gives insight into how much error propagation plays a role if parameters are considered that are not directly determined but calculated from other derived quantities.

The characterization of slug flow with length and time scales as well as frequency spectra of the complete liquid level time series, obtained from the results of the proposed deep learning based image processing technique have already been used in the investigation of flow experiments and validation of numerical simulations, see Schmelter et al. (2021b).

Table 9
Comparison of the mean slug characteristics calculated from the hand-labelled and predicted liquid level time series.

Parameter	Mask	Prediction
Mean slug unit time $\bar{T}_u$ in s	0.421	0.415
Mean slug body time $\bar{T}_b$ in s	0.205	0.229
Mean slug frequency $\bar{f}_s$ in Hz	2.373	2.407
Mean transl. slug vel. $\bar{u}_{\text{slug}}$ in m s^{-1}	5.017	4.390
Mean slug unit length $\bar{L}_u$ in D	31.709	27.353
Mean slug body length $\bar{L}_b$ in D	15.392	15.056

Altogether, it can be concluded that the trained model can handle different types of data and provides reliable results for its specific task. Furthermore the proposed image processing technique provides accurate liquid level time series that allow a detailed characterization of the flow.

4. Limitations

The visual recognition of gas and liquid regions or the gas–liquid interface in the video data constitutes a major limitation of the successful extraction of the liquid level time series with the proposed deep learning based image processing technique. For flows, where the interface cannot be observed from the side, a meaningful gas–liquid segmentation cannot be provided by the trained model. This is for instance the case for dispersed or annular flow patterns as well as for flows with large amounts of liquid spray, e.g., for slug or wavy flows in the transition to a dispersed or annular flow pattern. Furthermore, for foamy/bubbly regions in the flow, the segmentation often includes foam into the liquid phase, leading to overestimated absolute values for the liquid level time series. This overestimation was investigated in detail in Olbrich et al. (2021b), where hand-labelled liquid level time series of slug flow have been compared to reference parameters of a conventional tomography measurement system.

To demonstrate the limitations of a meaningful liquid level extraction with the proposed image processing technique, the method is applied to four instances of slug flow with larger amounts of dispersed phenomena, such as foam/bubbles or spray/mist. These are Experiment Nr. 8 and 14 with high liquid and low gas flow rates leading to a high liquid level in the pipe with large amounts of short slugs and foam/bubbles (see Tables. 2, 10 and Figs. 11i, 11iii) as well as Experiment

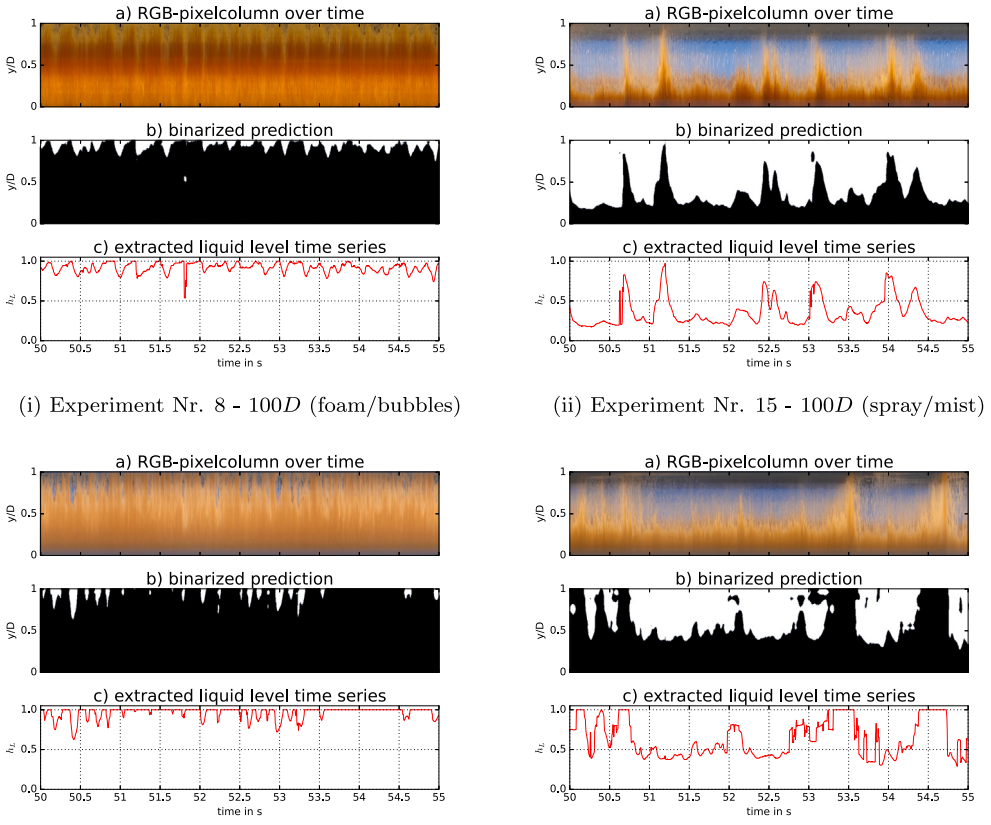

(i) Experiment Nr. 8 - 100D (foam/bubbles)

(ii) Experiment Nr. 15 - 100D (spray/mist)

(iii) Experiment Nr. 14 - 100D (foam/bubbles)

(iv) Experiment Nr. 16 - 100D (spray/mist)

Fig. 11. Visualization of the limitations of the prediction for four slug flows with large amounts of dispersed phenomena. For each experiment, the RGB-pixelcolumn over time (see a), the binarized predicted segmentation map (see b) and the extracted liquid level time series (see c) are given for the time interval [50 s, 55 s].

Table 10
The number of the experiment, the recording set-up, the recorded time (length of the video), the superficial liquid and gas velocities $v_s^{\text{liquid}}, v_s^{\text{gas}}$ (see also Table 2) and the dominant dispersed phenomena in the flow leading to an unrecognizable gas–liquid interface.

Experiment (Nr. - L_{inflow})	Set-up	Rec. time in s	v_s^{liquid} in m s^{-1}	v_s^{gas} in m s^{-1}	Dispersed phenomena
Nr. 8 - 100D	1	60	3.386	1.276	Foam/bubbles
Nr. 14 - 100D	3	60	3.911	1.548	Foam/bubbles
Nr. 15 - 100D	3	60	0.399	7.699	Spray/mist
Nr. 16 - 100D	3	60	1.209	11.442	Spray/mist

Nr. 15 and 16 with high gas and low liquid flow rates leading to a low liquid level with fewer shorter slugs and large amounts of spray/mist (see Tables. 2, 10 and Figs. 11ii, 11iv).

Due to the dispersed phenomena, the gas–liquid interface becomes (at least partially) unrecognizable for the observer in the considered image data. Thus, a meaningful hand-labelled segmentation map as ground truth for a validation of the prediction is not obtainable. However, the predictions are presented with the RGB-pixelcolumns over time in order to give an impression about the limitations of the proposed deep-learning based image processing technique.

For Experiment Nr. 8 and 15, the binarized predictions show artefacts caused by the foam/bubbles or the spray/mist, see for instance the segmented bubble in the foam/bubbles at [51.5 s, 52 s] in Fig. 11i(b) as well as the segmented lump of liquid in the spray/mist at 53 s in Fig. 11ii(b). These artefacts lead to deviations for the extraction of the liquid level time series. Despite the fact that a detailed validation with hand-labelled segmentation masks cannot be made, the extracted liquid level time series show the dominant liquid structures in the flow and can therefore be used for a quantification of the slugs in these two cases. For Experiment Nr. 14 and 16, on the other hand, with more dispersed phenomena compared to Experiment Nr. 8 and 15, the binarized predictions show larger areas of segmented liquid compared to what can visually be observed in the corresponding RGB-pixelcolumns over time (see 11iii(a,b) and 11iv(a,b)). This includes foam/bubbles or spray/mist, which are identified as liquid in the gas–liquid segmentation by the trained deep learning model, leading to impractical liquid level time series approximations.

5. Conclusions

In this paper, an image processing method based on a supervised deep learning model was presented, which extracts the liquid level time series from video recordings of liquid–gas flows in horizontal pipes. This method consists of a certain type of a deep convolutional neural network, called U-net, and several pre- and post-processing steps. The U-net was trained and tested with video data from horizontal oil–gas slug flows for the task of segmenting liquid and gas regions in the video frame data. For further evaluations of this model, additional independent video data were considered, which show different fluids, recording set-ups, and flow pattern. It was shown that, the trained model provides an accurate segmentation of oil and gas in the video data, even for previously unseen video recordings. In that regard, the model has proven to be versatile and is also applicable for other transparent gases. Furthermore, the extracted liquid level time series from the predicted segmentation maps show low errors. For the quantification of accuracy and error values, hand-labelled data was used as reference. The consistency between these hand-labelled data and the predictions of the U-net was shown in an inter-observer reliability test. Moreover, it was demonstrated how flow characteristics can be obtained from the results of the deep-learning based image processing technique.

Altogether, the presented method accurately extracts the liquid level time series from the considered video data. It can handle different types of data, even unseen data sets. Furthermore, it can overcome various noise effects, which are generally included in such image or video data. Once, the net is successfully trained, it predicts highly accurate segmentation maps in very short time. Prospectively, this method can provide parameters for the analysis and characterization of certain types of multiphase flows, in particular for the wavy or slug flow pattern, where temporal and spatial scales of the slugs, waves and bubbles, as well as their translational velocities can be derived from the extracted liquid level time series. The achieved characterization helps to assess and quantify problems for industrial operations that are induced by specific flow patterns. In addition, the proposed model has the potential for a segmentation of more complex three-phase flows, such as gas–oil–water flows with separate phases, on condition that it is trained with such data. Moreover, the proposed deep-learning based image processing technique can be used for monitoring multiphase flows for operation control if a transparent viewing section can be installed. This includes academic investigations under laboratory conditions as well as industrial applications, e.g., transportation pipelines in the oil and gas industry as well as cooling systems in the nuclear energy sector. In that regard, the link between the extracted liquid level time series and controlling parameters, such as pressure, flow rates, and phase ratio can be subject to further research.

CRediT authorship contribution statement

Marc Olbrich: Conceptualization, Methodology, Software, Investigation, Formal analysis, Validation, Visualization, Writing – original draft. **Leili Riazy:** Conceptualization, Methodology, Software, Investigation, Writing – review & editing. **Tobias Kretz:** Methodology, Software, Writing – review & editing. **Terri Leonard:** Investigation, Writing – review & editing. **Dennis S. van Putten:** Investigation, Writing – review & editing. **Markus Bär:** Supervision, Writing – review & editing. **Kilian Oberleithner:** Supervision, Writing – review & editing. **Sonja Schmelter:** Validation, Investigation, Supervision, Writing – review & editing.

Declaration of competing interest

The authors declare that they have no known competing financial interests or personal relationships that could have appeared to influence the work reported in this paper.

Data availability

The Dataset of Experiment Nr. 11 and the source code related to this article can be found at https://gitlab1.ptb.de/mfm2/liquid_level_extraction_unet, an open-source online GitLab repository hosted at Physikalisch-Technische Bundesanstalt (PTB) (Olbrich et al., 2021c).

Acknowledgements

This work was supported through the Joint Research Project *Multiphase flow reference metrology* (16ENG07). This project has received funding from the EMPIR programme co-financed by the Participating States and from the European Union's Horizon 2020 research and innovation programme.

Dataset

The Dataset of Experiment Nr. 11 and the source code related to this article can be found at https://gitlab1.ptb.de/mfm2/liquid_level_extraction_unet, an open-source online GitLab repository hosted at Physikalisch-Technische Bundesanstalt (PTB) (Olbrich et al., 2021c).

References

Abadi, M., Agarwal, A., Barham, P., Brevdo, E., Chen, Z., Citro, C., Corrado, G.S., Davis, A., Dean, J., Devin, M., Ghemawat, S., Goodfellow, I., Harp, A., Irving, G., Isard, M., Jia, Y., Jozefowicz, R., Kaiser, L., Kudlur, M., Levenberg, J., Mané, D., Monga, R., Moore, S., Murray, D., Olah, C., Schuster, M., Shlens, J., Steiner, B., Sutskever, I., Talwar, K., Tucker, P., Vanhoucke, V., Vasudevan, V., Viégas, F., Vinyals, O., Warden, P., Wattenberg, M., Wicke, M., Yu, Y., Zheng, X., 2015. TensorFlow: Large-scale machine learning on heterogeneous systems. https://www.tensorflow.org/. Accessed: 2021-05-31, Software available from tensorflow.org.

Ahmad, H., Kim, S.K., Park, J.H., Jung, S.Y., 2022. Development of two-phase flow regime map for thermally stimulated flows using deep learning and image segmentation technique. Int. J. Multiph. Flow. 146, 103869. http://dx.doi.org/10.1016/j.ijmultiphaseflow.2021.103869, URL: https://www.sciencedirect.com/science/article/pii/S0301932221002895.

Al-Kayiem, H.H., Mohmmed, A.O., Al-Hashimy, Z.I., Time, R.W., 2017. Statistical assessment of experimental observation on the slug body length and slug translational velocity in a horizontal pipe. Int. J. Heat Mass Transfer 105, 252–260.

Al-Safran, E., 2009. Investigation and prediction of slug frequency in gas/liquid horizontal pipe flow. J. Pet. Sci. Eng. 69 (1), 143–155.

Alakeely, A., Horne, R., 2021. Application of deep learning methods to estimate multiphase flow rate in producing wells using surface measurements. J. Pet. Sci. Eng. 205, 108936.

Aloysius, N., Geetha, M., 2017. A review on deep convolutional neural networks. In: 2017 International Conference on Communication and Signal Processing. ICCSP, pp. 0588–0592.

Baba, Y.D., Aliyu, A.M., Archibong, A.E., Abdulkadir, M., Lao, L., Yeung, H., 2018. Slug length for high viscosity oil-gas flow in horizontal pipes: Experiments and prediction. J. Pet. Sci. Eng. 165, 397–411.

Baghernejad, Y., Hajidavalloo, E., Hashem Zadeh, S.M., Behbahani-Nejad, M., 2019. Effect of pipe rotation on flow pattern and pressure drop of horizontal two-phase flow. Int. J. Multiph. Flow. 111, 101–111.

Bao, H., Feng, J., Dinh, N., Zhang, H., 2020. Computationally efficient CFD prediction of bubbly flow using physics-guided deep learning. Int. J. Multiph. Flow. 131, 103378.

Berman, J.J., 2016. Chapter 4 - Understanding your data. In: Berman, J.J. (Ed.), Data Simplification. Morgan Kaufmann, Boston, pp. 135–187.

Cerqueira, R.F., Paladino, E.E., 2021. Development of a deep learning-based image processing technique for bubble pattern recognition and shape reconstruction in dense bubbly flows. Chem. Eng. Sci. 230, 116163. http://dx.doi.org/10.1016/j.ces.2020.116163, URL: https://www.sciencedirect.com/science/article/pii/S0009250920306953.

Chollet, F., et al., 2015. Keras. https://keras.io. Accessed: 2021-05-31.

Crawford, D., 2018. Final Publishable JRP Report and Associated Annex A - Multiphase Flow Metrology in Oil and Gas Production (ENG58). Technical Report, EURAMET.

Dang, W., Gao, Z., Hou, L., Lv, D., Qiu, S., Chen, G., 2019. A novel deep learning framework for industrial multiphase flow characterization. IEEE Trans. Ind. Inf. 15 (11), 5954–5962.

Dhillon, A., Verma, G.K., 2020. Convolutional neural network: a review of models, methodologies and applications to object detection. Prog. Artif. Intell. 9, 85–112.

do Amaral, C., Alves, R., da Silva, M., Arruda, L., Dorini, L., Morales, R., Pipa, D., 2013. Image processing techniques for high-speed videometry in horizontal two-phase slug flows. Flow Meas. Instrum. 33, 257–264.

Dosovitskiy, A., Fischer, P., Ilg, E., Hausser, P., Hazirbas, C., Golkov, V., van der Smagt, P., Cremers, D., Brox, T., 2015. FlowNet: Learning optical flow with convolutional networks. In: Proceedings of the IEEE International Conference on Computer Vision. ICCV.

Drury, R., Hunt, A., Brusey, J., 2019. Identification of horizontal slug flow structures for application in selective cross-correlation metering. Flow Meas. Instrum. 66, 141–149.

Dukler, A.E., Fabre, J., 1994. Gas-liquid slug flow. Multiphase Sci. Technol. 8 (1–4), 355–469.

Elliott, A., Falcone, G., van Putten, D., Leonard, T., Haukalid, K., Pinguet, B., 2021. Investigating reproducibility in multiphase flow metrology: Results from an intercomparison of laboratories. Flow Meas. Instrum. 79, 101951.

Emmert-Streib, F., Yang, Z., Feng, H., Tripathi, S., Dehmer, M., 2020. An introductory review of deep learning for prediction models with big data. Front. Artif. Intell. 3, 4.

Graves, A., Mohamed, A.-r., Hinton, G., 2013. Speech recognition with deep recurrent neural networks. In: 2013 IEEE International Conference on Acoustics, Speech and Signal Processing. pp. 6645–6649.

Haas, T., Schubert, C., Eickhoff, M., Pfeifer, H., 2020. BubCNN: Bubble detection using Faster RCNN and shape regression network. Chem. Eng. Sci. 216, 115467. http://dx.doi.org/10.1016/j.ces.2019.115467, URL: https://www.sciencedirect.com/science/article/pii/S0009250919309571.

Hanratty, T.J., 2013. Physics of Gas-Liquid Flows. Cambridge University Press.

Jin, K.H., McCann, M.T., Froustey, E., Unser, M., 2017. Deep convolutional neural network for inverse problems in imaging. IEEE Trans. Image Process. 26 (9), 4509–4522.

Kamijima, C., Yoshimoto, Y., Abe, Y., Takagi, S., Kinefuchi, I., 2020. Relating the thermal properties of a micro pulsating heat pipe to the internal flow characteristics via experiments, image recognition of flow patterns and heat transfer simulations. Int. J. Heat Mass Transfer 163, 120415. http://dx.doi.org/10.1016/j.ijheatmasstransfer.2020.120415, URL: https://www.sciencedirect.com/science/article/pii/S0017931020333512.

Kingma, D.P., Ba, J., 2017. Adam: A method for stochastic optimization. arXiv:1412.6980.

Kottner, J., Dassen, T., 2008. Interpreting interrater reliability coefficients of the Braden scale: A discussion paper. Int. J. Nurs. Stud. 45 (8), 1238–1246.

Krizhevsky, A., Sutskever, I., Hinton, G.E., 2017. ImageNet classification with deep convolutional neural networks. Commun. ACM 60 (6), 84–90.

Larsen, R.J., Marx, M.L., 2012. Introduction to Mathematical Statistics and Its Applications, 5th Edition, Vol. 5. Prentice Hall.

LeCun, Y., Bengio, Y., Hinton, G., 2015. Deep learning. Nature 521 (7553), 436–444.

Li, J., Hu, D., Chen, W., Li, Y., Zhang, M., Peng, L., 2021. CNN-based volume flow rate prediction of oil–gas–water three-phase intermittent flow from multiple sensors. Sensors 21 (4), 1245.

Lin, Z., Liu, X., Lao, L., Liu, H., 2020. Prediction of two-phase flow patterns in upward inclined pipes via deep learning. Energy 210, 118541.

Ma, M., Lu, J., Tryggvason, G., 2015. Using statistical learning to close two-fluid multiphase flow equations for a simple bubbly system. Phys. Fluids 27 (9), 092101.

Mao, X.-J., Shen, C., Yang, Y.-B., 2016. Image restoration using very deep convolutional encoder-decoder networks with symmetric skip connections. In: Proceedings of the 30th International Conference on Neural Information Processing Systems. NIPS '16, Curran Associates Inc., Red Hook, NY, USA, pp. 2810–2818.

Mohmmed, A.O., Al-Kayiem, H.H., Nasif, M.S., Time, R.W., 2019. Effect of slug flow frequency on the mechanical stress behavior of pipelines. Int. J. Press. Vessels Pip. 172, 1–9.

Olbrich, M., Bär, M., Oberleithner, K., Schmelter, S., 2021a. Statistical characterization of horizontal slug flow using snapshot proper orthogonal decomposition. Int. J. Multiph. Flow. 134, 103453.

Olbrich, M., Hunt, A., Leonard, T., van Putten, D.S., Bär, M., Oberleithner, K., Schmelter, S., 2021b. Comparing temporal characteristics of slug flow from tomography measurements and video observations. Meas.: Sensors 18, 100222.

Olbrich, M., Riazy, L., Kretz, T., Schmelter, S., 2021c. Liquid-gas interface selection algorithm (LISA) with unet. https://gitlab1.ptb.de/mfm2/liquid_level_extraction_unet.

Olbrich, M., Schmeyer, E., Bär, M., Sieber, M., Oberleithner, K., Schmelter, S., 2020. Identification of coherent structures in horizontal slug flow. Flow Meas. Instrum. 76, 101814.

Olbrich, M., Schmeyer, E., Riazy, L., Oberleithner, K., Bär, M., Schmelter, S., 2018. Validation of simulations in multiphase flow metrology by comparison with experimental video observations. J. Phys. Conf. Ser. 1065, 092015.

Pedersen, S., Durdevic, P., Yang, Z., 2017. Challenges in slug modeling and control for offshore oil and gas productions: A review study. Int. J. Multiph. Flow. 88, 270–284.

Pieper, A., 2020. Final Publishable Report - Multiphase Flow Reference Metrology (16ENG07). Technical Report, EURAMET.

Poletaev, I., Tokarev, M.P., Pervunin, K.S., 2020. Bubble patterns recognition using neural networks: Application to the analysis of a two-phase bubbly jet. Int. J. Multiph. Flow. 126, 103194.

Prechelt, L., 1998. Early stopping - but when? In: Orr, G.B., Müller, K.-R. (Eds.), Neural Networks: Tricks of the Trade. Springer Berlin Heidelberg, Berlin, Heidelberg, pp. 55–69.

Ronneberger, O., Fischer, P., Brox, T., 2015. U-Net: Convolutional networks for biomedical image segmentation. In: Navab, N., Hornegger, J., Wells, W.M., Frangi, A.F. (Eds.), Medical Image Computing and Computer-Assisted Intervention – MICCAI 2015. Springer International Publishing, Cham, pp. 234–241.

Schmelter, S., Knotek, S., Olbrich, M., Fiebach, A., Bär, M., 2021a. On the influence of inlet perturbations on slug dynamics in horizontal multiphase flow—a computational study. Metrologia 58 (1), 014003.

Schmelter, S., Olbrich, M., Knotek, S., Bär, M., 2021b. Analysis of multiphase flow simulations and comparison with high-speed video observations. Meas.: Sensors 18, 100154. http://dx.doi.org/10.1016/j.measen.2021.100154, URL: https://www.sciencedirect.com/science/article/pii/S2665917421001173.

Sterbak, T., 2018. U-Net for segmenting seismic images with keras. https://www.depends-on-the-definition.com/unet-keras-segmenting-images. Accessed: 2021-05-25.

Taitel, Y., Dukler, A., 1977. A model for slug frequency during gas-liquid flow in horizontal and near horizontal pipes. Int. J. Multiph. Flow. 3 (6), 585–596.

Tinsley, H.E., Weiss, D.J., 1975. Interrater reliability and agreement of subjective judgments. J. Couns. Psychol. 22 (4), 358–376.

Viggiano, B., Skjæraasen, O., Schümann, H., Tutkun, M., Cal, R.B., 2018. Characterization of flow dynamics and reduced-order description of experimental two-phase pipe flow. Int. J. Multiph. Flow. 105, 91–101. http://dx.doi.org/10.1016/j.ijmultiphaseflow.2018.03.020, URL: https://www.sciencedirect.com/science/article/pii/S0301932217309941.

Virtanen, P., Gommers, R., Oliphant, T.E., Haberland, M., Reddy, T., Cournapeau, D., Burovski, E., Peterson, P., Weckesser, W., Bright, J., van der Walt, S.J., Brett, M., Wilson, J., Millman, K.J., Mayorov, N., Nelson, A.R.J., Jones, E., Kern, R., Larson, E., Carey, C.J., Polat, İ., Feng, Y., Moore, E.W., VanderPlas, J., Laxalde, D., Perktold, J., Cimrman, R., Henriksen, I., Quintero, E.A., Harris, C.R., Archibald, A.M., Ribeiro, A.H., Pedregosa, F., van Mulbregt, P., SciPy 1.0 Contributors, 2020. SciPy 1.0: Fundamental algorithms for scientific computing in Python. Nature Methods 17, 261–272.

Walburn, F.J., Sabbah, H.N., Stein, P.D., 1983. An experimental evaluation of the use of an ensemble average for the calculation of turbulence in pulsatile flow. Ann. Biomed. Eng. 11 (5), 385–399.

Wang, Y., Lin, G., 2020. Efficient deep learning techniques for multiphase flow simulation in heterogeneous porousc media. J. Comput. Phys. 401, 108968.

Xiao, S., Bucher, F., Wu, Y., Rokem, A., Lee, C.S., Marra, K.V., Fallon, R., Diaz-Aguilar, S., Aguilar, E., Friedlander, M., Lee, A.Y., 2017. Fully automated, deep learning segmentation of oxygen-induced retinopathy images. JCI Insight 2 (24).

Yan, Y., Wang, L., Wang, T., Wang, X., Hu, Y., Duan, Q., 2018. Application of soft computing techniques to multiphase flow measurement: A review. Flow Meas. Instrum. 60, 30–43.

Yu, C., Luo, H., Bi, X., Fan, Y., He, M., 2021. An effective convolutional neural network for liquid phase extraction in two-phase flow PIV experiment of an object entering water. Ocean Eng. 237, 109502. http://dx.doi.org/10.1016/j.oceaneng.2021.109502, URL: https://www.sciencedirect.com/science/article/pii/S0029801821009021.

Zhao, Y., Lao, L., Yeung, H., 2015. Investigation and prediction of slug flow characteristics in highly viscous liquid and gas flows in horizontal pipes. Chem. Eng. Res. Des. 102, 124–137. http://dx.doi.org/10.1016/j.cherd.2015.06.002, URL: https://www.sciencedirect.com/science/article/pii/S0263876215002075.

3

Discussion

3.1 The quantification of horizontal slug flow with snapshot Proper Orthogonal Decomposition

The conventional procedures for the quantification for horizontal slug flow are focusing either on a temporal description of the flow or a spatial description of the slugs. For the temporal quantification of slug flow, this includes time series analysis of phase volume fraction [40] and liquid level measurements [36], slug triggering mechanisms [63] as well as manually counting slugs [67]. Typically, these analyses are performed on data sets, which provide information about the dynamics of the phase distribution at a certain position in the pipe, but do not contain necessary spatial information about the slugs, for instance cross-sectional measurements [54] or single local wire-sensor [56]. To extrapolate spatial information of the slugs from these data, additional parameters, such as the translational slug velocities, need to be measured in advance [50]. For the measurement of spatial information of the slugs on the other hand, image processing techniques are usually employed on image or video data of the slugs [64]. Although video data contain temporal information too, the reported spatial analyses of slugs have not yet focused on the flow dynamics. In this context, a novel approach for a robust temporal and spatial quantification of horizontal slug flow with snapshot POD is presented, which uses spatio-temporal data sets, such as raw video data or snapshot sequences of phase fraction fields.

The snapshot POD is a modal decomposition, which extracts an energy-ranked mode basis of the coherent structures from the flow data [68, 69]. It is the most widely used POD method in fluid mechanics [69] and often employed for the identification and characterization of coherent structures in singlephase turbulent flows [72, 71, 75, 69]. For multiphase flows, however, there are only a few references on POD. In [85, 86, 87, 88], POD was used to identify coherent turbulent structures, such as eddies, in gas-liquid flows. In these investigations, the method was typically applied to velocity data from PIV-measurements. In [82, 83, 84, 89], POD was used for reduced order modelling with the aim of recognizing different flow patterns as well as the transition between them. In this context, the analyses were usually performed

on cross-sectional measurements of the phase distribution in the pipe. Measured flow data were approximated by a reduced order model based on a small number of POD modes, which capture the dominant behavior of the flow pattern. In [89], POD was applied to cross sectional tomography measurements of horizontal slug flow. They found a strong correlation between the temporal coefficient of one of the dominant POD modes and the liquid holdup in the pipe. From that, a timescale was derived to characterize the slugs. In summary, POD was used to find a low order description of large and complex multiphase flow data sets, to investigate turbulent structures in two-phase flows, and to characterize horizontal slug flow in time.

In this thesis, not only a temporal, but also a spatial characterization of horizontal gas-liquid slug flow with snapshot POD is presented. For the considered data sets, the characterization of slug flow is derived from the most dominant POD-mode pair and the corresponding temporal coefficients. These POD-analyses are performed on phase fraction fields from a longitudinal section along the vertical centerline of the pipe, as well as high speed video recordings of the slug flow from the side, see Section 1.4 or Section 3 in Publication I (2.2) and Section 3 and 4 in Publication II (2.2). In the first step, an operationally induced slug flow is analyzed, which consists only of periodically formed slugs that appear with the exact frequency of 1 Hz at the point of observation, see Section 1.4 or Section 3 in Publication I (2.2) and Section 3 and 4 in Publication II (2.2). Hence, the slugs constitute a periodic structure in the data set. Since the dynamics of periodic structures can be described by a pair of POD-modes, the mode-coupling algorithm proposed by Sieber et al. in [68] is applied a-posteriori to the temporal coefficients of the calculated POD-modes. In this algorithm, related modes are identified by the spectral similarity of their temporal coefficients, which is measured by using the so-called *harmonic correlation* from [68], see Equation (9) in Publication II (2.2). This measure provides a quantification of the spectral proximity of the individual modes and allows a coupling of the modes also for flows with more complex dynamics [68]. Thus, the mode coupling algorithm is also applied for the POD-analysis of the considered non-periodic slug flows. Generally, this technique helps to condense information about the individual coherent structures in the flow, which are provided by the snapshot Proper Orthogonal Decomposition. This is of particular interest in the context of this thesis since a characterization of specific structures, namely slugs, is desired.

For the investigation of this novel approach for the quantification of horizontal slug flow with snapshot POD, three aspects are addressed. These are the representation of the slugs in the POD modes, the derivation of the spatial and temporal characteristics of slug flow from the POD-modes, and the data requirements for this application.

3.1.1 Representation of the slugs in the POD modes

In the investigations for the quantification of horizontal slug flow by using snapshot POD, it was shown in Publication I and II that, the slugs of the considered horizontal slug flows are represented in the most dominant mode pair of a snapshot-POD analysis. This includes a strong similarity between the (ensemble) averaged slug and the liquid structure in the spatial modes as well as a strong similarity between the standardized liquid level time series and the standardized temporal coefficients of the most dominant mode pair. These similarities are illustrated for one of the two modes from the most dominant mode pair in Figure 3.1 for two

instances of slug flow, i.e., an air-water slug flow from the numerical simulation and a gas-oil slug flow from an experiment. For details, see Publication II (Section 2.2).

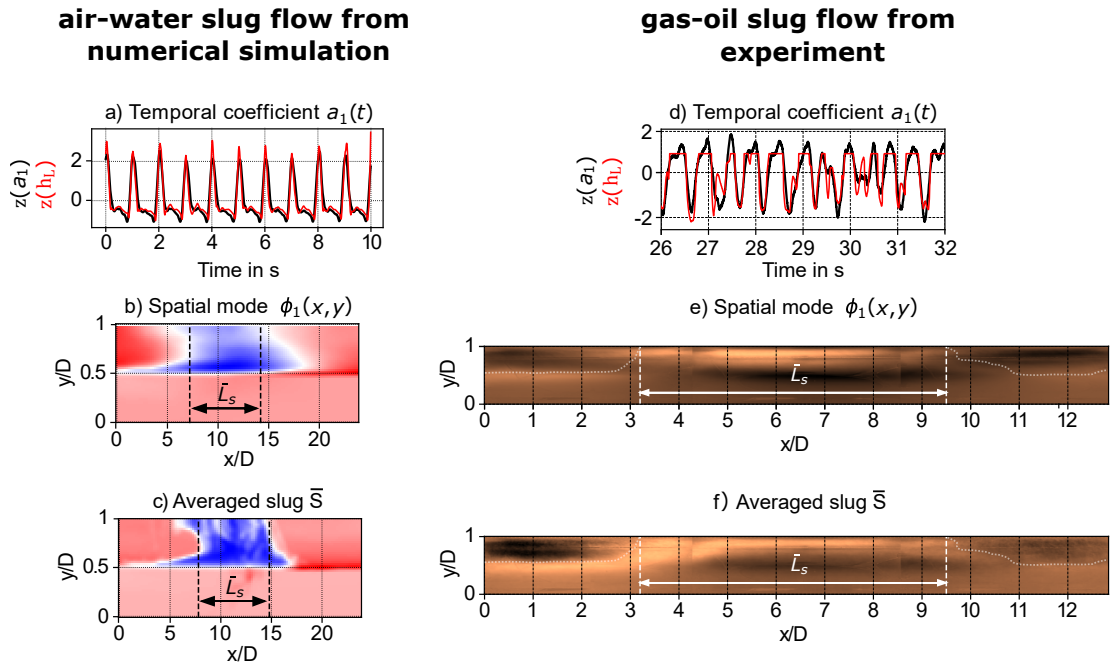

Figure 3.1: Illustration of the spatial modes ϕ_1 (see b and e) and their temporal coefficients a_1 in z-score (see black line in a and d) from the most dominant mode pair of a snapshot POD-analysis in comparison with corresponding liquid level time series h_L in z-score (see red line in a and d) and the (ensemble) averaged slugs $\bar{S}$ (see c and f) for an air-water slug flow from a numerical simulation (phase fraction fields) and a gas-oil slug flow from an experiment (video recordings). For reasons of clarity, the interface from the averaged slug is highlighted in f and superimposed over the spatial modes in e). In addition, the mean slug body lengths $\bar{L}_s$ are indicated. For details see Publication II in Section 2.2

The representation of the slugs in the POD-modes is further discussed in the following.

3.1.1.1 Spatial Modes

It was found for the considered data sets that, the (ensemble) averaged slug is represented in the spatial modes of the dominant POD-mode pair. This was concluded from a detailed comparison of the spatial modes with the (ensemble) averaged slug, including visual comparison as well as a quantitative comparison of the derived length scales. Moreover, for the high-quality phase fraction fields from the simulated air-water slug flow, a detailed correlation analysis of the spatial mode and the averaged slug was conducted in addition to determine the similarity between these structures. In the context of image processing, the normalized 2-dimensional cross-correlation coefficient is a common similarity measure for images and often used in template matching tasks [104].

For the comparison with the averaged slug, the one out of two spatial modes of the mode pair was considered, for which the liquid structure was visible to its full extend. Generally, the two spatial modes of the most energetic mode pair show the same structure, but are shifted to each other. This can be concluded from the coupling procedure of the POD-modes and the calculation of the spatial modes from the corresponding temporal coefficients. In the mode coupling algorithm, related modes are identified by the spectral similarity of their

temporal coefficients, which accounts for modes that have similar, but shifted dynamics. Thus, the temporal coefficients of the coupled modes show similar patterns and behavior, but they are shifted to each other. Since the spatial modes are calculated as the weighted average of the fluctuations of the snapshots, where the weights are given by the values of the temporal coefficients and the corresponding eigenvalues (see Equation (1.5)), the spatial modes are also shifted in the same manner. Due to this shift, the structure shown in the spatial modes, is not necessarily visible to its full extend in both of the modes, even if the length of the observed pipe segment (region of interest) is large enough to resolve the entire structure. However, in the course of these investigations, the averaged slug was typically visible in one of the two spatial modes of the most energetic mode pair for the considered data sets with a sufficiently long pipe segment.

Another aspect in the comparison of the (ensemble) averaged slug with the structure in the spatial modes is their position in the considered pipe segment. This needs to be taken into account to avoid undesired differences in slug shape and length, which can be caused for instance by slug growth. Hence, the structure in the spatial modes dictate the position for the comparison and the (ensemble) averaged slug needs to be calculated at this position.

3.1.1.2 Temporal Coefficients

Apart from the spatial modes, it was also found for the considered data sets that, the dynamics of the liquid level time series are represented in the temporal coefficients of the dominant POD-mode pair. In detail, the standard score of the liquid level time series coincides with the standard score of the temporal coefficients. This was concluded from a detailed comparison of the temporal coefficients with the liquid level time series in standard score, including visual comparison, quantitative comparison of the derived time scales, as well as an error analysis. Therefore, the temporal coefficients describe the temporal features of slug flow. Since the snapshot POD provides a mode basis for the data set, the individual basis elements do generally not have values that are in the same range as the variable, which has been decomposed. Due to that, the temporal coefficients and the spatial modes represent the temporal or spatial variations, but they do not attain the absolute values of the parameters, such as liquid level time series or the phase distribution for the (ensemble) averaged slug, respectively. For this reason, the liquid level time series and the temporal coefficients have been compared in standard score and the spatial modes have been normalized accordingly.

In the course of these investigations, the liquid level time series have been extracted from the vertical centerline of the pipe or approximated from video observations from the side, at a fixed streamwise position in the observed pipe segment. In order to avoid undesired deviations in the comparison of the temporal coefficient with the liquid level time series, this streamwise position needs to be taken into account. In this context, it was found for the considered data sets that, the standardized temporal coefficient approximates best the standardized liquid level time series, which has been extracted at the streamwise position, where the liquid intensity in the corresponding spatial mode is maximal. Typically, the position was located in the middle of the liquid structure (averaged slug) shown in the spatial mode.

Generally, the most energetic POD-modes represent the most dominant structures of the flow in terms of their fluctuations in the data. Thus, for more complex types of slug flow, such

as flows consisting of slugs and larger waves, the mode pair does not exclusively represent the slugs in the flow, but also other larger structures, e.g., the larger waves. This can be seen in the temporal coefficients, which reveal the dynamics of the gas-liquid interface at a certain position, especially for larger structures (see Figure 3.1d). Thus, the larger waves are also represented in the spatial modes, which are calculated with the temporal coefficients. However, from a phenomenological point of view, the large amplitude waves in between the slugs are typically shorter (in their length) compared to the slugs, and become less for further developed slug flows. Hence, the slug remains the prominent structure visible in the spatial mode. On the other hand, for the considered types of slug flow data, the slugs and large amplitude waves constitute the most dominant fluctuations in the data set. Due to that, it is reasonable for these dominant structures to be represented by the most dominant mode pair with the largest eigenvalues-ratio.

Altogether, the scientific result presented in Publication I and II (see Section 2.1 and 2.2) are leading to the conclusion that, the slugs are represented in the dominant mode pair of a snapshot POD-analysis for the considered slug flow data sets. These results include a description of the gas-liquid interface dynamics (approximation of the dynamics of the liquid level time series) in the temporal coefficients as well as the representation of the averaged slug in the spatial modes. This allows a detailed characterization of the temporal features of the flow as well as a statistical characterization of the spatial features of the slug. In this context, the derivation of time and length scales for the characterization of slug flow are discussed in the following section.

3.1.2 Derivation of time and length scales from the POD modes for the characterization of slug flow

In Publication I and II, different approaches for the derivation of the characterizing time and length scales for slug flow from the most dominant mode pair of a POD analysis have been considered, and further investigations on the accuracy of these length and time scales have been conducted. As discussed in the previous section, both temporal coefficients from the most energetic mode pair represent the dynamics of the vertical position of the gas-liquid interface from the considered data sets. However, it was observed that one of the two standardized temporal coefficients approximates the standardized liquid level time series more accurate. Typically, for this temporal coefficient, the averaged slug structure was more distinctly recognizable in the corresponding spatial mode. In detail, this means that the entire slug structure was typically visible to its full extend for observed pipe segments (regions of interest), which are large enough to resolve it. On the other hand, for observed pipe segments (region of interests), that are shorter, the spatial mode appeared to be completely filled with liquid, which indicates the averaged slug structure, but did not show it to its full extend. This spatial mode and the corresponding temporal coefficient was further considered for the derivation of the characterizing time and length scales of slug flow, see for instance Figure 3.1. In the following, this derivation of the time and length scales is further discussed.

3.1.2.1 Conventional length and time scales of slug flow

An approximation of the averaged slug body length $\bar{L}_s$ can directly be obtained from the representation of the averaged slug in the spatial mode, see Figure 3.1. Moreover, the characterizing time scales of slug flow, such as slug unit times T_u or slug body times T_b, can be derived from the temporal coefficient. Then, the mean slug frequency can be calculated from T_u as given in Equation (1.1). Typically, for analyses of holdup time series, these quantities are calculated by simple thresholding procedures, see [105, 50]. Although, thresholding is error-prone, it is the conventional procedure for this task and therefore also applied in these investigations. Generally, the choice of the threshold values for the slug detection in the time series is not obvious. In particular for the temporal coefficient, which has a different range compared to the typical quantities, such as liquid level or holdup. In a first approach in Publication I (see Section 2.1), the threshold value has been chosen generically as 0 for the time series in standard score, which led to an estimate of the mean time of the entire slug structure passing by, instead of a reasonable approximation of the slug body time. Consequently, an appropriate choice of a threshold value for the time scale detection needs further considerations. It must be noticed that, the threshold value needs to be chosen individually for every time series. Furthermore, it should not be too high, otherwise larger slugs are separated by their entrained gas bubbles. However, it should also be chosen high enough to avoid the detection of large amplitude waves [106]. Based on this, the threshold procedure was adapted accordingly for the individual time series in the more detailed analyses in Publication II (see Section 2.2) with the aim of accurately calculating the slug body times.

3.1.2.2 Dominant frequency and eigenvalues of the POD-modes

The dominant frequency $f_{i,j}$ of the mode pair (a_i, a_j) is provided by the mode coupling algorithm, see Equation (10) in Publication II (Section 2.2). This parameter represents a mean dominant frequency of the corresponding time series given by the temporal coefficients (a_i, a_j). For the dominant mode pair of the considered slug flows, this frequency provides an approximation of the dominant frequency of the liquid level time series h_L, since the temporal coefficients of the mode pair approximate h_L. Thus, it can be used as an additional quantity for the characterization of the flow. In this context however, the dominant frequency $f_{i,j}$ of the most dominant mode pair (a_i, a_j) is generally not equal to the mean slug frequency $\bar{f}_s$, which is defined as the inverse mean time in between consecutive slugs, see Equation (1.1). But for certain types of slug flow, such as the periodic air-water slug flow considered in Publication I and II (Section 2.1 and 2.2), these frequencies can coincide.

In addition, the snapshot-POD algorithm also provides the eigenvalues λ_i of the modes, see Equation (1.3). In general, this parameter represents a measure for the proportion of the fluctuations from the data set that is captured by the corresponding eigenvector, or rather the corresponding temporal coefficient, and is often referred to as an energy representation. For input variables with physical units, this parameter can indeed be identified with a physical energy, for instance a representation of the turbulent kinetic energy for velocity fields [72]. In contrast, such an identification with a physical energy can not be made for the considered slug flow data with arbitrary units, such as phase fraction fields and RGB-pixel values. These eigenvalues are often used as a characterizing quantity for the coherent structure, described by

the corresponding modes or mode pairs, in particular for the comparison of flows under different operating conditions, see for instance [75]. It also has significance in the reduced order modeling of flow data, where it constitutes a key parameter for choosing the number of basis vectors, which forms the reduced order model, see [76]. However, for a conventional characterization of slug flow with its time and length scales, this parameter is of minor importance. Nevertheless, it can contribute to a quantitative comparison of different slug flows or data sets.

3.1.2.3 Influence of the field length

In Publication II (see Section 2.2) it was found that, the length of the observed pipe segment (field or region of interest) affects the accuracy by which the temporal coefficient approximates the corresponding liquid level time series. This relation is a result from a detailed error analysis based on the high-quality phase-fraction data of the simulated air-water slug flows, but was also observed for the experimental data. For this, the mean relative error of the standardized temporal coefficient and the standardized liquid level time series have been investigated for independently conducted snapshot POD analyses of data from 38 differently long regions of interest, reaching from 1 inner pipe diameter to 74 inner pipe diameters, see Figure 9 and 10 in Publication II. Different reasons for the described negative trend in accuracy for the increasing length of the region of interest have been identified in Publication II. On one hand, the calculation of the temporal coefficient from the temporal covariance matrix of the phase volume fraction fields (see Equation (1.3)) are contributing to this error behavior. In detail, due to the summation over the spatial components of the fluctuations of the snapshots (dot product) in the POD algorithm, small structures, such as single slugs, are underrepresented in larger regions of interest, where also other fluctuations are taken into account. Furthermore, the scalar representation from the dot product of neighboring snapshots, where the same structure is at slightly different positions, become more similar for larger regions of interest. This leads to a broader temporal correlation, and results in a smoother temporal coefficient with wider spikes of lower amplitude (Figure 11 in Publication II). Hence, the representation of the slugs in the temporal coefficient becomes more imprecise for longer regions of interest relative to the detailed liquid level time series h_L. Another reason for this negative trend is that, the slugs accelerate and change shape as they move downstream the pipe. For longer regions of interest, this phenomenon is also having more influence on the computation of a_i and ϕ_i and causes negative effects on the approximation of the liquid level time series by the temporal coefficient. Consequently, this behavior affects also the accuracy of the derived time scales in the same manner, in particular the slug body times. It can also be concluded, that the most accurate approximations of the liquid level time series by the temporal coefficient are achieved for the shortest regions of interest. This is also in line with the results of Vigiano et al. [89], where a strong correlation of the holdup time series and the temporal coefficient of a dominant mode from a snapshot POD analysis of cross-sectional phase fraction measurements of horizontal slug flow was reported, since the cross-sectional data does not resolve spatial information of the slugs in the longitudinal direction.

For the representation of the averaged slug in the spatial mode, a similar negative trend in accuracy has been noted for increasing length of the region of interest, see Figure 10 in Publication II (Section 2.2). This can be explained by the calculation of the spatial mode ϕ_i

as the weighted average of the fluctuations of the snapshots, where the weights are given by the values of the temporal coefficient a_i and the corresponding eigenvalue λ_i (see Equation 1.5). Thus, the error in the temporal representation of the slugs in a_i, i.e., wider spikes with lower amplitude, propagates in their spatial representation in ϕ_i. In detail, the broader and more inaccurate the spikes in the temporal coefficient, the more weight is put on snapshots with slugs in slightly shifted positions for the calculation of ϕ_i. Thus, the averaged slug visible in ϕ_i appears to be blurred for longer regions of interest. This causes inaccuracies in the derivation of the mean slug body length from the spatial mode.

Altogether, it was presented for the considered data sets in Publication I and II (Section 2.1 and 2.2), that the conventional length and time scales for the characterization of horizontal slug flow can be derived from the most dominant mode pair of a snapshot POD analysis. Moreover, for a meaningful spatio-temporal characterization of slug flow with this length and time scale derived from the most dominant mode pair, the region of interest should have the necessary length to resolve the averaged slug entirely, but should remain sufficiently short to avoid larger errors in the characterizing parameters. If only a characterization in time is sought, the region of interest should be chosen as short as possible.

In order to derive a reasonable characterization of horizontal slug flow from the most dominant mode of a snapshot POD analysis, the data should meet certain requirements. These are discussed in the following.

3.1.3 Data requirements for the characterization of slug flow with snapshot POD

In the investigations concerning the quantification of horizontal slug flow with snapshot POD in Publication I and II, different types of data have been analyzed. These data sets satisfy certain criteria, which are substantial for the presented characterization of slug flow with snapshot POD. Those requirements are discussed in the following.

The first requirement is the representation of the spatial phase distribution with its temporal changes in the data. In general, multiphase flow patterns, such as horizontal gas-liquid slug flow, are defined by the spatio-temporal distribution of the different phases in the observed pipe segment. Thus, for a quantification of the slug flow pattern, the considered data should provide a description of this spatio-temporal phase distribution. Furthermore, the snapshot POD algorithm is based on the temporal correlation of spatially averaged snapshots (see the calculation of the temporal co-variance matrix $R \in \mathbb{R}^{N \times N}$ in Publication II (Section 2.2)). For snapshots, that provide spatial information of the phase distribution of slug flow, this averaging process leads to a reasonable description of the liquid structures in the snapshot, i.e., the fraction of the investigated phase in the corresponding snapshot.

For a temporal and spatial quantification of horizontal slug flow with snapshot POD, the second requirement is the spatial representation of the slugs in the data, in particular their length. Since slugs are liquid structures of different lengths, which block the complete pipe cross-section with liquid, the data should capture the spatial information in the pipe along the vertical axis from bottom to top, as well as along the longitudinal axis, in order to resolve the slugs in their vertical and longitudinal dimensions. In detail, for a meaningful spatio-temporal characterization of slug flow with snapshot POD, the region of interest should

have the necessary length to resolve the averaged slug entirely, but should remain sufficiently short to avoid larger errors in the characterizing parameters, as discussed in Section 3.1.2. This requirement changes if only a characterization in time is sought. Then, the region of interest should be chosen as short as possible, such that the data represents at best the phase distribution along a vertical line in the pipe, from bottom to top, as pointed out in Section 3.1.2.

For these reasons, data sets that represent the phase distribution in a two-dimensional plane along the vertical and longitudinal axis of an observed pipe segment have been considered in this work. This includes two-dimensional volume fraction fields in a longitudinal section along the vertical centerline of the observed pipe segment for the simulated air-water slug flow (see also Section 1.4) as well as two-dimensional scalar fields of RGB-components from a video recording of the flow from the side for an gas-water and gas-oil slug flow (see also Section 1.4). For the gas-oil slug flow, it was possible to describe the phase distribution in the observed pipe segment by considering the red component of the RGB-values, due to the reddish-brown color of the oil, the transparent gas and the dark background in the recording setup (see Publication II in Section 2.2). For the gas-water slug flow, the grayscale of the RGB-values was considered, because of the gray color of the water in the videos (see Publication I in Section 2.1).

The phase fraction data of the air-water slug flow from the numerical simulation was available for the complete length of the computational domain, i.e., the 8 m long pipe, such that the spatial resolution of the slugs in the considered two-dimensional plane was ensured. In contrast to this, the experimental set-ups consist of permanently installed transparent viewing sections with a fixed length of approximately 0.5 m. For the considered slug flow experiments, this viewing sections were too short to resolve the averaged slugs entirely, see for instance Publication I in Section 2.1. Thus, the slug body lengths could not be derived from the spatial modes in the first place. To enable also a direct spatial characterization of the slugs from the spatial mode, an artificial extension procedure for the region of interest based on cross correlation was developed and applied to the raw video data of the gas-oil slug flow experiment, as presented in Publication II (Section 2.2). The extension of the region of interest was done by embedding the frames into time-shifted frames from the same video. For slug flows, where the slugs have similar translational velocities and the changes in their properties, such as velocity and shape, are negligible within the viewing section, this embedding can be applied to enlarge the region of interest without a distortion of the slugs, for details see Publication II in Section 2.2. It was applied to the video data of the gas-oil slug flow experiment in order to extend the region of interest and resolve the entire averaged slug. This procedure provided data with sufficient spatial information of the slugs, and hence, made their direct spatial characterization with snapshot POD possible, see Publication II in Section 2.2.

Altogether, for a meaningful temporal and spatial characterization of horizontal slug flow with snapshot POD, the data should represent the phase distribution with its temporal changes in a pipe segment, which is long enough to resolve the desired spatial information of the slugs. Three different data sets have been considered for the investigations for the quantification of horizontal slug flow with snapshot POD, which belong to two common types of data in the industrial and academic field of multiphase flows. The first type is high quality data from numerical simulations, which are a proven tool for the investigation of fluid flows. The second

type is RGB-data of noise-affected experimental video recordings, which are a common for experimental investigations of two-phase flow patterns, especially in the academic field. For these two types of data, the novel concept of the quantification of horizontal slug with snapshot POD was proven.

In the course of these investigations, an approximation of the liquid level time series as well as time scales of slug flow have been derived from video recordings. Although video-based approaches are common for the investigations of slug flows, in particular to examine geometrical properties of the slugs and bubbles, an approximation of the liquid level time series and a derivation of the time scales of the slugs from video observations was not reported in the literature. For this reason, the plausibility of the temporal quantification of slug flow from video observations needs to be investigated. In this regard, the approximation of the liquid level time series as well as time scales of slug flow from video recording are further examined and discussed in the next section.

3.2 The evaluation of the temporal quantification of slug flow from video observations by using tomography measurements as a reference

The liquid level time series describes the dynamic behavior of the interface of horizontal gas-liquid flows in a certain plane, commonly in the vertical centerline of the pipe for a fixed longitudinal position, see Figure 1.3. Therefore, it also represents the dynamics of the phase distribution and thereby provides a temporal quantification of separated and intermittent flow pattern. The conventional measurement techniques of the liquid level time series for horizontal stratified and slug flows include intrusive wire-sensor measurements in the vertical centerline of the pipe [36, 56, 57] as well as non-intrusive narrow-beam gamma densiometer measurements in the pipe cross-section [60]. For the approximation of the liquid level time series with image processing techniques, only very few references can be found. In [107], an image processing technique is presented, where the gas-liquid interface is detected in the grayscale image of each video frame from recordings of air-water stratified and wavy flows. From that, also a liquid level time series was derived to investigate the liquid film thickness in stratified flows. In [108], an image processing technique is presented, where the gas-liquid interface is detected in a binarization of each video frame from recordings of air-water stratified and slug flows. For their analysis of the transition from stratified flow to slug flow, time series of mean values of the liquid film thickness over the complete length of the observed pipe segment have been considered. However, an approximation of the liquid level time series from video recordings of horizontal slug flow was not reported in the literature, except in the author's earlier work [62]. In that paper, an image processing technique based on a fixed sequence of image filters is presented that extracts an approximation of the liquid level time series. However, this approach is only applicable to certain types of gas-oil and gas-water slug flows, which have been recorded under specific conditions. This technique was used in the investigations of Publication I (Section 2.1) to extract an approximation of the liquid level time series from the raw video data as a reference parameter for the temporal coefficient of the snapshot POD analysis, as discussed in Section 3.1.1. However, for the video recordings of the oil-gas slug

flow in Publication II (Section 2.2), the approximation of the liquid level time series with this technique was not successful. Thus, the liquid level time series has been derived from manually marked gas-liquid interfaces in the video data, as described in Publication II in Section 2.2. All of the aforementioned approximations of the liquid level time series from video recordings have not been validated with other conventional measurement techniques. For this reason, the validity of the derived time scales of slug flow needs to be proven.

In this context, the approximation of the liquid level time series from video data of two instances of horizontal slug flow with manually marked gas-liquid interfaces as well as the derived time scales of the slugs have been qualitatively compared to reference parameters from well-established tomography measurements in Publication III, see Section 2.3. It was found that, the liquid level time series from the video recordings are systematically overestimated with respect to the liquid level time series from the tomography system. However, the derived temporal characteristics of the liquid slugs are in good agreement, especially for the slug unit times. Thus, the approximation of the liquid level time series from video recordings of horizontal slug flow allows a reasonable temporal characterization of the slugs. The comparison of the liquid level time series from video data $h_L^{video}(t)$ with the liquid level and holdup time series from the tomography measurements, $h_L^{tomo}(t)$ and $\alpha_L^{tomo}(t)$, as well as the probability density function (pdf) of the derived time scales, namely slug unit time T_U and slug body time T_B, are illustrated in Figure 3.2.

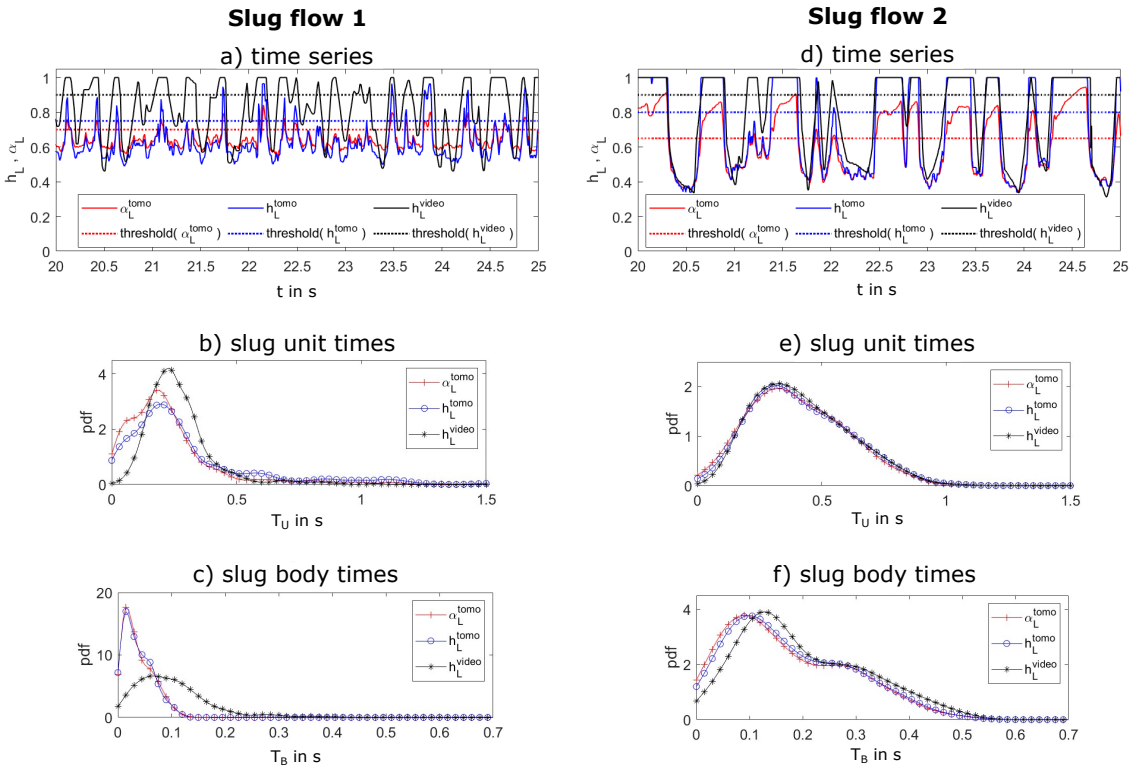

Figure 3.2: Illustration of the qualitative comparison of the temporal quantification for Slug flow 1 and 2 from video data and tomography measurements. For details see Publication III in Section 2.3

For this investigation, two instances of gas-oil slug flow have been considered, which represent margins for the optical assessability of the gas-liquid interface and the liquid structures of the flow. The video recording of the first experiment, denoted as Slug flow 1 in

Publication III (Section 2.3), predominantly shows short aerated slugs with numerous large amplitude waves and foam, see Figure 3.2a. Due to that, a clear assignment of the interface in the camera-based flow observations is not obvious, particularly for the foamy regions and aerated parts of the slugs and waves. In contrast to this, the video recording of the second case, denoted as Slug flow 2 in Publication III (Section 2.3), shows larger slugs with reduced aeration and foam, as well as fewer waves, see Figure 3.2d. For this case, the interface is clearly assignable in the video recordings.

To achieve a comparability of the parameters from video observations and the ECT-System, preprocessing steps have been employed. This inlcudes a correction of the refractive effects of the transparent pipe wall for the video data, as well as the construction of the liquid level time series from the ECT-measurements, which are discussed in the following.

3.2.1 Comparability of video and tomography data

In this qualitative comparison, data from video recordings and measurements from an ECT-system have been used for approximations of the liquid level time series. These two different types of data are readily comparable. The video recordings show the flow from the side through a transparent viewing section. Thus, the obtained images represent a two-dimensional projection of three dimensional flow from the side. The ECT-system on the other hand, provides phase fraction measurements in the pipe cross-section. For a better comparability between the observed liquid level in the videos and the measured reference parameters, the refractive effects of the transparent pipe wall have been corrected, which are primarily caused by the curvature and the thickness of the pipe wall as well as the different optical properties of the media [109]. For this, a post processing routine has been developed, which is based on the law of refraction [110], basic trigonometric relations and optical and geometrical properties of the pipe wall, for details see Publication III in Section 2.3. This is similar to the approach in [111]. The correction accounts for the vertical distortion in the observation of the interface through the transparent pipe wall, especially close to the bottom and the top of the pipe, which are crucial areas for the observation of slug flow. Such refractive effects and distortions can be reduced for optical measurements by using specifically designed optical measurement section, see for instance [64, 112]. However, the considered experimental setup only consists of the transparent pipe segment such that the refractive effects need to be corrected a posteriori.

To further enhance a comparability of the different data sets, suitable parameters have been constructed from the tomography measurements. The ECT-system provides spatially and temporally resolved liquid volume fraction measurements in the pipe cross section, see Section 1.4. From these measurements, a liquid level time series is constructed for the comparison with the video data. For this, the time series of the vertical position of the gas-liquid interface is extracted from the phase fraction measurements in the vertical centerline of the pipe cross-section. This is similar to the conventional wire-sensor measurements of the liquid level, see [36, 57, 59]. To define a unique location of the gas-liquid interface from the spatially resolved liquid volume fraction values α_L along the considered vertical line through the pipe for every time t, a threshold is applied. This threshold is defined as the median of all vertical positions within the considered vertical line, where $0.4 < \alpha_L < 0.5$ holds, see Figure 2 in Publication III (Section 2.3). The interval $(0.4, 0.5)$ for the threshold was chosen in accordance to the gas-

liquid interface visualization for horizontal slug flow with the same ECT-measurement system, given in [40]. The median of the detected positions was chosen to make the vertical interface position unique and robust against outliers, such as artifacts in the measurement. With this construction, a liquid level time series can be extracted from the temporally and spatially resolved cross-sectional phase fraction measurements, denoted as $h_L^{tomo}(t)$, see Publication III in Section 2.3.

3.2.2 Comparison of the time series and time scales

The liquid level time series extracted from video recordings $h_L^{video}(t)$ have been compared with the liquid level time series $h_L^{tomo}(t)$ and the liquid holdup time series $\alpha_L^{tomo}(t)$ extracted from the tomography system for both slug flows, see Figure 3.2a,d. It was noted that $h_L^{video}(t)$ showed systematically larger values compared to $\alpha_L^{tomo}(t)$ and $h_L^{tomo}(t)$. This is primarily caused by the type of data, which have been used for the different approximations of the liquid level time series, i.e., a two-dimensional projection of a three dimensional flow from the side in contrast to volumetric phase fraction data from pipe-cross sections. Due to that, the approximation of the interface from the video data includes foam and aerated regions in the slugs and waves as liquid phase, whereas the volumetric measurement only measures the proportion of the liquid. Furthermore, the volumetric measurement in the pipe cross-section accounts for detailed changes in vertical and transversal directions, whereas a vertical line through the pipe in the two-dimensional projection of the flow from the video data only accounts for changes in the vertical direction. This causes larger values for $h_L^{video}(t)$ compared to $h_L^{tomo}(t)$ and particularly compared to $\alpha_L^{tomo}(t)$, Figure 3.2a, d. Moreover, these differences become larger with increasing dispersion of the phases in the flow, such as atomization of the liquid, aerated liquid in the slugs and waves as well as foam. For these reasons, the liquid level approximations derived from these types of data, show larger differences for the Slug flow 1, which has more of such undesired phenomena, compared to Slug flow 2, see Figure 3.2 and Publication III in Section 2.3. Another parameter that influences the deviations between the different liquid level approximations in this qualitative comparison is the distance in between the points of observation/measurement, in which the structures of the flow can change, i.e., the distance between the viewing section and the ECT-measurement section. For the considered experiments, the liquid level approximations have been made at centered position of each section, resulting in a distance of approximately 14 inner pipe diameters, see Publication III in Section 2.3. For such a short distance, slug flows with short slugs, numerous waves and dispersed regions, such as Slug flow 1, will be more affected by the change of the flow structures than slug flows with longer and more distinct slugs, such as Slug flow 2.

In contrast to the systematic overestimation of the absolute values in the video based liquid level approximations, the derived characterizing time scales of slug flow showed good agreement, see Figure 3.2b, c, e, f. These time scales have been derived from the different liquid level time series $h_L^{video}(t)$ and $h_L^{tomo}(t)$ as well as from the holdup time series $\alpha_L^{tomo}(t)$ for both slug flows, using the conventional thresholding procedure, described in the previous sections. To find suitable values, the thresholds have been chosen individually for each time series, see Figure 3.2a, d. It was found that, the pdfs of the slug unit times extracted from the different time series show similar behavior, particularly for Slug flow 2. For this slug flow,

which consists of larger slugs and fewer waves, the pdfs are almost identical. In contrast to this, the pdfs of the slug body times showed more deviations, especially for Slug flow 1, which consists of short slugs, numerous waves and dispersed regions. One reason for this is that, the slugs appear longer in the video recordings, compared to the tomography measurements, see Figure 3.2a,d. This is caused by the overestimation of liquid for the aerated regions in the slugs in the video, which are particularly located close to the slug fronts due to the mixing eddy, as well as close to the slug rears due to the shedding of the entrained gas from to slug into the liquid layer behind, see Figure 1.2 and Section 1.2.1 for the phenomenology of the slugs. Thus, also the slug body times become longer for the video data. However, the time scales of the slugs, which have been derived from the video recordings of the considered slug flow experiments provide a reasonable and consistent temporal characterization of slug flow. This holds in particular for the slug unit times and the related slug frequencies, see Equation (1.1).

Altogether, a systematic overestimation of the liquid level time series approximation from the video data is noted in this qualitative comparison. Thus, measurements of related flow parameters, e.g., liquid film thickness, from video data should only be done under careful consideration, particularly for horizontal slug flow. In contrast to this, the derived temporal characteristics of the liquid slugs from video recordings provide a reasonable and consistent temporal characterization of slug flow. It was found that shorter aerated slugs and dispersed regions are leading to larger errors in the derived time scales for the video data. For slug flows with larger slugs and fewer dispersed regions, which is typically the case for slug flows in a fully developed state [27], the proposed temporal quantification of horizontal slug flow from video recordings has the potential to provide accurate time scales of the slugs.

In this regards, for academic or industrial application, where temporal quantifications of horizontal slug flows and other separated and intermittent flow pattern are needed, a fast and reliable method for the approximation of the liquid level time series from video data can serve as a useful tool. In this context, the accurate, efficient and automated extraction of the liquid level time series from video recordings with a novel deep learning based image processing technique is discussed in the next section.

3.3 Accurate and efficient extraction of the liquid level time series from video observations of multiphase flows with a deep learning model

The slugs in horizontal slug flow can generally grow to large structures with average lengths of more than 40 pipe diameters in their stable state. Even lengths of up to 500 pipe diameters have been reported, see [113]. For investigations of slug flows with such long slugs, temporal quantifications are preferably considered since a direct spatial characterization with images of entire slugs, for instance with the previously proposed snapshot POD analysis, is impractical. As mentioned in Section 3.1.2, the snapshot POD can also provide an approximation of the dynamics of the gas-liquid interface from short regions of interest, which do not resolve the slugs entirely. However, the eigenvalue decomposition and the construction of the spatial modes in the snapshot POD algorithm are memory and time consuming calculations. Furthermore, the

absolute values of the liquid level time series are not reproduced in this approximation. Thus, a fast image processing technique, which automatically extracts an accurate approximation of the liquid level time series from video recordings of separated and intermittent flow patterns can serve as a useful tool in related industrial and academic operations.

Most of the image processing techniques for the measurement of characteristic parameters for separated and intermittent horizontal two-phase flows are using fixed sequences of image filters and pixelwise comparisons to detect the gas-liquid interface or to segment the gas and liquid regions. This methods include grayscale transformation, contrast enhancement, threshold binarization, and edge-detection with pixel-value gradients, in particular for gas-water flows, see [64, 62, 108, 107]. For gas-oil slug flows, a similar procedure was proposed in the author's earlier work [62]. These approaches have been developed for specific video recording setups, liquids, and lighting. They often require individual adaptations for changes in these conditions, due to the pixelwise comparisons, see for instance the different approaches needed to extract the interface for gas-oil and gas-water slug flows in [62]. In contrast to this, deep learning models have the potential to overcome such difficulties and to provide reliable and more versatile image processing techniques.

Deep learning describes a family of learning algorithms in the field of machine learning and artificial intelligence [114]. It is used to learn complex and robust prediction models, e.g., multi-layer neural networks with many hidden units, directly from the data without the need of carefully engineering suitable features [114, 91]. Deep learning has a wide range of applications in science, business, and technology, e.g., in image or speech recognition, see [98, 91, 93, 115]. However, in the field of multiphase flows, deep learning has rarely been applied. In the context of numerical simulations of multiphase flows, deep learning models have been used to approximate the governing equations, estimate simulation errors, and predict flow parameters as well as closure coefficients, see e.g., [116, 117, 118]. Further applications of deep learning in the field of multiphase flows are the prediction of flow patterns and parameters, such as mean flow rates or mean phase fractions, based on operating conditions or related measurements, see [119, 120, 121, 47]. Moreover, image processing techniques based on deep convolutional neural networks have been presented in [122, 123, 124, 125, 126] for the detection, reconstruction, and analysis of gas bubbles in vertical pipes and micro-channels, as well as for the extraction of relevant water-regions as pre-processing step for two-phase PIV-measurements in the field of ship and ocean engineering. For the quantification of separated and intermittent gas-liquid flow patterns in horizontal pipes, such as wavy or slug flow, such advanced image processing techniques have not been reported.

In this context, a novel deep-learning based image processing method is presented in Publication IV in Section 2.4. It has been shown that, this method accurately and reliably extracts the liquid level time series from video recordings of stratified wavy and slug flows for different recording setups, liquids, and lighting conditions. This extraction includes several image processing steps, which are briefly described and discussed in the following.

3.3.1 Image processing steps

The proposed deep-learning based image processing method consists of several image processing steps. At first, the RGB-values in a pixelcolumn along a vertical line through the pipe (inner

pipe diameter) are extracted from the video frames at a desired longitudinal position in the observed pipe segment and stacked. The resulting image, also called RGB-pixelcolumn over time, represents a two-dimensional projection of the three-dimensional flow in the observed vertical line through the pipe from the side with its temporal variations. For suitable separated and intermittent flows, this image allows an approximation of the phase distribution with its temporal changes in the observed vertical line, see for instance Figure 4 in Publication IV (Section 2.4). This is similar to the previously proposed approaches for the liquid level extraction in Publication I, II, III and in [62]. Then, the phase distribution in this image is approximated by the segmentation of gas and liquid regions, similar to phase volume fraction fields. This segmentation task is performed by an previously trained and tested deep-learning model, which is based on a U-net. Before the RGB-pixelcolumn over time is segmented by the deep-learning model, the long image is cut in length and reshaped in height into evenly sized segments, which are individually normalized with an RGB-componentwise z-score to reduce the influence of disturbances in the video recording setup, such as differences in luminance or color. It was found that, this normalization led to the most accurate and consistent training results, compared to other RGB-componentwise or image wise normalizations, for instance with the maximum norm. A similar result for the z-score normalization has been reported for the image processing procedure for bubbly two-phase flows in [123]. Afterwards, the segmented image is binarized to obtain a sharp representation of the gas-liquid interface, from which the approximation of the liquid level time series is calculated with a simple edge detection. For details, see Publication IV in Section 2.4. The essential step in this image processing technique is the segmentation of gas and liquid regions with the trained deep-learning model. This model with its training and testing process is discussed in the following.

3.3.2 Training and testing of the deep learning model

The used deep-learning model was extensively trained and tested with video data from real slug flow experiments and classifies each region in the RGB-pixelcolumn over time into its respective phase being either liquid or gas. The model is based on the U-net, a convolutional neural network architecture for a fast and precise segmentation of images that was introduced by Ronneberger et al. [98]. It has been successfully applied in many image-to-image learning problems, e.g., computer tomography, see [99, 100, 101]. The U-net is typically trained in a supervised manner and able to achieve accurate results with only few labelled training data [98]. For these reasons, the U-net was chosen for the liquid-gas segmentation in the proposed image processing technique. It was trained and tested with video data from 18 different horizontal gas-liquid slug flow experiments from two different recording setups with different liquid colors. These different recording setups also include different background colors, lighting conditions, reflections and other noise effects. The videos show each flow from the side for a duration of 120 s to 150 s, see Section 1.4 or Publicaiton IV in Section 2.4 for details. To prepare the video data for the training of the U-net, the RGB-pixelcolumns over time have been extracted and binary segmentation masks have been generated from hand-labelled gas-liquid interfaces in the RGB-pixelcolumns over time for all experiments. These masks have a sharp interface with values of 1 for gas and 0 for liquid and represent an approximation of the temporally resolved gas volume fraction fields in the observed vertical line through the pipe. For the

testing in the optimization process of the training procedure, a subset of these data, i.e. two out of 18 experiments, was randomly chosen, and the data is split into a disjoint training and test set. The U-net was trained on a set of 483 pairs and tested on a set of 61 pairs of RGB-images and corresponding masks (544 pairs in total), as described in Publication IV in Section 2.4. Although, training sets of large numbers of images and masks are generally used for segmentation and recognition tasks, see e.g., [122], for the segmentation of gas and liquid in two phase flows, CNN-based models have also been successfully trained on data sets with just several hundreds of image pairs [126, 125], in particular for the U-net, which is able to achieve accurate results with only few labelled training data [98]. Since the segmentation includes only two classes, i.e., gas and liquid, the binary accuracy function was chosen as accuracy metric for the comparison of predicted segmentation maps and hand-labelled segmentation masks, see Publication IV in Section 2.4. The training was terminated after 42 epochs due to early stopping. The best model was found after 31 epochs. For this model, a mean binary accuracy of 97.91% for the training set and a mean binary accuracy of $97,74\%$ for the test set, was achieved. The mean binary accuracies for the prediction on the individual experiments varies from 96.86% to 98.85%. These accuracies are high, compared to the reported training and test accuracies in between 89% and 98.7% of other successfully trained gas and liquid segmentation models, see e.g. [124, 125, 126]. In a second step, the mean absolute error of the derived liquid level times series from the predicted and hand-labelled segmentation maps have been considered. This error varies from 1.15% to 3.12% for the individual experiments from the training and test set. It was also observed that, the predictions from the trained model showed more detailed and consistent segmentation maps compared to the hand-labelled masks, see Publication IV in Section 2.4. From these high accuracies and low errors for the training and test data, it can be concluded that, the model was trained successfully for its task and performs well for the considered types of data. For further evaluations on the reliability and versatility of the trained model, video data from three additional experiments were considered, which differ from the ones used for training and testing in recording setup, liquid color, and flow pattern, see Publication IV in Section 2.4. For the previously unseen data sets of these three expermients, the binary accuracies for the predicted segmentations reaches from 95.41% to 97.68% and the mean absolute error of the extracted liquid level time series reaches from 2.32% to 4.92%. From the high accuracies and low errors for the disjoint test set and the three additional unseen data sets, it can be concluded, that the model is able to generalize to unseen data and accurately predicts the segmentation maps also for different recording setups, liquids, and flow patterns.

In addition, the consistency of the hand-labelled data sets has been proven in an inter-observer reliability test that measures the degree of consistency of subjective judgments among independent observers, see [127, 128]. For this, the Pearson-correlation [129] of the hand-labelled liquid level time series from three independent observers have been considered for the video data from four different slug flow experiments. The Pearson-correlation is a common measure for this task, see [127]. These correlation values are in between 0.914 and 0.985, i.e., close to 1, which indicates a strong correlation and a high degree of consistency between the hand-labelled liquid level time series of the different observers. Hence, it can be concluded that, the hand-labelled gas-liquid interfaces provide reliable segmentation masks

for the training of the U-net. Furthermore, this analysis was also applied to the prediction of the U-net to quantify the degree of consistency between the prediction and the labels of the independent observers, see also [130]. In addition to this, also the pointwise error was considered. In the comparison of the predicted liquid level time series with the hand-labelled time series, it was found that, the predictions of the U-net also provide liquid level time series, which are consistent with respect to the different observers.

Altogether, the presented method accurately extracts the liquid level time series from the considered video data of stratified wavy and slug flow. It can handle different types of data, even unseen data sets. Once, the net is successfully trained, it predicts highly accurate segmentation maps in very short time. The segmentation of an image with the size of 128×1024px only takes a few milliseconds on the used *Intel Core i5-8265U CPU @ 1.6GHz*, e.g., 9 ms for one image segment of Experiment Nr. $11 - 100D$ from Publication IV in Section 2.4. Apart from the differences in recording setups, liquids, and flow patterns, the used video data also showed various noise effects, lighting conditions, and light reflections on the pipe wall, which posed serious problems for the liquid level approximation with the previously published image filter technique in [62]. Due to these disturbances, the approximation with the filter-based technique was not successful for several of the videos, see for instance Publication II in Section 2.2. In contrast to this, the trained deep learning model can overcome such effects and predicts highly accurate segmentation maps, also for the cases, where the filter-based technique was not successful. The proposed model was trained with videos of different slug flows. This flow pattern also includes stratified smooth and wavy regions in between the slugs, which where also captured in the video recordings of the slug flows. Moreover, the plug flow pattern is very similar to the slug flow pattern, particularly for video data, as mentioned in Section 1.2. Consequently, the model can generally be applied for separated and intermittent gas-liquid flow patterns as demonstrated for stratified wavy and slug flow in Publication IV in Section 2.4.

3.3.3 Limitations and outlook

The visual recognition of gas and liquid regions or the gas-liquid interface in the video data constitutes a limitation of the successful segmentation with the trained model. For flows, where the interface cannot be observed from the side, a meaningful segmentation cannot be provided. This is for instance the case for dispersed or annular flows as well as for flows with large amounts of liquid spray, such as for slug flows in the transition to a dispersed or annular flow pattern. Furthermore, for foamy regions in separated and intermittent gas-liquid flows, the segmentation often includes the foam into the liquid phase, leading to overestimated absolute values for the liquid level time series as mentioned in Publication 2.3. However, for separated and intermittent flows, where the gas-liquid interface can clearly be observed from the side, a meaningful segmentation is provided by this method.

Because of its proven accurate and fast segmentation for various recording setups of suitable separated and intermittent two-phase flow patterns, the proposed deep-learning based image processing method can serve as a useful non-intrusive technique in related industrial and academic operations. This includes the development, calibration and validation of predictive models, correlations, and simulations in the field of multiphase flows as well as the monitoring

of such types of flows for operation control in different sectors of the energy industry, including transportation pipelines in the oil and gas industry as well as cooling systems in the nuclear energy industry.

4

Conclusions and outlook

In this thesis, quantitative methods for the characterization of separated and intermittent gas-liquid flow patterns have been presented and discussed. This includes the temporal and spatial characterization of horizontal slug flow with the most dominant mode pair of a snapshot POD analysis from spatially and temporally resolved phase fraction fields and video recordings as well as the extraction of the liquid level time series with a deep learning based image processing technique for video recordings of separated and intermittent gas-liquid flow patterns.

The scientific results, which have been presented in Publication I and II (see Section 2.1 and 2.2) and discussed in Section 3.1.1, are leading to the conclusion that, the slugs are represented in the dominant mode pair of a snapshot POD analysis for the considered slug flow data sets. This includes a description of the gas-liquid interface dynamics (approximation of the dynamics of the liquid level time series) in the temporal coefficients as well as the representation of the averaged slug in the spatial modes. Hence, the snapshot POD allows a detailed temporal and spatial characterization of the slugs.

As presented in Publication I and II (Section 2.1 and 2.2) and discussed in Section 3.1.2, the conventional length and time scales for the characterization of horizontal slug flow can be derived from the most dominant mode pair of a snapshot POD analysis. Moreover, it was found that the length of the observed pipe segment (region of interest) affects the accuracy of the approximation of the liquid level time series by the temporal coefficient as well as the representation of the the averaged slug in the spatial modes. Hence, for a meaningful spatial and temporal characterization of slug flow with its length and time scale derived from the most dominant mode pair, the region of interest should have the necessary length to resolve the averaged slug entirely, but should remain sufficiently short to avoid larger errors in the characterizing parameters. If only a characterization in time is sought, the region of interest should be chosen as short as possible. Apart from the length of the observed pipe segment, the data should represent the phase distribution with its temporal changes in order to characterize horizontal slug flow with a snapshot POD analysis, as discussed in Section 3.1.3.

Consequently, limitations for a successful temporal and spatial characterization of horizontal slug flow with snapshot POD are given by the data, i.e., the spatial and temporal information captured in it. Other limitations of this approach are that, the temporal coefficients only

approximate the dynamics of the liquid level time series and not their absolute values. Due to that, direct estimations of other flow parameters, such as volumetric phase fraction or liquid film thickness in the pipe, cannot be made from it. A further consequence of this missing information is that, an identification of the flow pattern is not obvious. In detail, without the absolute values for the vertical position of the gas-liquid interface in the temporal coefficients, a differentiation between a wavy flow with large amplitude waves and a slug flow with short slugs is difficult. Another limiting aspect is the computational time of the POD algorithm. Generally, the eigenvalue decomposition and the construction of the spatial modes in the snapshot POD algorithm are memory and time consuming calculations. Furthermore, the slugs in horizontal slug flow can generally grow to large structures. For investigations of slug flows with long slugs, temporal quantifications are preferably considered since a direct spatial characterization with images of entire slugs, for instance with the snapshot POD analysis, is impractical. In this context, a fast and accurate deep learning based image processing method for the approximation of the liquid level time series with its absolute values from video recordings of horizontal slug flow as well as other separated and intermittent gas-liquid flow pattern in horizontal pipes was developed.

As presented in Publication IV (Section 2.4) and discussed in Section 3.3, the image processing method consists of an extensively trained and tested deep learning model for the segmentation of gas and liquid regions in the video data as well as several pre- and post-processing steps to approximate the liquid level time series. It was shown that, the method accurately extracts the liquid level time series from the considered video data of stratified wavy and slug flow. It can handle different types of data, even unseen data sets, and overcomes various noise effects, which are generally included in this kind of image or video data. As demonstrated in Publication IV (see Section 2.4), the model cannot only be applied to slug flow, but also to other separated and intermittent gas-liquid flow patterns in horizontal pipes.

In the course of the investigations in this thesis, video recordings have been used to characterize horizontal slug flow and to find an approximation of the liquid level time series and the time scales of the slugs. This temporal quantification of horizontal slug flow from video recordings have been validated with reference parameters from a conventional tomography measurement system as presented in Publication III (Section 2.3) and discussed in Section 3.2. It was found that, the approximation of the liquid level time series from the video data is systematically overestimated. Thus, measurements of related flow parameters, e.g., liquid film thickness, from video data of horizontal slug flow should only be done under careful consideration. In contrast to this, the derived temporal characteristics provide a reasonable and consistent temporal characterization of slug flow. It was noted that, shorter aerated slugs and dispersed regions are leading to larger errors in the derived time scales for the video data. For slug flows with larger slugs and fewer dispersed regions, which is typically the case for slug flows in a fully developed state, the proposed temporal quantification of horizontal slug flow from video recordings has the potential to provide accurate time scales of the slugs.

A general limitation for the characterization of gas-liquid flows with video or image data is given by the visual recognition of the gas and liquid regions and the gas-liquid interface. This applies not only for the successful image segmentation of the phases with the trained deep model, but also for the snapshot POD analysis of video data. For separated and intermittent

flows, where the gas-liquid interface can clearly be observed from the side, a meaningful characterization is provided by these methods. For flows, where the interface cannot be observed in the video data, a meaningful characterization cannot be provided by the proposed methods. This is for instance the case for dispersed or annular flows as well as for flows with large amounts of liquid spray or foam, such as for slug flows in the transition to a dispersed or annular flow pattern.

Prospectively, the proposed quantitative methods can be used for the development, calibration and validation of predictive models, correlations and simulations for separated and intermittent gas-liquid flows in horizontal pipes. In this context, the characterization of horizontal slug flow with snapshot POD can be further improved by the approximation of the absolute values of the liquid level time series in the temporal coefficients under the use of the information provided by the spatial modes and the mean field. Since the deep learning based image processing method provides a fast and accurate approximation of the liquid level time series from video data, it is also suitable for the monitoring of such types of flows in different sectors of the energy industry, including transportation pipelines in the oil and gas industry as well as cooling systems in the nuclear energy industry. Here, the versatility of the trained deep learning model can be further improved by additional instances of training with different types of data, for instance from bubbly flows or vertical flow patterns.

References

[1] G. Yadigaroglu and G. F. Hewitt. *Introduction to multiphase flow: basic concepts, applications and modelling*. Springer, 2017.

[2] C. J. Adkins and C. J. Adkins. *Equilibrium thermodynamics*. Cambridge University Press, 1983.

[3] E. Fermi. *Thermodynamics*. Dover books in physics and mathematical physics. Dover Publications, 1956. ISBN: 9780486603612. URL: https://books.google.de/books?id=VEZ1ljsT3IwC.

[4] J. W. Tester, M. Modell, et al. *Thermodynamics and its Applications*. Prentice Hall PTR, 1997.

[5] E. Michaelides, C. T. Crowe, and J. D. Schwarzkopf. *Multiphase flow handbook*. CRC Press, 2016.

[6] T. J. Hanratty. *Physics of gas-liquid flows*. Cambridge University Press, 2013.

[7] A. Pieper. *Final Publishable Report - Multiphase flow reference metrology (16ENG07)*. Tech. rep. EURAMET, 2020.

[8] S. Pedersen, P. Durdevic, and Z. Yang. "Challenges in slug modeling and control for offshore oil and gas productions: A review study". In: *International Journal of Multiphase Flow* 88 (2017), pp. 270–284.

[9] W. Wulff. "Computer simulation of two-phase flow in nuclear reactors". In: *Nuclear engineering and design* 141.1-2 (1993), pp. 303–313.

[10] L. Fu and Y.-C. Jin. "Improved Multiphase Lagrangian Method for Simulating Sediment Transport in Dam-Break Flows". In: *Journal of Hydraulic Engineering* 142.6 (2016), p. 04016005. DOI: 10.1061/(ASCE)HY.1943-7900.0001132.

[11] C. Liu, Z. Li, L. Zeng, Q. Zhang, R. Hu, X. Zhang, L. Guo, Y. Huang, X. Yang, and L. Chen. "Gas/particle two-phase flow characteristics of a down-fired 350 MWe supercritical utility boiler at different tertiary air ratios". In: *Energy* 102 (2016), pp. 54–64.

[12] J. B. Kitto and M. J. Albrecht. "Elements of Two-Phase Flow in Fossil Boilers". In: *Two-Phase Flow Heat Exchangers: Thermal-Hydraulic Fundamentals and Design*. Ed. by S. Kakaç, A. E. Bergles, and E. O. Fernandes. Dordrecht: Springer Netherlands, 1988, pp. 495–551.

[13] S. Sundaresan. "Modeling the hydrodynamics of multiphase flow reactors: Current status and challenges". In: *AIChE Journal* 46.6 (2000), pp. 1102–1105. DOI: https://doi.org/10.1002/aic.690460602. eprint: https://aiche.onlinelibrary.wiley.com/doi/pdf/10.1002/aic.690460602. URL: https://aiche.onlinelibrary.wiley.com/doi/abs/10.1002/aic.690460602.

[14] C. E. Brennen. *Fundamentals of Multiphase Flow*. Cambridge University Press, 2005. DOI: 10.1017/CBO9780511807169.

[15] G. Takacs. "Chapter 2 - A Review of Production Engineering Fundamentals". In: *Sucker-Rod Pumping Handbook*. Ed. by G. Takacs. Boston: Gulf Professional Publishing, 2015, pp. 13–56. ISBN: 978-0-12-417204-3. DOI: https://doi.org/10.1016/B978-0-12-417204-3.00002-9. URL: https://www.sciencedirect.com/science/article/pii/B9780124172043000029.

[16] M. Lu. "Experimental and computational study of two-phase slug flow". PhD thesis. Imperial College London, 2015.

[17] *Design of Pipelines for the Simultaneous Flow of Oil and Gas*. Vol. All Days. SPE Annual Technical Conference and Exhibition. SPE-323-G. Oct. 1953. DOI: 10.2118/323-G. eprint: https://onepetro.org/SPEATCE/proceedings-pdf/53FM/All-53FM/SPE-323-G/2085003/spe-323-g.pdf. URL: https://doi.org/10.2118/323-G.

[18] G. E. Alves. "Cocurrent liquid-gas flow in a pipe-line contactor". In: *Chemical Engineering Progress* 50.9 (1954), pp. 449–456.

[19] F. Holland and R. Bragg. "7 - Gas–liquid two-phase flow". In: *Fluid Flow for Chemical Engineers (Second Edition)*. Ed. by F. Holland and R. Bragg. Second Edition. Oxford: Butterworth-Heinemann, 1995, pp. 219–267. ISBN: 978-0-340-61058-9. DOI: https://doi.org/10.1016/B978-034061058-9.50009-8. URL: https://www.sciencedirect.com/science/article/pii/B9780340610589500098.

[20] J. Mandhane, G. Gregory, and K. Aziz. "A flow pattern map for gas—liquid flow in horizontal pipes". In: *International Journal of Multiphase Flow* 1.4 (1974), pp. 537–553. ISSN: 0301-9322. DOI: https://doi.org/10.1016/0301-9322(74)90006-8. URL: https://www.sciencedirect.com/science/article/pii/0301932274900068.

[21] Y. Taitel and A. E. Dukler. "A model for predicting flow regime transitions in horizontal and near horizontal gas-liquid flow". In: *AIChE Journal* 22.1 (1976), pp. 47–55. DOI: https://doi.org/10.1002/aic.690220105. eprint: https://aiche.onlinelibrary.wiley.com/doi/pdf/10.1002/aic.690220105. URL: https://aiche.onlinelibrary.wiley.com/doi/abs/10.1002/aic.690220105.

[22] Y. Taitel and A. Dukler. "A model for slug frequency during gas-liquid flow in horizontal and near horizontal pipes". In: *International Journal of Multiphase Flow* 3.6 (1977), pp. 585–596.

[23] E. Al-Safran. "Investigation and prediction of slug frequency in gas/liquid horizontal pipe flow". In: *Journal of Petroleum Science and Engineering* 69.1-2 (2009), pp. 143–155.

[24] D. Barnea, O. Shoham, Y. Taitel, and A. Dukler. "Flow pattern transition for gas-liquid flow in horizontal and inclined pipes. Comparison of experimental data with theory". In: *International Journal of Multiphase Flow* 6.3 (1980), pp. 217–225. ISSN: 0301-9322. DOI: https://doi.org/10.1016/0301-9322(80)90012-9. URL: https://www.sciencedirect.com/science/article/pii/0301932280900129.

[25] Z. Ruder, P. Hanratty, and T. Hanratty. "Necessary conditions for the existence of stable slugs". In: *International Journal of Multiphase Flow* 15.2 (1989), pp. 209–226. ISSN: 0301-9322. DOI: https://doi.org/10.1016/0301-9322(89)90071-2. URL: https://www.sciencedirect.com/science/article/pii/0301932289900712.

[26] Z. Ruder and T. Hanratty. "A definition of gas-liquid plug flow in horizontal pipes". In: *International Journal of Multiphase Flow* 16.2 (1990), pp. 233–242. ISSN: 0301-9322. DOI: https://doi.org/10.1016/0301-9322(90)90056-O. URL: https://www.sciencedirect.com/science/article/pii/030193229090056O.

[27] H. H. Al-Kayiem, A. O. Mohmmed, Z. I. Al-Hashimy, and R. W. Time. "Statistical assessment of experimental observation on the slug body length and slug translational velocity in a horizontal pipe". In: *International Journal of Heat and Mass Transfer* 105 (2017), pp. 252–260.

[28] V. De Henau and G. Raithby. "A study of terrain-induced slugging in two-phase flow pipelines". In: *International Journal of Multiphase Flow* 21.3 (1995), pp. 365–379. ISSN: 0301-9322. DOI: https://doi.org/10.1016/0301-9322(94)00081-T. URL: https://www.sciencedirect.com/science/article/pii/030193229400081T.

[29] R. Malekzadeh, R. Henkes, and R. Mudde. "Severe slugging in a long pipeline–riser system: Experiments and predictions". In: *International Journal of Multiphase Flow* 46 (2012), pp. 9–21. ISSN: 0301-9322. DOI: https://doi.org/10.1016/j.ijmultiphaseflow.2012.06.004. URL: https://www.sciencedirect.com/science/article/pii/S0301932212000894.

[30] L. Meng and X. Hao. "The Control Method of Pigging Slug Flow for Multiphase Subsea Pipeline". In: 542 (July 2019), p. 012082. DOI: 10.1088/1757-899x/542/1/012082. URL: https://doi.org/10.1088/1757-899x/542/1/012082.

[31] P. Yin, X. Cao, C. Wu, S. Qin, P. Zhang, and J. Bian. "The effect of surfactants on the initiation and development of air–water slug flow in hilly terrain pipeline". In: *Experimental Thermal and Fluid Science* 117 (2020), p. 110139. ISSN: 0894-1777. DOI: https://doi.org/10.1016/j.expthermflusci.2020.110139. URL: https://www.sciencedirect.com/science/article/pii/S0894177719320655.

[32] E. Kordyban. "Some details of developing slugs in horizontal two-phase flow". In: *AIChE Journal* 31.5 (1985), pp. 802–806. DOI: https://doi.org/10.1002/aic.690310515. eprint: https://aiche.onlinelibrary.wiley.com/doi/pdf/10.1002/aic.690310515. URL: https://aiche.onlinelibrary.wiley.com/doi/abs/10.1002/aic.690310515.

[33] Z. Fan, F. Lusseyran, and T. J. Hanratty. "Initiation of slugs in horizontal gas-liquid flows". In: *AIChE Journal* 39.11 (1993), pp. 1741–1753. DOI: https://doi.org/10.1002/aic.690391102. eprint: https://aiche.onlinelibrary.wiley.com/doi/pdf/10.1002/aic.690391102. URL: https://aiche.onlinelibrary.wiley.com/doi/abs/10.1002/aic.690391102.

[34] M. J. Vaze and J. Banerjee. "Prediction of liquid height for onset of slug flow". In: *The Canadian Journal of Chemical Engineering* 90.5 (2012), pp. 1295–1303. DOI: https://doi.org/10.1002/cjce.20626. eprint: https://onlinelibrary.wiley.com/doi/pdf/10.1002/cjce.20626. URL: https://onlinelibrary.wiley.com/doi/abs/10.1002/cjce.20626.

[35] A. E. Dukler and M. G. Hubbard. "A model for gas-liquid slug flow in horizontal and near horizontal tubes". In: *Industrial & Engineering Chemistry Fundamentals* 14.4 (1975), pp. 337–347.

[36] E. S. Kordyban and T. Ranov. "Mechanism of Slug Formation in Horizontal Two-Phase Flow". In: *Journal of Basic Engineering* 92.4 (Dec. 1970), pp. 857–864. ISSN: 0021-9223. DOI: 10.1115/1.3425157. eprint: https://asmedigitalcollection.asme.org/fluidsengineering/article-pdf/92/4/857/5638477/857_1.pdf. URL: https://doi.org/10.1115/1.3425157.

[37] D. Tiab and E. C. Donaldson. "Chapter 10 - Reservoir Characterization". In: *Petrophysics (Fourth Edition)*. Ed. by D. Tiab and E. C. Donaldson. Fourth Edition. Boston: Gulf Professional Publishing, 2016, pp. 583–640. ISBN: 978-0-12-803188-9. DOI: https://doi.org/10.1016/B978-0-12-803188-9.00010-3. URL: https://www.sciencedirect.com/science/article/pii/B9780128031889000103.

[38] *Slug Flow: Occurrence, Consequences, and Prediction*. Vol. All Days. SPE University of Tulsa Centennial Petroleum Engineering Symposium. SPE-27960-MS. Aug. 1994. DOI: 10.2118/27960-MS. eprint: https://onepetro.org/speutcpes/proceedings-pdf/94UTCPES/All-94UTCPES/SPE-27960-MS/1974258/spe-27960-ms.pdf. URL: https://doi.org/10.2118/27960-MS.

[39] L. S. Hansen, S. Pedersen, and P. Durdevic. "Multi-Phase Flow Metering in Offshore Oil and Gas Transportation Pipelines: Trends and Perspectives". In: *Sensors* 19.9 (2019). ISSN: 1424-8220. DOI: 10.3390/s19092184. URL: https://www.mdpi.com/1424-8220/19/9/2184.

[40] R. Drury, A. Hunt, and J. Brusey. "Identification of horizontal slug flow structures for application in selective cross-correlation metering". In: *Flow Measurement and Instrumentation* 66 (2019), pp. 141–149. ISSN: 0955-5986. DOI: https://doi.org/10.1016/j.flowmeasinst.2018.12.002. URL: https://www.sciencedirect.com/science/article/pii/S0955598618300542.

[41] A. Elliott, G. Falcone, D. van Putten, T. Leonard, K. Haukalid, and B. Pinguet. "Investigating reproducibility in multiphase flow metrology: Results from an intercomparison of laboratories". In: *Flow Measurement and Instrumentation* 79 (2021), p. 101951. ISSN: 0955-5986. DOI: https://doi.org/10.1016/j.flowmeasinst.2021.101951. URL: https://www.sciencedirect.com/science/article/pii/S0955598621000625.

[42] Q. Wang, J. Polansky, M. Wang, K. Wei, C. Qiu, A. Kenbar, and D. Millington. "Capability of dual-modality electrical tomography for gas-oil-water three-phase pipeline flow visualisation". In: *Flow Measurement and Instrumentation* 62 (2018), pp. 152–166. ISSN: 0955-5986. DOI: https://doi.org/10.1016/j.flowmeasinst.2018.02.007. URL: https://www.sciencedirect.com/science/article/pii/S0955598617300936.

[43] *A New Technique to Eliminate Severe Slugging in Pipeline/Riser Systems*. Vol. All Days. SPE Annual Technical Conference and Exhibition. SPE-63185-MS. Oct. 2000. DOI: 10.2118/63185-MS. eprint: https://onepetro.org/SPEATCE/proceedings-pdf/00ATCE/All-00ATCE/SPE-63185-MS/1903835/spe-63185-ms.pdf. URL: https://doi.org/10.2118/63185-MS.

[44] A. B. Ehinmowo, O. D. Orodu, P. A. Anawe, and O. O. Ogunleye. "Attenuating severe slug flow at large valve opening for increased oil production without feedback control signal". In: *Journal of Petroleum Science and Engineering* 146 (2016), pp. 1130–1141. ISSN: 0920-4105. DOI: https://doi.org/10.1016/j.petrol.2016.08.019. URL: https://www.sciencedirect.com/science/article/pii/S0920410516303321.

[45] J. Baliño, K. Burr, and R. Nemoto. "Modeling and simulation of severe slugging in air–water pipeline–riser systems". In: *International Journal of Multiphase Flow* 36.8 (2010), pp. 643–660. ISSN: 0301-9322. DOI: https://doi.org/10.1016/j.ijmultiphaseflow.2010.04.003. URL: https://www.sciencedirect.com/science/article/pii/S0301932210000807.

[46] A. O. Mohmmed, H. H. Al-Kayiem, M. S. Nasif, and R. W. Time. "Effect of slug flow frequency on the mechanical stress behavior of pipelines". In: *International Journal of Pressure Vessels and Piping* 172 (2019), pp. 1–9. ISSN: 0308-0161.

[47] Z. Lin, X. Liu, L. Lao, and H. Liu. "Prediction of two-phase flow patterns in upward inclined pipes via deep learning". In: *Energy* 210 (2020), p. 118541. ISSN: 0360-5442. DOI: https://doi.org/10.1016/j.energy.2020.118541. URL: https://www.sciencedirect.com/science/article/pii/S0360544220316492.

[48] *Advancements in Two-Phase Slug Flow Modeling*. Vol. All Days. SPE University of Tulsa Centennial Petroleum Engineering Symposium. SPE-27961-MS. Aug. 1994. DOI: 10.2118/27961-MS. URL: https://doi.org/10.2118/27961-MS.

[49] A. E. Dukler and J. Fabre. "GAS-LIQUID SLUG FLOW". In: *Multiphase Science and Technology* 8.1-4 (1994), pp. 355–469. ISSN: 0276-1459.

[50] Y. D. Baba, A. M. Aliyu, A. E. Archibong, M. Abdulkadir, L. Lao, and H. Yeung. "Slug length for high viscosity oil-gas flow in horizontal pipes: Experiments and prediction". In: *Journal of Petroleum Science and Engineering* 165 (2018), pp. 397–411.

[51] W. C. Lyons, J. H. Stanley, F. J. Sinisterra, and T. Weller. "Chapter 9 - Aerated Fluids Drilling". In: *Air and Gas Drilling Manual (Fourth Edition)*. Ed. by W. C. Lyons, J. H. Stanley, F. J. Sinisterra, and T. Weller. Fourth Edition. Gulf Professional Publishing, 2021, pp. 283–314. ISBN: 978-0-12-815792-3. DOI: https://doi.org/10.1016/B978-0-

12-815792-3.00009-X. URL: https://www.sciencedirect.com/science/article/pii/B978012815792300009X.

[52] G. Oddie and J. A. Pearson. "FLOW-RATE MEASUREMENT IN TWO-PHASE FLOW". In: *Annual Review of Fluid Mechanics* 36.1 (2004), pp. 149–172. DOI: 10.1146/annurev.fluid.36.050802.121935.

[53] P. Wiedemann, F. d. A. Dias, E. Schleicher, and U. Hampel. "Temperature Compensation for Conductivity-Based Phase Fraction Measurements with Wire-Mesh Sensors in Gas-Liquid Flows of Dilute Aqueous Solutions". In: *Sensors* 20.24 (2020). ISSN: 1424-8220. DOI: 10.3390/s20247114. URL: https://www.mdpi.com/1424-8220/20/24/7114.

[54] B. Viggiano, O. Skjæraasen, H. Schümann, M. Tutkun, and R. B. Cal. "Characterization of flow dynamics and reduced-order description of experimental two-phase pipe flow". In: *International Journal of Multiphase Flow* 105 (2018), pp. 91–101. ISSN: 0301-9322. DOI: https://doi.org/10.1016/j.ijmultiphaseflow.2018.03.020. URL: https://www.sciencedirect.com/science/article/pii/S0301932217309941.

[55] L. Wojtan, T. Ursenbacher, and J. R. Thome. "Interfacial measurements in stratified types of flow. Part II: Measurements for R-22 and R-410A". In: *International Journal of Multiphase Flow* 30.2 (2004), pp. 125–137. ISSN: 0301-9322. DOI: https://doi.org/10.1016/j.ijmultiphaseflow.2003.11.009. URL: https://www.sciencedirect.com/science/article/pii/S0301932203002210.

[56] N. Andritsos and T. J. Hanratty. "Influence of interfacial waves in stratified gas-liquid flows". In: *AIChE Journal* 33.3 (1987), pp. 444–454. DOI: https://doi.org/10.1002/aic.690330310. eprint: https://aiche.onlinelibrary.wiley.com/doi/pdf/10.1002/aic.690330310. URL: https://aiche.onlinelibrary.wiley.com/doi/abs/10.1002/aic.690330310.

[57] M. Sadatomi, M. Kawaji, C. Lorencez, and T. Chang. "Prediction of liquid level distribution in horizontal gas-liquid stratified flows with interfacial level gradient". In: *International Journal of Multiphase Flow* 19.6 (1993), pp. 987–997. ISSN: 0301-9322. DOI: https://doi.org/10.1016/0301-9322(93)90073-4. URL: https://www.sciencedirect.com/science/article/pii/0301932293900734.

[58] U. Kadri. "A Probabilistic Approach for Predicting Average Slug Frequency in Horizontal Gas/Liquid Pipe Flow". In: *Oil Gas Sci. Technol. - Rev. IFP Energies nouvelles* 69.2 (2014), pp. 331–339. DOI: 10.2516/ogst/2012070. URL: https://doi.org/10.2516/ogst/2012070.

[59] J. Koskie, I. Mudawar, and W. Tiederman. "Parallel-wire probes for measurement of thick liquid films". In: *International Journal of Multiphase Flow* 15.4 (1989), pp. 521–530. ISSN: 0301-9322. DOI: https://doi.org/10.1016/0301-9322(89)90051-7. URL: https://www.sciencedirect.com/science/article/pii/0301932289900517.

[60] U. Kadri. "Long liquid slugs in stratified gas/liquid flow in horizontal and slightly inclined pipes". Dissertation. Delft: Technical University Delft, 2009.

[61] Y. Ma, Z. Zheng, L.-a. Xu, X. Liu, and Y. Wu. "Application of electrical resistance tomography system to monitor gas/liquid two-phase flow in a horizontal pipe". In: *Flow Measurement and Instrumentation* 12.4 (2001), pp. 259–265. ISSN: 0955-5986. DOI: https://doi.org/10.1016/S0955-5986(01)00026-7. URL: https://www.sciencedirect.com/science/article/pii/S0955598601000267.

[62] M. Olbrich, E. Schmeyer, L. Riazy, K. Oberleithner, M. Bär, and S. Schmelter. "Validation of simulations in multiphase flow metrology by comparison with experimental video observations". In: *Journal of Physics: Conference Series* 1065 (Aug. 2018), p. 092015. DOI: 10.1088/1742-6596/1065/9/092015. URL: https://doi.org/10.1088/1742-6596/1065/9/092015.

[63] E. Carpintero Rogero. "Experimental Investigation of Developing Plug and Slug Flows". Dissertation. München: Technische Universität München, 2009.

[64] C. do Amaral, R. Alves, M. da Silva, L. Arruda, L. Dorini, R. Morales, and D. Pipa. "Image processing techniques for high-speed videometry in horizontal two-phase slug flows". In: *Flow Measurement and Instrumentation* 33 (2013), pp. 257–264. ISSN: 0955-5986. DOI: https://doi.org/10.1016/j.flowmeasinst.2013.07.006. URL: https://www.sciencedirect.com/science/article/pii/S0955598613000939.

[65] O. Dinaryanto, A. Widyatama, A. I. Majid, Deendarlianto, and Indarto. "Image processing analysis on the air-water slug two-phase flow in a horizontal pipe". In: *AIP Conference Proceedings* 1737.1 (2016), p. 040011. DOI: 10.1063/1.4949299. URL: https://aip.scitation.org/doi/abs/10.1063/1.4949299.

[66] A. Widyatama, O. Dinaryanto, Indarto, and Deendarlianto. "The development of image processing technique to study the interfacial behavior of air-water slug two-phase flow in horizontal pipes". In: *Flow Measurement and Instrumentation* 59 (2018), pp. 168–180. ISSN: 0955-5986. DOI: https://doi.org/10.1016/j.flowmeasinst.2017.12.015. URL: https://www.sciencedirect.com/science/article/pii/S0955598616302412.

[67] R. Wilkens and D. Thomas. "A simple technique for determining slug frequency using differential pressure". In: *Journal of Energy Resources Technology* 130.1 (2008).

[68] M. Sieber, C. O. Paschereit, and K. Oberleithner. "Spectral proper orthogonal decomposition". In: *Journal of Fluid Mechanics* 792 (2016), pp. 798–828. DOI: 10.1017/jfm.2016.103.

[69] K. Taira, S. L. Brunton, S. T. M. Dawson, C. W. Rowley, T. Colonius, B. J. McKeon, O. T. Schmidt, S. Gordeyev, V. Theofilis, and L. S. Ukeiley. "Modal Analysis of Fluid Flows: An Overview". In: *AIAA Journal* 55.12 (2017), pp. 4013–4041. DOI: 10.2514/1.J056060. eprint: https://doi.org/10.2514/1.J056060. URL: https://doi.org/10.2514/1.J056060.

[70] P. Holmes, J. L. Lumley, G. Berkooz, and C. W. Rowley. *Turbulence, Coherent Structures, Dynamical Systems and Symmetry*. 2nd ed. Cambridge Monographs on Mechanics. Cambridge University Press, 2012.

[71] J. L. Lumley. "The Structure of Inhomogeneous Turbulent Flows". In: *Atmospheric Turbulence and Radio Wave Propagation*. Ed. by A. M. Yaglom and V. I. Tatarski. Moskow: Nauka, 1967, 1967, pp. 166–178.

[72] L. Sirovich. "Turbulence and the dynamics of coherent structures. Part I: Coherent structures". In: *Quart. Appl. Math.* 45 (1987), pp. 561–571.

[73] S. Wold, K. Esbensen, and P. Geladi. "Principal component analysis". In: *Chemometrics and Intelligent Laboratory Systems* 2.1 (1987). Proceedings of the Multivariate Statistical Workshop for Geologists and Geochemists, pp. 37–52. ISSN: 0169-7439. DOI: https://doi.org/10.1016/0169-7439(87)80084-9. URL: http://www.sciencedirect.com/science/article/pii/0169743987800849.

[74] K. Oberleithner, L. Rukes, and J. Soria. "Mean flow stability analysis of oscillating jet experiments". In: *Journal of Fluid Mechanics* 757 (2014), pp. 1–32.

[75] M. Sieber, O. Paschereit, and K. Oberleithner. "Advanced Identification of Coherent Structures in Swirl-Stabilized Combustors". In: *Journal of Engineering for Gas Turbines and Power* (2017).

[76] R. Bourguet, M. Braza, and A. Dervieux. "Reduced-order modeling for unsteady transonic flows around an airfoil". In: *Physics of Fluids* 19.11 (2007), p. 111701. DOI: 10.1063/1.2800042. eprint: https://doi.org/10.1063/1.2800042. URL: https://doi.org/10.1063/1.2800042.

[77] T. Barber, M. Ahmed, and N. A. Shafi. "POD Snapshot Data Reduction for Periodic Fluid Flows". In: *43rd AIAA Aerospace Sciences Meeting and Exhibit*. DOI: 10.2514/6.2005-287. eprint: https://arc.aiaa.org/doi/pdf/10.2514/6.2005-287. URL: https://arc.aiaa.org/doi/abs/10.2514/6.2005-287.

[78] T. Bui-Thanh, M. Damodaran, and K. Willcox. "Aerodynamic Data Reconstruction and Inverse Design Using Proper Orthogonal Decomposition". In: *AIAA Journal* 42.8 (2004), pp. 1505–1516. DOI: 10.2514/1.2159. eprint: https://doi.org/10.2514/1.2159. URL: https://doi.org/10.2514/1.2159.

[79] A. Tallet, C. Allery, and C. Leblond. "Optimal flow control using a POD-based reduced-order model". In: *Numerical Heat Transfer, Part B: Fundamentals* 70.1 (2016), pp. 1–24. DOI: 10.1080/10407790.2016.1173472. eprint: https://doi.org/10.1080/10407790.2016.1173472. URL: https://doi.org/10.1080/10407790.2016.1173472.

[80] S. S. Ravindran. "Adaptive Reduced-Order Controllers for a Thermal Flow System Using Proper Orthogonal Decomposition". In: *SIAM Journal on Scientific Computing* 23.6 (2002), pp. 1924–1942. DOI: 10.1137/S1064827500374716. eprint: https://doi.org/10.1137/S1064827500374716. URL: https://doi.org/10.1137/S1064827500374716.

[81] P. LeGresley and J. Alonso. "Airfoil design optimization using reduced order models based on proper orthogonal decomposition". In: *Fluids 2000 Conference and Exhibit*. DOI: 10.2514/6.2000-2545. eprint: https://arc.aiaa.org/doi/pdf/10.2514/6.2000-2545. URL: https://arc.aiaa.org/doi/abs/10.2514/6.2000-2545.

[82] Q. Wang, J. Polansky, B. Karki, M. Wang, K. Wei, C. Qiu, A. Kenbar, and D. Millington. "Experimental tomographic methods for analysing flow dynamics of gas-oil-water flows in horizontal pipeline". In: *Journal of Hydrodynamics, Ser. B* 28.6 (2016), pp. 1018–1021.

[83] J. Polansky and M. Wang. "Proper Orthogonal Decomposition as a technique for identifying two-phase flow pattern based on electrical impedance tomography". In: *Flow Measurement and Instrumentation* 53 (2017), pp. 126–132.

[84] J. Polansky and M. Wang. "Vertical annular flow pattern characterisation using proper orthogonal decomposition of Electrical Impedance Tomography". In: *Flow Measurement and Instrumentation* 62 (2018), pp. 281–296.

[85] S. Munir, M. I. Siddiqui, M. Heikal, A. R. Abdul Aziz, and G. de Sercey. "Identification of dominant structures and their flow dynamics in the turbulent two-phase flow using POD technique". In: *Journal of Mechanical Science and Technology* 29.11 (2015), pp. 4701–4710.

[86] X. Tu and C. Trägårdh. "Methodology development for the analysis of velocity particle image velocimetry images of turbulent, bubbly gas-liquid flows". In: *Measurement Science and Technology* 13.7 (June 2002), pp. 1079–1086. DOI: 10.1088/0957-0233/13/7/315. URL: https://doi.org/10.1088/0957-0233/13/7/315.

[87] S. J. Yi, S. M. Kim, H. D. Kim, J. W. Kim, and K. C. Kim. "Spatial and temporal structures of turbulent bubble-driven flows in a rectangular water tank". In: *Journal of mechanical science and technology* 24.9 (2010), pp. 1819–1827.

[88] M. Pang and J. Wei. "Experimental investigation on the turbulence channel flow laden with small bubbles by PIV". In: *Chemical Engineering Science* 94 (2013), pp. 302–315. ISSN: 0009-2509. DOI: https://doi.org/10.1016/j.ces.2013.02.062. URL: https://www.sciencedirect.com/science/article/pii/S0009250913001796.

[89] B. Viggiano, O. Skjæraasen, H. Schümann, M. Tutkun, and R. B. Cal. "Characterization of flow dynamics and reduced-order description of experimental two-phase pipe flow". In: *International Journal of Multiphase Flow* 105 (2018), pp. 91–101.

[90] J. Schmidhuber. "Deep learning in neural networks: An overview". In: *Neural Networks* 61 (2015), pp. 85–117. ISSN: 0893-6080.

[91] Y. LeCun, Y. Bengio, and G. Hinton. "Deep learning". In: *nature* 521.7553 (2015), pp. 436–444.

[92] D.-X. Zhou. "Theory of deep convolutional neural networks: Downsampling". In: *Neural Networks* 124 (2020), pp. 319–327. ISSN: 0893-6080. DOI: https://doi.org/10.1016/j.neunet.2020.01.018. URL: https://www.sciencedirect.com/science/article/pii/S0893608020300204.

[93] A. Krizhevsky, I. Sutskever, and G. E. Hinton. "ImageNet Classification with Deep Convolutional Neural Networks". In: *Advances in Neural Information Processing Systems*. Ed. by F. Pereira, C. J. C. Burges, L. Bottou, and K. Q. Weinberger. Vol. 25. Curran Associates, Inc., 2012. URL: https://proceedings.neurips.cc/paper/2012/file/c399862d3b9d6b76c8436e924a68c45b-Paper.pdf.

[94] A. Dhillon and G. K. Verma. "Convolutional neural network: a review of models, methodologies and applications to object detection". In: *Progress in Artificial Intelligence* 9 (2020), pp. 85–112. ISSN: 2192-6360.

[95] N. Aloysius and M. Geetha. "A review on deep convolutional neural networks". In: *2017 International Conference on Communication and Signal Processing (ICCSP)*. 2017, pp. 0588–0592.

[96] M. Mohri, A. Rostamizadeh, and A. Talwalkar. *Foundations of Machine Learning*. Adaptive Computation and Machine Learning. MIT Press, 2018.

[97] S. J. Russell and P. Norvig. *Artificial Intelligence: a modern approach*. 3rd ed. Pearson, 2009.

[98] O. Ronneberger, P. Fischer, and T. Brox. "U-Net: Convolutional Networks for Biomedical Image Segmentation". In: *Medical Image Computing and Computer-Assisted Intervention – MICCAI 2015*. Ed. by N. Navab, J. Hornegger, W. M. Wells, and A. F. Frangi. Cham: Springer International Publishing, 2015, pp. 234–241. ISBN: 978-3-319-24574-4.

[99] X.-J. Mao, C. Shen, and Y.-B. Yang. "Image Restoration Using Very Deep Convolutional Encoder-Decoder Networks with Symmetric Skip Connections". In: *Proceedings of the 30th International Conference on Neural Information Processing Systems*. NIPS'16. Barcelona, Spain: Curran Associates Inc., 2016, pp. 2810–2818. ISBN: 9781510838819.

[100] A. Dosovitskiy, P. Fischer, E. Ilg, P. Hausser, C. Hazirbas, V. Golkov, P. van der Smagt, D. Cremers, and T. Brox. "FlowNet: Learning Optical Flow With Convolutional Networks". In: *Proceedings of the IEEE International Conference on Computer Vision (ICCV)*. Dec. 2015.

[101] K. H. Jin, M. T. McCann, E. Froustey, and M. Unser. "Deep Convolutional Neural Network for Inverse Problems in Imaging". In: *IEEE Transactions on Image Processing* 26.9 (2017), pp. 4509–4522.

[102] D. Crawford. *Final Publishable JRP Report and associated Annex A - Multiphase Flow Metrology in Oil and Gas Production (ENG58)*. Tech. rep. EURAMET, 2018.

[103] R. Kansao, E. Casanova, A. Blanco, F. Kenyery, and M. Rivero. "Fatigue Life Prediction Due to Slug Flow in Extra Long Submarine Gas Pipelines". In: International Conference on Offshore Mechanics and Arctic Engineering Volume 3: Pipeline and Riser Technology; Ocean Space Utilization (June 2008), pp. 685–692. DOI: 10.1115/OMAE2008-58005. eprint: https://asmedigitalcollection.asme.org/OMAE/proceedings-pdf/OMAE2008/48203/685/4583647/685_1.pdf. URL: https://doi.org/10.1115/OMAE2008-58005.

[104] J. Lewis. "Fast Normalized Cross-Correlation". In: *Ind. Light Magic* 10 (Oct. 2001).

[105] Y. Zhao, L. Lao, and H. Yeung. "Investigation and prediction of slug flow characteristics in highly viscous liquid and gas flows in horizontal pipes". In: *Chemical Engineering Research and Design* 102 (2015), pp. 124–137. ISSN: 0263-8762. DOI: https://doi.org/10.1016/j.cherd.2015.06.002. URL: https://www.sciencedirect.com/science/article/pii/S0263876215002075.

[106] S. Schmelter, S. Knotek, M. Olbrich, A. Fiebach, and M. Bär. "On the influence of inlet perturbations on slug dynamics in horizontal multiphase flow—a computational study". In: *Metrologia* 58.1 (Jan. 2021), p. 014003. DOI: 10.1088/1681-7575/abd1c9. URL: https://doi.org/10.1088/1681-7575/abd1c9.

[107] H. Y. Kuntoro, A. Z. Hudaya, O. Dinaryanto, A. I. Majid, and Deendarlianto. "An improved algorithm of image processing technique for film thickness measurement in a horizontal stratified gas-liquid two-phase flow". In: *AIP Conference Proceedings* 1737.1 (2016), p. 040010. DOI: 10.1063/1.4949298. URL: https://aip.scitation.org/doi/abs/10.1063/1.4949298.

[108] Digpriya, S. Saini, and J. Banerjee. "Analysis of interfacial behavior in two-phase flow using image processing". In: *IOP Conference Series: Materials Science and Engineering* 1146.1 (May 2021), p. 012002. DOI: 10.1088/1757-899x/1146/1/012002. URL: https://doi.org/10.1088/1757-899x/1146/1/012002.

[109] M. Lowe and P. Kutt. "Refraction through cylindrical tubes". In: *Experiments in fluids* 13.5 (1992), pp. 315–320.

[110] M. Born, E. Wolf, A. B. Bhatia, P. C. Clemmow, D. Gabor, A. R. Stokes, A. M. Taylor, P. A. Wayman, and W. L. Wilcock. *Principles of Optics: Electromagnetic Theory of Propagation, Interference and Diffraction of Light*. 7th ed. Cambridge University Press, 1999. DOI: 10.1017/CBO9781139644181.

[111] L. Liu and B. Bai. "Error Analysis of Liquid Holdup Measurement in Gas-Liquid Annular Flow through Circular Pipes using High-Speed Camera Method". In: *Journal of Shanghai Jiaotong University (Science)* 23.1 (2018), pp. 34–40.

[112] W. Steenbergen. "Reduction of beam refraction in optical pipe flow experiments by use of sheet-fabricated pipe walls". In: *Experiments in fluids* 22.2 (1996), pp. 165–173.

[113] U. Kadri, M. Zoeteweij, R. Mudde, and R. Oliemans. "A growth model for dynamic slugs in gas–liquid horizontal pipes". In: *International Journal of Multiphase Flow* 35.5 (2009), pp. 439–449. ISSN: 0301-9322. DOI: https://doi.org/10.1016/j.ijmultiphaseflow.2009.02.003. URL: https://www.sciencedirect.com/science/article/pii/S0301932209000214.

[114] F. Emmert-Streib, Z. Yang, H. Feng, S. Tripathi, and M. Dehmer. "An Introductory Review of Deep Learning for Prediction Models With Big Data". In: *Frontiers in Artificial Intelligence* 3 (2020). ISSN: 2624-8212. DOI: 10.3389/frai.2020.00004. URL: https://www.frontiersin.org/article/10.3389/frai.2020.00004.

[115] A. Graves, A.-r. Mohamed, and G. Hinton. "Speech recognition with deep recurrent neural networks". In: *2013 IEEE International Conference on Acoustics, Speech and Signal Processing*. 2013, pp. 6645–6649. DOI: 10.1109/ICASSP.2013.6638947.

[116] Y. Wang and G. Lin. "Efficient deep learning techniques for multiphase flow simulation in heterogeneous porousc media". In: *Journal of Computational Physics* 401 (2020), p. 108968. ISSN: 0021-9991.

[117] H. Bao, J. Feng, N. Dinh, and H. Zhang. "Computationally efficient CFD prediction of bubbly flow using physics-guided deep learning". In: *International Journal of Multiphase Flow* 131 (2020), p. 103378. ISSN: 0301-9322.

[118] M. Ma, J. Lu, and G. Tryggvason. "Using statistical learning to close two-fluid multiphase flow equations for a simple bubbly system". In: *Physics of Fluids* 27.9 (2015), p. 092101.

[119] Y. Yan, L. Wang, T. Wang, X. Wang, Y. Hu, and Q. Duan. "Application of soft computing techniques to multiphase flow measurement: A review". In: *Flow Measurement and Instrumentation* 60 (2018), pp. 30–43. ISSN: 0955-5986.

[120] A. Alakeely and R. Horne. "Application of deep learning methods to estimate multiphase flow rate in producing wells using surface measurements". In: *Journal of Petroleum Science and Engineering* 205 (2021), p. 108936. ISSN: 0920-4105.

[121] W. Dang, Z. Gao, L. Hou, D. Lv, S. Qiu, and G. Chen. "A Novel Deep Learning Framework for Industrial Multiphase Flow Characterization". In: *IEEE Transactions on Industrial Informatics* 15.11 (2019), pp. 5954–5962.

[122] I. Poletaev, M. P. Tokarev, and K. S. Pervunin. "Bubble patterns recognition using neural networks: Application to the analysis of a two-phase bubbly jet". In: *International Journal of Multiphase Flow* 126 (2020), p. 103194. ISSN: 0301-9322.

[123] T. Haas, C. Schubert, M. Eickhoff, and H. Pfeifer. "BubCNN: Bubble detection using Faster RCNN and shape regression network". In: *Chemical Engineering Science* 216 (2020), p. 115467. ISSN: 0009-2509. DOI: https://doi.org/10.1016/j.ces.2019.115467. URL: https://www.sciencedirect.com/science/article/pii/S0009250919309571.

[124] R. F. Cerqueira and E. E. Paladino. "Development of a deep learning-based image processing technique for bubble pattern recognition and shape reconstruction in dense bubbly flows". In: *Chemical Engineering Science* 230 (2021), p. 116163. ISSN: 0009-2509. DOI: https://doi.org/10.1016/j.ces.2020.116163. URL: https://www.sciencedirect.com/science/article/pii/S0009250920306953.

[125] C. Yu, H. Luo, X. Bi, Y. Fan, and M. He. "An effective convolutional neural network for liquid phase extraction in two-phase flow PIV experiment of an object entering water". In: *Ocean Engineering* 237 (2021), p. 109502. ISSN: 0029-8018. DOI: https://doi.org/10.1016/j.oceaneng.2021.109502. URL: https://www.sciencedirect.com/science/article/pii/S0029801821009021.

[126] H. Ahmad, S. K. Kim, J. H. Park, and S. Y. Jung. "Development of two-phase flow regime map for thermally stimulated flows using deep learning and image segmentation technique". In: *International Journal of Multiphase Flow* 146 (2022), p. 103869. ISSN: 0301-9322. DOI: https://doi.org/10.1016/j.ijmultiphaseflow.2021.103869. URL: https://www.sciencedirect.com/science/article/pii/S0301932221002895.

[127] J. Kottner and T. Dassen. "Interpreting interrater reliability coefficients of the Braden scale: A discussion paper". In: *International Journal of Nursing Studies* 45.8 (2008), pp. 1238–1246. ISSN: 0020-7489.

[128] H. E. Tinsley and D. J. Weiss. “Interrater reliability and agreement of subjective judgments”. In: *Journal of Counseling Psychology* 22.4 (1975), pp. 358–376.

[129] J. J. Berman. “Chapter 4 - Understanding Your Data”. In: *Data Simplification*. Boston: Morgan Kaufmann, 2016, pp. 135–187. ISBN: 978-0-12-803781-2.

[130] S. Xiao, F. Bucher, Y. Wu, A. Rokem, C. S. Lee, K. V. Marra, R. Fallon, S. Diaz-Aguilar, E. Aguilar, M. Friedlander, and A. Y. Lee. “Fully automated, deep learning segmentation of oxygen-induced retinopathy images”. In: *JCI Insight* 2.24 (Dec. 2017).

A

Associated Journal Publications

1. M. Olbrich, E. Schmeyer, L. Riazy, K. Oberleithner, M. Bär and S. Schmelter, "Validation of simulations in multiphase flow metrology by comparison with experimental video observations". In: *Journal of Physics: Conference Series*, 1065 (2018), p. 092015, https://doi.org/10.1088/1742-6596/1065/9/092015.

2. S. Schmelter, M. Olbrich, E. Schmeyer, M. Bär, "Numerical simulation, validation, and analysis of two-phase slug flow in large horizontal pipes". In: *Flow Measurement and Instrumentation*, 73 (2020), p. 101722, ISSN 0955-5986, https://doi.org/10.1016/j.flowmeasinst.2020.101722.

3. S. Schmelter, S. Knotek , M. Olbrich, A. Fiebach, M. Bär, "On the influence of inlet perturbations on slug dynamics in horizontal multiphase flow - a computational study". In: *Metrologia*, 58 (2020), p. 014003, https://doi.org/10.1088/1681-7575/abd1c9.

4. S. Knotek, S. Schmelter, M. Olbrich, "Assessment of different parameters used in mesh independence studies in two-phase slug flow simulations". In: *Measurement: Sensors*, 18 (2021), p. 100317, ISSN 2665-9174, https://doi.org/10.1016/j.measen.2021.100317.

5. S. Schmelter, M. Olbrich, S. Knotek, M. Bär, "Analysis of multiphase flow simulations and comparison with high-speed video observations". In: *Measurement: Sensors*, 18 (2021), p. 100154, ISSN 2665-9174, https://doi.org/10.1016/j.measen.2021.100154.